Reconstruction of a class of fluid flows by variational methods and inversion of integral transforms in tomography.

A Thesis

Submitted to the Tata Institute of Fundamental Research, Mumbai, for the degree of Doctor of Philosophy in Mathematics

by

Souvik Roy

Tata Institute of Fundamental Research-

Centre for applicable mathematics,

Bangalore

March 30, 2015

DECLARATION

This thesis is a presentation of my original research work. Wherever contributions of others are involved, every effort is made to indicate this clearly, with due reference to the literature and acknowledgement of collaborative research and discussions.

The work was done under the guidance of Prof. A. S. Vasudevamurthy and Dr. Praveen Chandrashekar and a collaboration with Dr. Venkateswaran P. Krishnan at the Tata Institute of Fundamental Research, Centre for Applicable Mathematics, Bangalore.

SOUVIK ROY

In my capacity as supervisor of the candidate's thesis, I certify that the above statements are true to the best of my knowledge.

Prof. A. S. Vasudevamurthy **Dr. Praveen Chandrashekar**

Date: March 30, 2015

Abstract

Inverse problems are related to natural fields like atmospheric flows, medical diagnostics, computer vision and many more. The major challenge lies in modelling an inverse problem, inclusion of necessary parameters to recover physical entities using partial data or boundary data and an efficient numerical implementation to determine these entities. The main aim of this thesis is to develop suitable models and efficient numerical implementation of such models for inverse problems in fluid flows and tomography.

Our motivation for studying inverse problems in fluid flows is to understand cloud motion from satellite images using the optical flow method (OFM). For tracking such motion, we applied OFM to images that were generated synthetically by solving the 2D incompressible Stokes, Euler and Navier-Stokes equation. We propose an optical flow algorithm based on variational methods so as to recover fluid motion governed by Stokes and Navier-Stokes equations. We formulate a minimization problem and determine conditions under which solution exists. Numerical results using finite element method not only support theoretical results but also show that Stokes flow forced by a potential are recovered almost exactly.

In the field of inverse problems in tomography, we present an efficient and novel numerical algorithm for inversion of transforms arising in imaging modalities such as ultrasound imaging, thermoacoustic and photoacoustic tomography, intravascular imaging, non-destructive testing, and radar imaging with circular acquisition geometry. Our algorithm is based on recently discovered explicit inversion formulas for circular and elliptical Radon transforms with radially partial data derived by Ambartsoumian, Gouia-Zarrad, Lewis and by Ambartsoumian and Krishnan. These inversion formulas hold when the support of the function lies on the inside (relevant in ultrasound imaging, thermoacoustic and photoacoustic tomography, non-destructive testing), outside (relevant in intravascular imaging), both inside and outside (relevant in radar imaging) of the acquisition circle. Given the importance of such inversion formulas in several new and emerging imaging modalities, an efficient numerical inversion algorithm is of tremendous topical interest. The novelty of our non-iterative numerical inversion approach is that the entire scheme can be pre-processed and used repeatedly in image reconstruction, leading to a very fast algorithm. Several numerical simulations are presented showing the robustness of our algorithm.

Acknowledgments

My first, foremost and sincere thanks to my research guides - Prof. A.S. Vasudeva Murthy and Dr. Praveen Chandrashekhar and my collaborator Dr. Venkateswaran P. Krishnan for their constant support and encouragement. They were a great source of inspiration for me. They were always there for me anytime I needed them. Without their guidance, this thesis would not have been as it is now. My collaboration with them has been highly productive and cherishable.

I would also like to extend my thanks to my institute TIFR-CAM, Bangalore for providing excellent research facilities and environment. I would also thank all the teachers of TIFR-CAM who helped me in every aspect a teacher can.

In context of the thesis, I extend my thanks to Gaik Ambartsoumian whose fruitful suggestions were helpful in improving the tomographic section. Another person to whom I extend my thanks is Dr. Swapan Kumar Chakraborty, who taught me and helped me to build a strong foundation in analysis in my undergraduate course and inspired me to pursue research in PDE.

My next thanks goes to my friends Aradhana Kumari, Deep Ray, Rohit Mishra, Anant Diwakar, Jayesh Badwaik and Pranav Gujar from TIFR-CAM who helped me carry out various experiments connected with the research carried out in this thesis.

Last but not the least, whatever I am now as a human being or a student is because of my family. I express my gratitude to my loving father (who passed away). His constant words of encouragement was a great source of inspiration for me. In spite of his absence, he still remains a strong motivating factor in pursuing my research. Next I express my gratitude to my mother who cared for me always and have always supported me even in times of great trouble. Finally I express my gratitude to my sister and brother-in-law who have remained by my side always.

Contents

List of Figures

List of Tables

Chapter 1

Introduction

Inverse problems have connections to natural fields like atmospheric flows, medical diagnostics, computer vision and many more. Modeling an inverse problem, inclusion of necessary parameters to show an existence of a unique solution, efficient numerical implementation to determine the solution are few of the important questions which arise in the study of inverse problems. The aim of this thesis is precisely to study two major inverse problems. The first one is related to recovery of fluid motion. We use the technique of optical flow estimation to trace passive scalars which are propagated by the flow. Examples of such scalars are smoke, brightness patterns of dense rain-bearing clouds whose intensity remains constant atleast for a short time span. The second one deals with the inversion of circular and elliptic Radon transforms. Such a problem has its importance in detection of tumors, radar imaging and sonar imaging.

1.1 What is Optical Flow

Motions occur from micro to macro scale level. For example motion of atoms in our body occurs at a micro scale level whereas our planet Earth moves around the sun at a macro scale level. Activities like eating, drinking, sleeping, dancing, singing induces motion. Such is human nature that we cannot do without motion. But all of these are so natural that we take them for granted. We need to understand the transformations our world is undergoing else we would not be able to survive. The main difference between us and robots is the concept of perception of changing objects. If robots were to exist in our world, along with us, then they should also have this sense of perception. What is required is a general and flexible representation of visual motion that can be used for many purposes and can be computed efficiently [96].

Optical flow is the distribution of movement of brightness pattern in an image. It can arise from relative motion of objects and viewer. Thus, a good bit of information can be obtained from the optical flow about the spatial arrangement of the objects viewed and the rate of change of this arrangement.

1.1.1 Relationship To Object Motion

The relationship between optical flow in the image plane and velocities of objects in the 3D world is not obvious. For example, when a changing picture is projected onto stationary screen we sense motion. Conversely, a moving object may give rise to constant brightness pattern. For example, a uniform sphere exhibits shading because its surface elements are oriented in many directions. Yet when it is rotated, there is no optical flow at any point of the image, as shading does not move with the surface. (Fig 1.1).

(a) Original Image (b) Image after object was rotated

Figure 1.1: Shading effect: The shading at the bottom of the object looks same even though the object has been rotated. These images were taken at TIFR-CAM, Bangalore

More specifically, consider the diagram in Figure 1.2 which illustrates how the translation and rotation of the camera cause the projected location p in the scene to move.

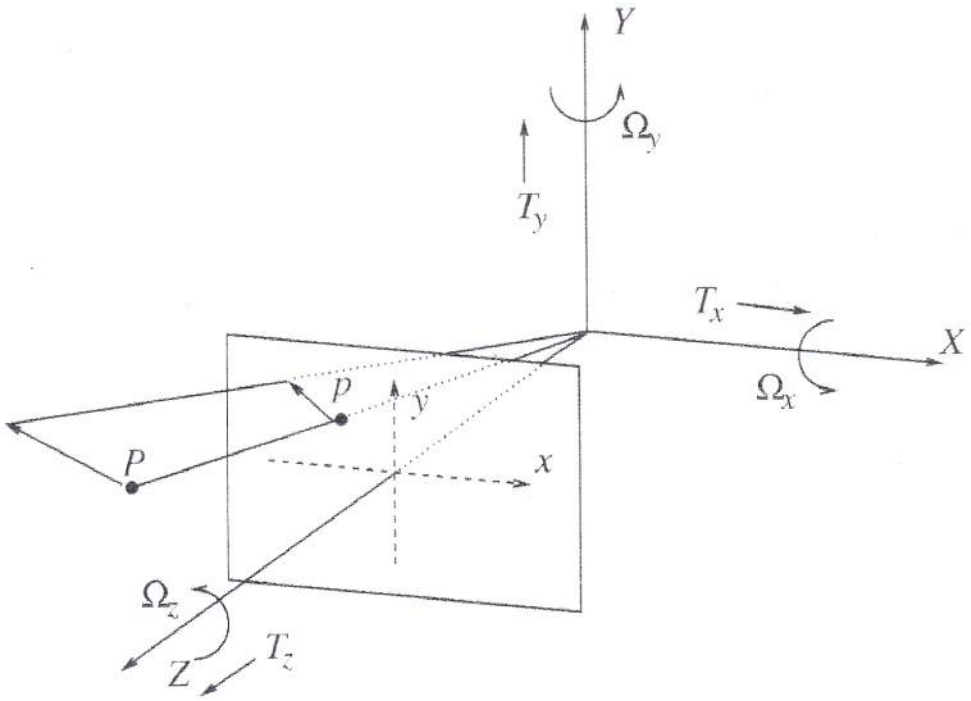

Figure 1.2: A point P in the scene projects to a point in the $[x, y]$ coordinate system of the image plane of a camera centered at the origin of the camera coordinate system $[X, Y, Z]$, with its optical axis pointing in the direction Z. The motion of the camera is described by its translation $[T_X, T_Y, T_Z]$ and rotation $[\Omega_X, \Omega_Y, \Omega_Z]$. Courtesy: ([18]).

Likewise, if point P is moving independently, its projection on the image plane will change, even when the camera is stationary. It is this vector field, $U(x, y) = [u(x, y), v(x, y)]$, describing the horizontal and vertical image motion, that is to be recovered at every point in the image.

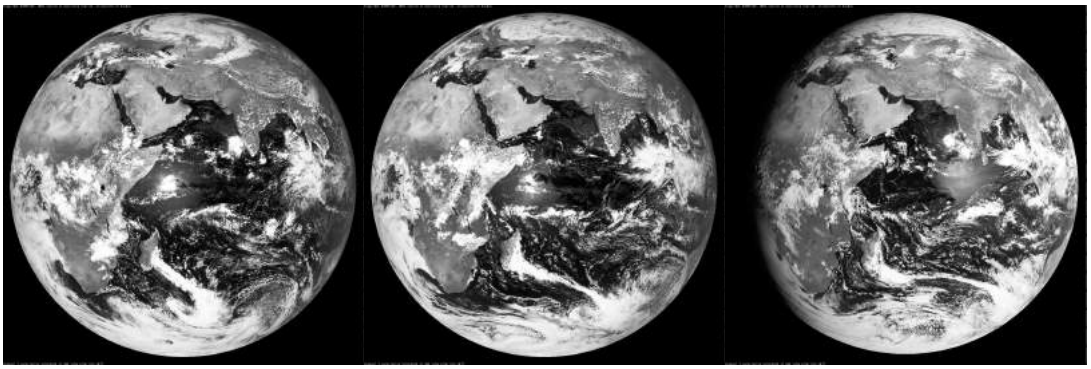

(a) 4^{th} October, 2014 (b) 5^{th} October, 2014 (c) 6^{th} October, 2014

Figure 1.3: Panochromatic Geostationary satellite images of the Indian subcontinent for three consecutive days. Courtesy: Dundee Satellite receiving station.

1.1.2 Problems In Computing The Optical Flow Pattern

Computing optical flow at a point in the image without considering the neighboring points needs additional constraints. This is because the velocity field at each image point has two components while the change in image brightness at a point due to motion yields only one constraint [49]. To illustrate this we consider a brightness pattern where brightness varies as a function of one image coordinate but not the other. Any motion of the pattern in one direction changes the brightness at a particular point, but motion in the other coordinate yields no change. So components of movement in the second direction cannot be computed locally. Thus to determine the flow completely additional constraints must be introduced.

Even if additional constraints are introduced, the notion of determining flow could be difficult. For example let us consider a flag waving against wind. Suppose it were a rigid object, its motion could be described by providing the coordinates of one particle and the orientation of an orthogonal reference frame attached to that particle. However, since it is a non-rigid object, to describe it at any instant of time, trajectory of each individual particle on the flag needs to be specified. Thus to consider "motion" of a non-rigid object, the rigidity properties of the object is important. What we want to capture mathematically is the notion of overall motion when indeed there is one that corresponds to our intuition [93].

1.1.3 Application to Cloud Motion

In this thesis our main aim is to apply optical flow techniques to one of the most important and interesting research area of cloud motion estimation. Geostationary satellites are a valuable source of rainfall information due to the availability of a global view of clouds at an acceptable spatial and temporal resolution. However to retrieve the information from the satellite images is a significant challenge. For example, precipitation peaks while the cloud area is rapidly growing and reduces at the time of maximum cloud area [95], Visible(VIS) and Infrared (IR) channels of the satellites can see only the top-of-the-clouds, not rain at the surface of the earth. Moreover, how a cloud changes with time reflects atmospheric instabilities that occur and most instabilities lead to precipitation. As a consequence, we need some descriptions of cloud motion and pattern changes as an explicit link to rain rate.

Meteosat Second Generation satellites replaced in 2002 the former Meteosat, providing a significantly increased amount of information as compared to the previous version in order to continuously observe the whole Earth [89]. In this sense, MSG generates images every 15 min with a 10-bit quantization, a spatial sampling distance of 3 km at subsatellite point in

11 channels, from the visible to the infrared channel, and 1 km in the high resolution visible channel.

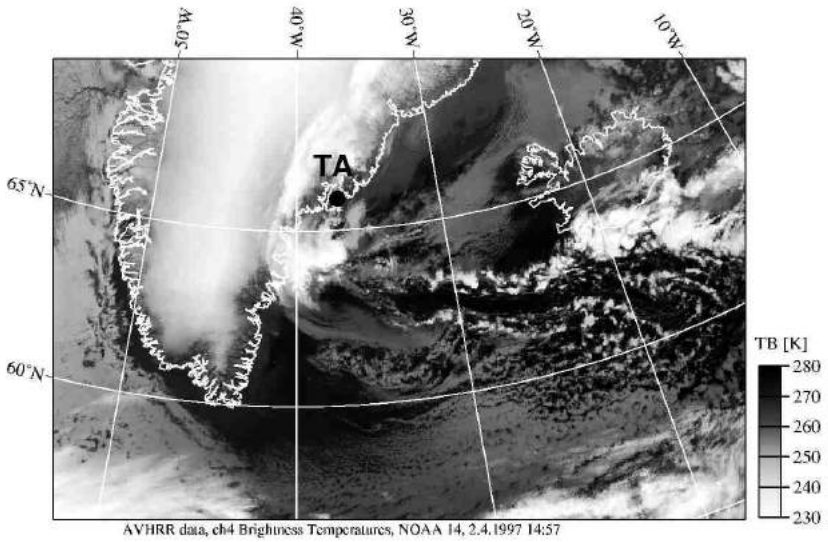

Figure 1.4: In this image, we illustrate, using different greyscale values, the original cloud structure layer classification estimated from the meteorological satellite channels (http://.meteo.uni-bonn.de).

Among the most important applications, numerical weather prediction combines the information from different channels, mainly from the VIS 0.8, WV 6.2, WV 7.3 and IR 10.8 channels, to compute the displacement of the clouds between two time instants, that constitute the most important source of information for this application.

It is well known [49] that tracking rigid body motion by OFM can be done satisfactorily using nonlinear least squares technique whereas it is totally inadequate for fluid flow [45]. This is because rigid body motion have features like geometric invariance where local features such as corners, contours etc are usually stable over time [43]. However for fluid images these features are difficult to define leave alone being stable. This is one of the main problems in understanding the connection between optical flow and fluid flow [74, 29, 67, 63]. Unlike previous approaches where optical flow techniques were used to track rigid body motion, we use such techniques to recover fluid flow velocity which generates motion by tracing scalars introduced into the flow. The difference in the two approaches is shown via an experiment in Appendix D.

1.2 Inverse problem in Tomography

The second kind of inverse problem we deal with in this thesis is in the field of tomography. Circular and elliptical Radon transforms arise naturally. They are extensively used in the study of several modern imaging modalities such as ultrasound reflectivity imaging, thermoacoustic tomography, photoacoustic tomography, intravascular imaging, non-destructive testing, and radar imaging. The representation of a function by its circular Radon transform (CRT)and various related problems arise in many areas of mathematics, physics and imaging science. There has been a substantial spike of interest towards these problems in the last decade mainly due to the connection between the CRT and mathematical models of several emerging medical imaging modalities (See Figure 1.5).

In ultrasound imaging, ultrasonic pulses emitted from a transducer moving along a curve (typically a circle), propagate inside the medium and reflect off inhomogeneities which are measured by the same or a different moving transducer. Assuming that the speed of sound

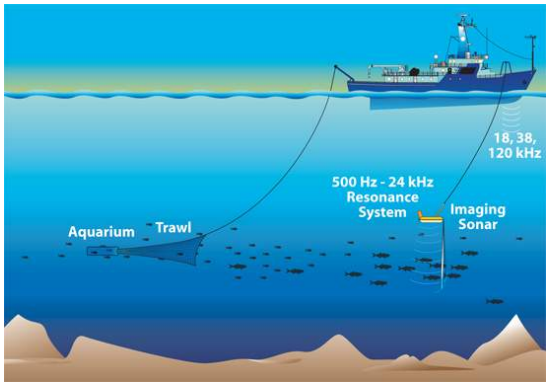

(a) Sonar Imaging. Courtesy: Woods Hole Oceanographic Institution

(b) Breast Mammography. Courtesy: Silenia Dimensions System

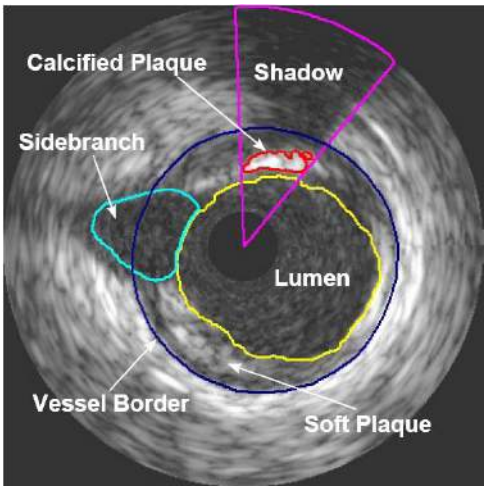

(c) Intravascular Ultrasound. Courtesy: Natural Computing Group, LIACS, Leiden University

(d) Radar Imaging. Courtesy: PSDgraphics

Figure 1.5: Various applications of inversion of Radon transforms

propagation within the medium is constant and that the medium is weakly reflecting, the pulses registered at the receiver transducer is the superposition of all the pulses reflected off those inhomogeneities such that the total distance travelled by the reflected pulse is a constant. This leads to the consideration of an integral transform of a function on a plane (which models the image to be reconstructed), given its integrals along a family of circles (for the case of identical emitter/receiver) or ellipses (for spatially separated emitter/receiver). The goal is to recover an image of the medium given these integrals. In other words, one is interested in the inversion of a circular or elliptical Radon transform. For a detailed discussion of the mathematical model of ultrasound imaging, we refer the reader to [58, 59, 60]. Similarly, the mathematical formulation of problems in thermoacoustic and photoacoustic tomography, non-desctructive testing, intravascular imaging, radar and sonar imaging all lead to inversion of circular or elliptical Radon transforms. For details, we refer the reader to the following references [51, 8, 4].

1.3 Aim of the thesis

In connection to recovery of fluid flows, our aim is to track movement of vortex structures generated by solving the 2D incompressible Stokes, Euler and Navier Stokes equation. Previous work in this direction includes the Horn-Schunck algorithm which implements a constraint free first order regularization approach with a finite differencing scheme [49], estimating optical flow involving prior knowledge that the flow satisfies Stokes equation [88], higher order regularization with incompressibility constraint coupled with mimetic finite differencing scheme [102] and an optimal control approach for determining optical flow without differentiation of data [16].

To recover fluid-type motions, a number of approaches have been proposed to integrate the basic optical flow solution with fluid dynamics constraints, e.g., the continuity equation that describes the fluid property [29, 69] or the divergence-curl (div-curl) equation [29, 12] to describe spreading and rotation. The main aim of our work is to track fluid flow by tracing passive scalars which are propagated by the flow using simple flow dynamics and specifying appropriate boundary conditions. In other words, we use optical flow techniques to efficiently track fluid flow motion. Such a work has its importance in determining atmospheric motion vectors (AMV), tracking smoke propagation, determining motion of tidal waves using floating buoys. Since the basic idea in the variational approach is not to estimate locally and individually but to estimate non-locally by minimizing a suitable functional defined over the entire image section, we therefore prefer a variational approach.

In the field of tomography, our aim is to provide an efficient numerical implementation of inversion formulas for a class of circular and elliptical Radon transforms with radially partial data obtained in the papers [5, 6]. The main contribution of this thesis is a novel implementation of the inversion formulas for a class of circular and elliptical Radon transforms with radially partial data obtained Ambartsoumian, Gouia-Zarrad and Lewis in [5] and Ambartsoumian and Krishnan in [6].

1.4 Overview of the thesis

Chapter 2. The Horn-Schunck optical flow estimation method is reviewed and applied on a simple example to test the method.The image taken as an example is a compact distribution in the unit square in $\mathbb{R}^2$ and moved with a constant velocity. Two cases are considered: in the first case, discrete image derivatives are taken and in the second case, continuous image derivatives are taken. Then the finite difference iterative method is applied to calculate the optical flow velocities and the results are analyzed.

Chapter 3. In this chapter, the mathematical theory of the Horn-Schunck method is devel-

oped, with Dirichlet and Neumann boundary conditions on the optical flow velocities, and existence and uniqueness of the solution to the optical flow problem is proved.

Chapter 4. The finite difference method in Chapter 2 did not give very good results and so another method was tried out using finite elements and the same example was tested and the results were analyzed.

Chapter 5. In this chapter, we deal with recovery of incompressible potential flows. We use a variational approach by minimizing a functional and then apply it to two examples: the first one is an object given by a compact distribution moving in the unit square in $\mathbb{R}^2$ and the second one as flow of a fluid due to a vortex field situated outside the domain i.e the unit square.

Chapter 6. We propose an optical flow algorithm based on variational methods to recover fluid motion governed by Stokes and Navier-Stokes equations. We formulate a minimization problem and determine conditions under which unique solution exists. Numerical results using finite element method not only support theoretical results but also show that Stokes flow forced by a potential are recovered almost exactly.

Chapter 7. We track vortex based motion governed by underlying 2D fluid flow satisfying incompressible Euler and Navier-Stokes equations. A vorticity-streamfunction formulation and optimization techniques are used. We use Helmholtz decomposition of the velocity field and prove existence of a unique velocity and vorticity field for the linearized vorticity equations. Discontinuous Galerkin finite elements are used to solve the vorticity equation for Euler's flow to efficiently track discontinuous vortices. Finally we test our method with two vortex flows governed by Euler and Navier-Stokes equations at high Reynolds number which support our theoretical results.

Chapter 8. Finally, we implement numerical inversion of a class of circular and elliptical Radon transforms with partial radial data derived in "Inversion of the circular Radon transform on an annulus" by Ambartsoumian, Gouia-Zarrad and Lewis, published in Inverse Problems and in a preprint "Inversion of a class of circular and elliptical Radon transforms," by Ambartsoumian and Krishnan. Several numerical computations validating these inversion formulas are presented.

Chapter 2

Horn-Schunck Optical Flow Method

2.1 Introduction

Optical flow method is the estimation of 2D velocities that are in apparent motion as seen in successive image sequences. The estimation is based on the changes in spatio-temporal brightness pattern recorded in such image sequences. Computing optical flow at a given point in the image is an ill-posed problem because change in brightness pattern yields only one constraint whereas there are two components of flow. Hence additional constraints are required to determine the flow uniquely. In this chapter, we discuss the classical method of Horn and Schunck[49]. The method is based on the assumption that the apparent velocity of the brightness pattern varies smoothly almost everywhere in the image. Here gradient-based approaches and finite difference methods are used. While Horn and Schunck optical flow method is used to track rigid body motion, our aim is to use such optical flow techniques for tracking motion due to fluid flow. The image sequences used to track motion are some passive scalars propagated by the flow. The usual Horn and Schunck method in [49] is modified to incorporate non-unit spacing grid and tested on a constant flow. Finally the results are analysed.

2.2 Constraints on the motion of an image

2.2.1 Data conservation

The approach of [49] exploits the assumption of data conservation (See Figure 2.1) i.e. image intensity corresponding to a small image region remains the same, although the location of the region may change. Our given data is a sequence of brightness patterns $E(x, y, t)$ where (x, y)

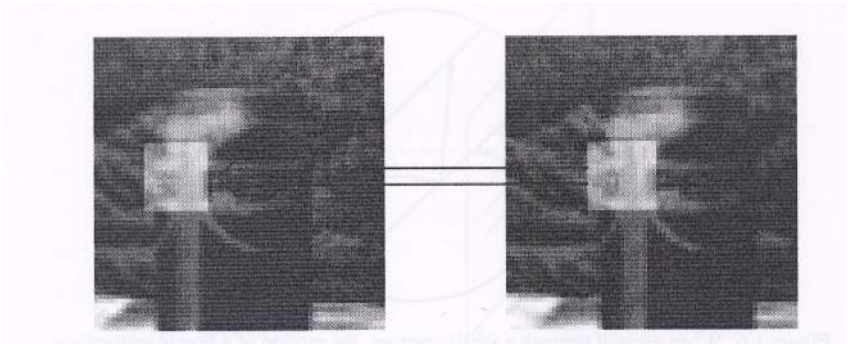

Figure 2.1: Data Conservation assumption. The highlighted region in the right image looks roughly the same as the region in the left image, despite the fact that it has moved. Courtesy: ([18]).

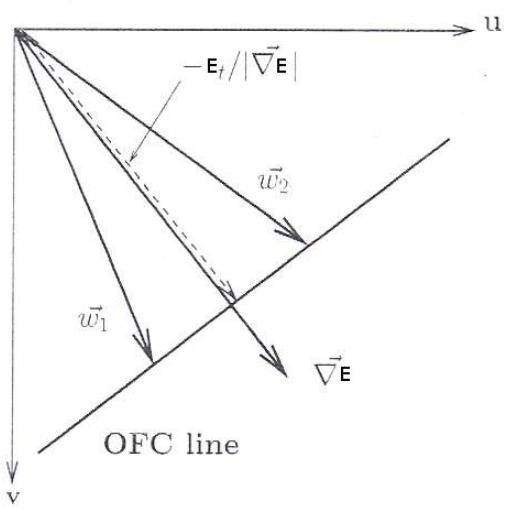

Figure 2.2: The aperture problem: the solutions of (2.1) define a line in the (u, v)-space. The vectors w_1 and w_2 are possible solutions. Courtesy: ([18])

represents the spatial coordinates and t is the time coordinate. As brightness of a particular point in the pattern is constant, we have

$$\frac{dE}{dt} = 0$$

By the chain rule for derivatives (see Appendix A) we have

$$\frac{\partial E}{\partial x}\frac{dx}{dt} + \frac{\partial E}{\partial y}\frac{dy}{dt} + \frac{\partial E}{\partial t} = 0$$

This gives the data conservation constraint

$$E_x u + E_y v + E_t = 0 \tag{2.1}$$

where

$$u = \frac{dx}{dt}, \qquad v = \frac{dy}{dt}.$$

The equation (2.1) can also be written as

$$(E_x, E_y) \cdot (u, v) = -E_t$$

or

$$E_t + U \cdot \nabla E = 0, \qquad U = \begin{pmatrix} u \\ v \end{pmatrix}$$

This means the solution set of (2.1) defines a line in the $u - v$ space which is perpendicular to the intensity spatial gradient ∇E. The component of the optical flow in the direction of the brightness gradient (E_x, E_y) equals

$$\frac{-E_t}{\sqrt{E_x^2 + E_y^2}}$$

The problem is ill-posed as we cannot determine the component of movement in the direction of iso-brightness contours, at right angles to brightness gradient (one equation and two unknowns). This is commonly referred to as the aperture problem. So the flow velocity (u, v) cannot be computed locally without additional constraints

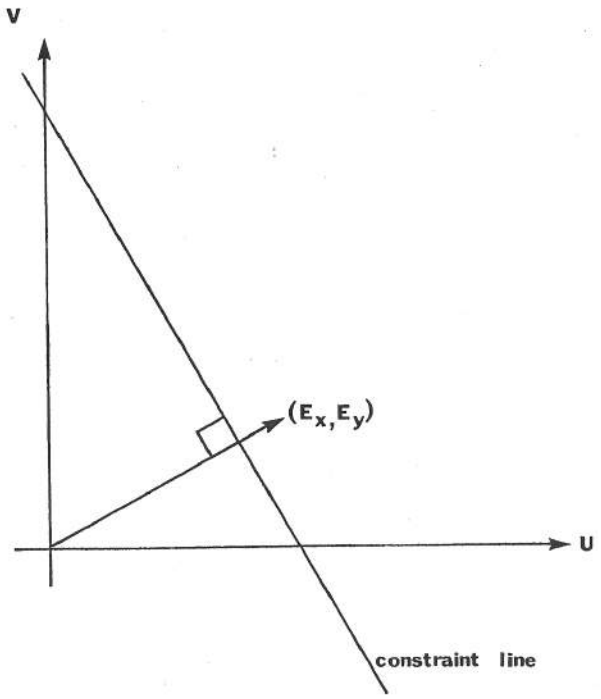

Figure 2.3: The basic rate of change of image brightness equation constrains the optical flow velocity. The velocity (u, v) has to lie along a certain line perpendicular to the brightness gradient vector(E_x, E_y) in the velocity space. Courtesy: ([49]).

2.2.2 Smoothness constraints

The data conservation constraint (2.1) alone is not sufficient to accurately recover optical flow. First, local motion estimates, based on data conservation, may only partially constrain the solution. Consider a motion of a line in Figure 2.3. Within a small region, the data conservation constraint cannot uniquely determine the motion of the line; an infinite number of interpretations are consistent with the constraint. This is commonly referred to as the aperture problem [48]. This can be seen in Figure 2.4 with the interpretations of the movement of the brightness pattern. Hence we cannot predict the motion of the image pattern when viewed through a small aperture. Second and more importantly, motion estimates based on data conservation constraint are very sensitive to noise in the images, particularly in regions where there is very little spatial variation.

To overcome these problems, many approaches have exploited a spatial coherence assumption. Neighboring points in the scene typically belong to the same surface and hence have similar velocities. Since neighboring points in the scene project to neighboring points in the image plane, we expect optical flow to vary smoothly. This assumption is typically implemented as the smoothness constraint. Here we try to limit the difference between the flow velocity at a point and the average velocity over a small neighborhood, containing the point. Equivalently, we can minimize the sum of the squares of the Laplacians of x and y components of the flow. We use this fact while calculating the minimization equations.

2.3 Problem statement

To estimate fluid flow, we trace passive scalars that are propagated by the flow. Examples of such scalars are smoke, brightness patterns of dense rain-bearing clouds whose intensity remains constant atleast for a short time span. These scalars can be represented by a function $E : \Omega \times \mathbb{R}^+ \longrightarrow \mathbb{R}$, where $\Omega \subseteq \mathbb{R}^2$ is a bounded domain of the spatial coordinates and $\mathbb{R}^+$

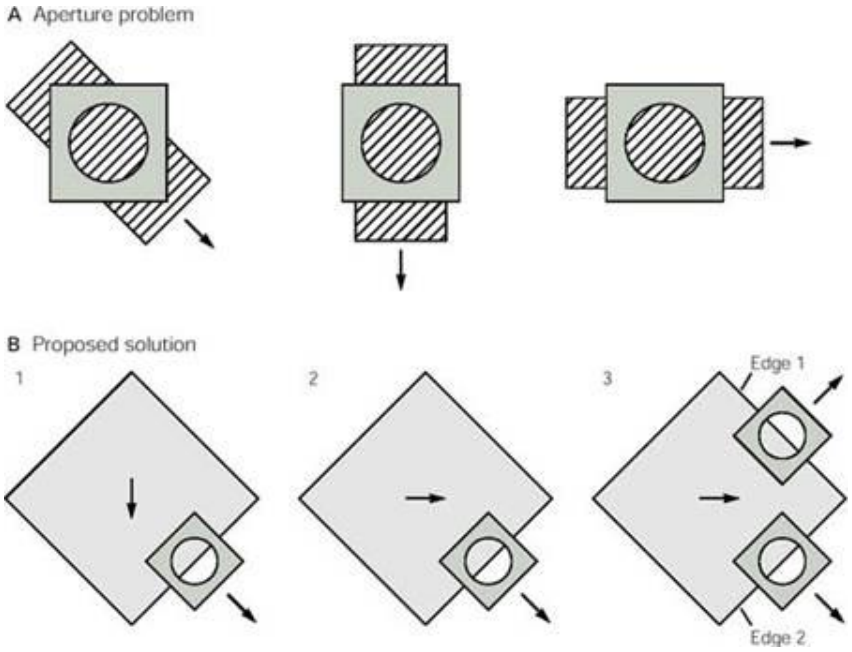

Figure 2.4: Illustration of the aperture problem (www.fisica.cab.cnea.gov.ar).

is the domain of the time coordinate. The field U of optical velocities over Ω, is obtained by minimizing the functional

$$J(U) = \frac{1}{2}\int_{\Omega}(U \cdot \nabla E + E_t)^2 dxdy + \frac{K}{2}\int_{\Omega} \|\nabla U\|^2 \tag{2.2}$$

where $U = (u, v)$. The first term in the functional is the data conservation constraint and the second term in the functional is the smoothness constraint. $K > 0$ is a parameter, called smoothing parameter, which is used to make the order of both the terms same so that each of them has a significant contribution in calculation of the flow velocities. The boundary conditions on the flow velocity could be either Dirichlet or Neumann.

The Euler-Lagrange equations obtained by the minimization of J are

$$\begin{aligned}(E_t + U \cdot \nabla E)E_x - K\Delta u = 0\\ (E_t + U \cdot \nabla E)E_y - K\Delta v = 0\end{aligned} \tag{2.3}$$

(see Theorem (3.2.2)).

2.4 Discretization

Let Ω be discretized by the unit spacing grid and the grid points be indexed by (x_i, y_j) where $1 \leq i, j \leq N$. Let the time axis be discretized by the unit spacing grid and indexed by t_k, $1 \leq k \leq M$.

2.4.1 Estimating the partial derivatives of E

Horn-Schunck proposed the idea of replacing the derivatives of the image E with their finite difference approximations. The following estimates are used. Let $E_x(x_i, y_j, t_k) = E_x^{i,j,k}$, $E_y(x_i, y_j, t_k) = E_y^{i,j,k}$, $E_t(x_i, y_j, t_k) = E_t^{i,j,k}$ Each of the estimates is the average of the first four differences taken

over adjacent measurements in the cube as shown in (Figure 2.5).

$$\begin{aligned}
E_x^{i,j,k} &\approx \frac{1}{4}\{E_{i,j+1,k} - E_{i,j,k} + E_{i+1,j+1,k} - E_{i+1,j,k} + E_{i,j+1,k+1} \\
&\quad - E_{i,j,k+1} + E_{i+1,j+1,k+1} - E_{i+1,j,k+1}\} \\
E_y^{i,j,k} &\approx \frac{1}{4}\{E_{i+1,j,k} - E_{i,j,k} + E_{i+1,j+1,k} - E_{i,j+1,k} + E_{i+1,j,k+1} \\
&\quad - E_{i,j,k+1} + E_{i+1,j+1,k+1} - E_{i,j+1,k+1}\} \\
E_t^{i,j,k} &\approx \frac{1}{4}\{E_{i,j,k+1} - E_{i,j,k} + E_{i+1,j,k+1} - E_{i+1,j,k} + E_{i,j+1,k+1} \\
&\quad - E_{i,j+1,k} + E_{i+1,j+1,k+1} - E_{i+1,j+1,k}\}
\end{aligned} \tag{2.4}$$

where i corresponds to the x-axis direction, j corresponds to the y-axis direction and k corresponds to the time axis and $E_{i,j,k}$ represents the value of the image intensity at the (i, j) position and at the kth stage i.e. $E_{i,j,k} = E(x_i, y_j, t_k)$.

2.4.2 Estimating the Laplacian of flow velocities

Δu and Δv can be approximated using

$$\begin{aligned}
\Delta u(x_i, y_j, t_k) &\approx \kappa(\overline{u}_{i,j,k} - u_{i,j,k}) \\
\Delta v(x_i, y_j, t_k) &\approx \kappa(\overline{v}_{i,j,k} - v_{i,j,k})
\end{aligned}$$

where

$$\begin{aligned}
\overline{u}_{i,j,k} &= \frac{1}{6}\{u_{i-1,j,k} + u_{i,j+1,k} + u_{i+1,j,k} + u_{i,j-1,k}\} \\
&\quad + \frac{1}{12}\{u_{i-1,j-1,k} + u_{i-1,j+1,k} + u_{i+1,j+1,k} + u_{i+1,j-1,k}\}. \\
\overline{v}_{i,j,k} &= \frac{1}{6}\{v_{i-1,j,k} + v_{i,j+1,k} + v_{i+1,j,k} + v_{i,j-1,k}\} \\
&\quad + \frac{1}{12}\{v_{i-1,j-1,k} + v_{i-1,j+1,k} + v_{i+1,j+1,k} + v_{i+1,j-1,k}\}.
\end{aligned} \tag{2.5}$$

The proportionality factor $\kappa = 3$ if the averages are computed as above and if the grid spacing interval is of unit length. (Figure 2.6) illustrates the assignment of weights to neighboring points.

2.5 Minimization equations

With all the approximations as shown in Sec 2.4.1 and Sec 2.4.2, the Euler-Lagrange Equations in (2.3) can be written as

$$\begin{aligned}
(K + E_x^2)u + E_x E_y v &= (K\overline{u} - E_x E_t) \\
E_x E_y u + (K + E_y^2)v &= (K\overline{v} - E_y E_t)
\end{aligned} \tag{2.6}$$

or

$$\begin{aligned}
(K + E_x^2 + E_y^2)(u - \overline{u}) &= -E_x(E_x\overline{u} + E_y\overline{v} + E_t) \\
(K + E_x^2 + E_y^2)(v - \overline{v}) &= -E_y(E_x\overline{u} + E_y\overline{v} + E_t)
\end{aligned} \tag{2.7}$$

The discretized Euler Lagrange equations are as follows

$$\begin{aligned}
(K + (E_x^{i,j,k})^2 + (E_x^{i,j,k})^2)(u_{i,j,k} - \overline{u}_{i,j,k}) &= -E_x^{i,j,k}(E_x^{i,j,k}\overline{u}_{i,j,k} + E_y^{i,j,k}\overline{v}_{i,j,k} + E_t^{i,j,k}) \\
(K + (E_x^{i,j,k})^2 + (E_x^{i,j,k})^2)(v_{i,j,k} - \overline{v}_{i,j,k}) &= -E_x^{i,j,k}(E_x^{i,j,k}\overline{u}_{i,j,k} + E_y^{i,j,k}\overline{v}_{i,j,k} + E_t^{i,j,k})
\end{aligned} \tag{2.8}$$

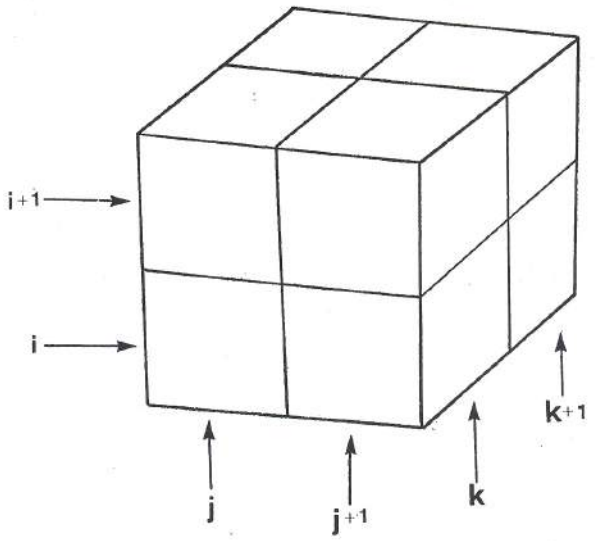

Figure 2.5: The three partial derivatives of image brightness at the center of the cube are each estimated from the average of first differences along four parallel edges of the cube. Here the column index j corresponds to the x-direction in the image, the row index i to the y-direction, while k lies in the time direction: Courtesy ([49]).

1/12	1/6	1/12
1/6	-1	1/6
1/12	1/6	1/12

Figure 2.6: The Laplacian is estimated by subtracting the value at a point(represented in the figure by the central square with weight -1) from a weighted average of the values at neighboring points. Shown here are suitable weights by which values can be multiplied: Courtesy ([49]).

2.6 Discretized iterative scheme

The discretized Euler-Lagrange equations (2.8) lead to the following iterative scheme for solving the optical flow problem

$$\begin{aligned} u_{i,j,k}^{n+1} &= \overline{u}_{i,j,k}^{n} - \frac{E_x^{i,j,k}(E_x^{i,j,k}\overline{u}_{i,j,k}^{n} + E_y^{i,j,k}\overline{v}_{i,j,k}^{n} + E_t^{i,j,k})}{K + (E_x^{i,j,k})^2 + (E_y^{i,j,k})^2} \\ v_{i,j,k}^{n+1} &= \overline{v}_{i,j,k}^{n} - \frac{E_y^{i,j,k}(E_x^{i,j,k}\overline{u}_{i,j,k}^{n} + E_y^{i,j,k}\overline{v}_{i,j,k}^{n} + E_t^{i,j,k})}{K + (E_x^{i,j,k})^2 + (E_y^{i,j,k})^2} \end{aligned} \tag{2.9}$$

where $E_x^{i,j,k}$,$E_y^{i,j,k}$,$E_t^{i,j,k}$ are given by (2.4) and $\overline{u}_{i,j,k}^{n}$,$\overline{v}_{i,j,k}^{n}$ are given by (2.5).

2.7 Courant-Friedrich-Lewey(CFL) condition

The scheme in 2.9 is obtained using an unit spacing grid. We now discretize our grid arbitrarily with $x-$spacing as $\triangle x$, y-spacing as $\triangle y$. To choose $\triangle t$, we now introduce some conditions which will depend on $\triangle x$ and $\triangle y$. This has to be done so that the images we enter in our code should be such that they remain close to each other depending on the grid size. These conditions are called CFL conditions as they were invented by the trio- Courant, Friedrich and Lewey. The natural choice for CFL condition is that the distance covered by the image in time $\triangle t$ will be less than the $\triangle x$ and $\triangle y$ so that two consecutive images remain in the same grid element.
So,

$$|u\triangle t| \leq C\triangle x = h$$
$$|v\triangle t| \leq C\triangle y = h$$

where C is the CFL number. This implies,

$$|\triangle t| \leq Ch \min\left\{\frac{1}{|u|}, \frac{1}{|v|}\right\}$$

Since nothing is known apriori about $\min\left\{\frac{1}{|u|}, \frac{1}{|v|}\right\}$ so we choose C such that

$$\triangle t \leq h. \tag{2.10}$$

2.8 Modified Euler-Lagrange equations

The iterative formula (2.9) holds for $\triangle x = \triangle y = \triangle t = 1$. For our case we choose $\triangle x = \triangle y = h$ and $\triangle t$ is chosen to satisfy (2.10). Hence

$$u(\frac{K}{(\triangle x)^2} + E_x^2) + E_x E_y v = (\frac{K\overline{u}}{(\triangle x)^2} - E_x E_t).$$

$$v(\frac{K}{(\triangle y)^2} + E_y^2) + E_x E_y u = (\frac{K\overline{v}}{(\triangle y)^2} - E_y E_t).$$

We can write the equation in matrix notations as follows

$$\begin{pmatrix} \frac{K}{(\triangle x)^2} + E_x^2 & E_x E_y \\ E_x E_y & \frac{K}{(\triangle y)^2} + E_y^2 \end{pmatrix} \begin{pmatrix} u \\ v \end{pmatrix} = \begin{pmatrix} \frac{K\overline{u}}{(\triangle x)^2} - E_x E_t \\ \\ \frac{K\overline{v}}{(\triangle y)^2} - E_y E_t \end{pmatrix}$$

Let

$$A = \begin{pmatrix} \frac{K}{(\triangle x)^2} + E_x^2 & E_x E_y \\ E_x E_y & \frac{K}{(\triangle y)^2} + E_y^2 \end{pmatrix}$$

Then

$$\text{Det(A)} = \frac{\alpha^4}{(\triangle x \triangle y)^2} + K\left[\frac{E_x^2}{(\triangle y)^2} + \frac{E_y^2}{(\triangle x)^2}\right]$$

and

$$\begin{pmatrix} u \\ v \end{pmatrix} = \frac{1}{\text{Det(A)}} \begin{pmatrix} \frac{K}{(\triangle y)^2} + E_y^2 & -E_x E_y \\ -E_x E_y & \frac{K}{(\triangle x)^2} + E_x^2 \end{pmatrix} \begin{pmatrix} \frac{K\overline{u}}{(\triangle x)^2} - E_x E_t \\ \\ \frac{K\overline{v}}{(\triangle y)^2} - E_y E_t \end{pmatrix}$$

This gives

$$u = \frac{1}{\frac{K}{(\triangle x \triangle y)^2} + \left[\frac{E_x^2}{(\triangle y)^2} + \frac{E_y^2}{(\triangle x)^2}\right]} \left[\frac{\overline{u}}{(\triangle x)^2}\left(\frac{K}{(\triangle y)^2} + E_y^2\right) - \frac{E_x}{(\triangle y)^2}\left(\overline{v}E_y + E_t\right)\right]$$

$$v = \frac{1}{\frac{K}{(\triangle x \triangle y)^2} + \left[\frac{E_x^2}{(\triangle y)^2} + \frac{E_y^2}{(\triangle x)^2}\right]} \left[\frac{\overline{v}}{(\triangle y)^2}\left(\frac{K}{(\triangle y)^2} + E_x^2\right) - \frac{E_y}{(\triangle x)^2}\left(\overline{u}E_x + E_t\right)\right]$$

Now let $\triangle x = \triangle y = h$ and let $\overline{E}_x = E_x \cdot \triangle x$, $\overline{E}_y = E_y \cdot \triangle y$, $\overline{E}_t = E_t \cdot \triangle t$
Then

$$\begin{pmatrix} u \\ v \end{pmatrix} = \frac{1}{\text{Det(A)}} \begin{pmatrix} \alpha^4\overline{u} - K\lambda\overline{E}_x\overline{E}_t + K\overline{u}\overline{E}_y^2 - \overline{E}_x\overline{E}_y K\overline{v} \\ \alpha^4\overline{v} - K\lambda\overline{E}_y\overline{E}_t + K\overline{v}\overline{E}_x^2 - \overline{E}_x\overline{E}_y K\overline{u} \end{pmatrix}$$

where $\text{A} = \begin{pmatrix} K + \overline{E}_x^2 & \overline{E}_x\overline{E}_y \\ \overline{E}_x\overline{E}_y & K + \overline{E}_y^2 \end{pmatrix}$, $\text{Det(A)} = \alpha^4 + K\left(\overline{E}_x^2 + \overline{E}_y^2\right)$ and $\lambda = \frac{h}{\triangle t}$.
Hence we have

$$\begin{aligned} u &= \frac{1}{K + \overline{E}_x^2 + \overline{E}_y^2}\left[(K + \overline{E}_x^2 + \overline{E}_y^2)\overline{u} - \overline{E}_x(\overline{E}_x\overline{u} + \overline{E}_y\overline{v} + \lambda\overline{E}_t)\right] \\ v &= \frac{1}{K + \overline{E}_x^2 + \overline{E}_y^2}\left[(K + \overline{E}_x^2 + \overline{E}_y^2)\overline{v} - \overline{E}_y(\overline{E}_x\overline{u} + \overline{E}_y\overline{v} + \lambda\overline{E}_t)\right] \end{aligned} \tag{2.11}$$

2.9 The modified discretized iterative formula

The modified discretized iterative solution is given as

$$\begin{aligned} u_{i,j,k}^{n+1} &= \overline{u}_{i,j,k}^{n} - \frac{\overline{E}_x^{i,j,k}(\overline{E}_x^{i,j,k}\overline{u}_{i,j,k}^{n} + \overline{E}_y^{i,j,k}\overline{v}_{i,j,k}^{n} + \lambda\overline{E}_t^{i,j,k})}{K + (\overline{E}_x^{i,j,k})^2 + (\overline{E}_y^{i,j,k})^2} \\ v_{i,j,k}^{n+1} &= \overline{v}_{i,j,k}^{n} - \frac{\overline{E}_y^{i,j,k}(\overline{E}_x^{i,j,k}\overline{u}_{i,j,k}^{n} + \overline{E}_y^{i,j,k}\overline{v}_{i,j,k}^{n} + \lambda\overline{E}_t^{i,j,k})}{K + (\overline{E}_x^{i,j,k})^2 + (\overline{E}_y^{i,j,k})^2} \end{aligned} \tag{2.12}$$

where $\overline{E}_x^{i,j,k} = E_x^{i,j,k} \cdot \triangle x$, $\overline{E}_y^{i,j,k} = E_y^{i,j,k} \cdot \triangle y$, $\overline{E}_t^{i,j,k} = E_t^{i,j,k} \cdot \triangle t$ and $E_x^{i,j,k}$,$E_y^{i,j,k}$,$E_t^{i,j,k}$ are given by (2.4), $\overline{u}_{i,j,k}^{n}$,$\overline{v}_{i,j,k}^{n}$ are given by (2.5), $\lambda = \frac{h}{\triangle t}$.

2.10 Convergence of Horn and Schunck Optical Flow estimation method

We have obtained an iterative formula for finding out the solution to the optical flow problem. The next important thing is to show the convergence of the method. It is shown in [61] that the iterative equations (2.9) (commonly referred to as the Jacobi iterations) converge. The iterative equations (2.9) is based on a unit spacing grid. whereas the iterative equations (2.12) is based on a non-unit spacing grid. This introduces an additional λ factor with $\overline{E}_t^{i,j,k}$ in (2.12). Hence modifying the proof in [61] it can be shown that (2.12) also converges.

2.11 Numerical examples

(2.12) is now used to determine motion governed by a constant flow. The scalar E_0 representing the image at time t_0 is given as

$$E_0(x, y) = E(x, y, 0) = e^{-50[(x-1/2)^2+(y-1/2)^2]}.$$

The image sequence E is generated by advecting E_0 with a constant velocity of $(u, v) = (1, 1)$. So at time t, E is given by

$$E(x, y, t) = E_0(x - ut, y - vt) = E(x - ut, y - vt, 0)$$

using the characteristic method. We choose $h = 0.01$ and $\triangle t = 0.01$ satisfying (2.10). The relative L^2 error in velocity is defined as

$$\text{Relative } L^2 \text{ error} = \frac{\|U_e - U_o\|}{\|U_e\|} \tag{2.13}$$

and the advection error is defined as

$$\text{Advection Error} = \|E_t + U_o \cdot \nabla E\| \tag{2.14}$$

where U_e is the exact velocity and U_o is the obtained velocity and the norm $\|\cdot\|$ is the usual L^2 norm for vector functions.

2.11.1 Using finite differences for derivatives of E

First using images at two consecutive times 0 and $\triangle t$ derivatives of E are evaluated at time $t = 0$. Figure 2.11.1 shows the obtained velocity plots for $K = 1$.

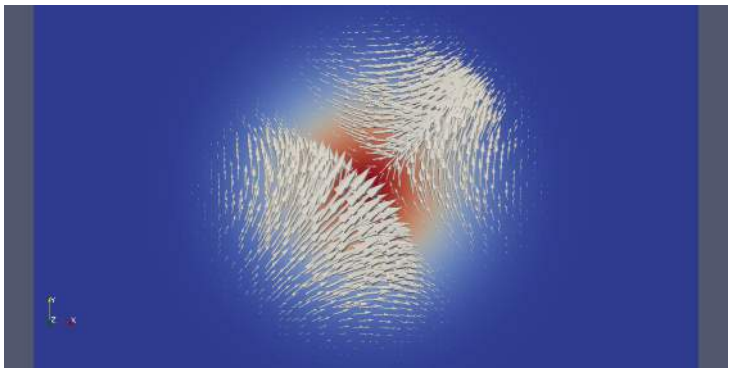

Figure 2.7: Recovered velocity vectors at $t = 0$

Table (2.1) shows the L^2 error in the velocity and the advection error for various valus of K.

K	Relative L^2 error	Advection Error
0.2	1.23	1.67 e-10
1	1.12	1.43 e-10
2	1.37	1.27 e-10

Table 2.1: Variation of relative L^2 error and advection error with the smoothing parameter K

2.11.2 Using analytical derivatives of E

Since $E \in C^\infty$, the derivatives of E can be evaluated exactly. Figure 2.11.1 shows the obtained velocity plots for $K = 1$.

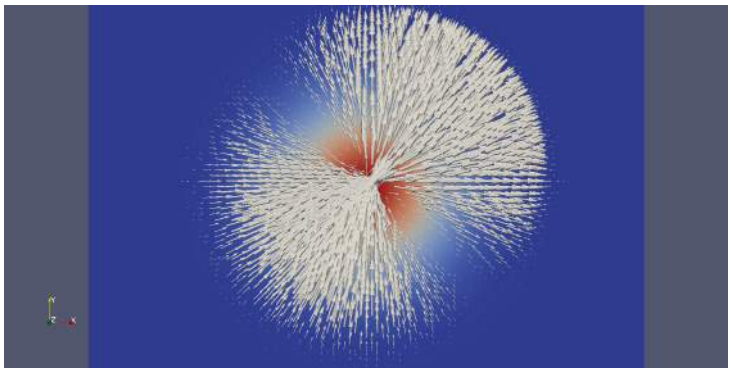

Figure 2.8: Recovered velocity vectors at $t = 0$

Table (2.2) shows the L^2 error in the velocity and the advection error for various valus of K.

K	Relative L^2 error	Advection Error
0.2	0.54	2.21 e-11
1	0.41	2.15 e-11
2	0.49	2.33 e-11

Table 2.2: Variation of relative L^2 error and advection error with the smoothing parameter K

2.12 Conclusions

The results show that the relative L^2 error is of order 1 and it does not improve irrespective of different values of K. The problem could be due to the approximation of the Laplacians of the velocities and derivatives of E by finite differences. In an attempt to improve the order of the relative error we could try the finite element method as it uses the weak form of the PDE and solves it exactly. Also the boundary conditions can be incorporated well into the finite element structure. So with this idea we proceed onto implementing the finite element method to calculate the optical flow velocities. But before doing that we would want to establish the existence and uniqueness of the solution of the optical flow problem and also derive some estimates on the solution.

Chapter 3

Existence, Uniqueness and Stability Results

3.1 Introduction

In the previous chapter, we discussed the Horn and Schunck method and used it to try and recover motion due to fluid flows. A numerical implementation of minimization of optical flow functional (2.2) using finite difference method was performed. In this chapter, we show existence and uniqueness of minimizer for the optical flow functional under some given conditions and also derive some estimates on the solution.

3.2 Existence and uniqueness of minimizer

We set Ω to be the unit square [0,1]$\times$[0,1]. We want to minimize the functional $J(U)$ over the field of optical flow velocities U in Ω where $J(U)$ is given in (2.2). We assume our image $E \in W^{1,\infty}(\Omega)$ and hence $E \in L^2(\Omega)$ as Ω is bounded because

$$\begin{aligned}\int_\Omega E^2 dxdy &\leq \|E\|_{L^\infty}^2 \int_\Omega dxdy \\ &\leq \|E\|_{L^\infty}^2 \\ &< \infty\end{aligned}$$

as $|\Omega| = \int_\Omega dxdy = 1$.

Theorem 3.2.1. *The functional given in (2.2) is convex with respect to U.*

Proof. Let

$$U_1 = \begin{pmatrix} u_1 \\ v_1 \end{pmatrix} \text{ and } U_2 = \begin{pmatrix} u_2 \\ v_2 \end{pmatrix}$$

and let (.) denote the usual inner product in $\mathbb{R}^2$. Then for $0 \leq \alpha \leq 1$ we have,

$$\begin{aligned}
J(\alpha U_1 + (1-\alpha)U_2) =& \frac{1}{2}\int_\Omega ((\alpha U_1 + (1-\alpha)U_2)\cdot \nabla E) + E_t)^2 dxdy \\
&+ \frac{K}{2}\int_\Omega \|\nabla(\alpha u_1 + (1-\alpha)u_2)\|^2 + \|\nabla(\alpha v_1 + (1-\alpha)v_2)\|^2 dxdy \\
\leq& \frac{1}{2}\int_\Omega ((\alpha U_1 + (1-\alpha)U_2)\cdot \nabla E)^2 + (\alpha + 1 - \alpha)E_t^2 + 2E_t((\alpha U_1 + (1-\alpha)U_2)\cdot \nabla E) dxdy \\
&+ \frac{K}{2}\int_\Omega \|\nabla(\alpha u_1 + (1-\alpha)u_2)\|^2 + \|\nabla(\alpha v_1 + (1-\alpha)v_2)\|^2 \, dxdy \\
=& \frac{1}{2}\int_\Omega ((\alpha U_1 + (1-\alpha)U_2)\cdot \nabla E)^2 + (\alpha + 1 - \alpha)E_t^2 + 2E_t((\alpha U_1 + (1-\alpha)U_2)\cdot \nabla E) dxdy \\
&+ \frac{K}{2}\int_\Omega \|(\alpha \nabla u_1 + (1-\alpha)\nabla u_2)\|^2 + \|(\alpha \nabla v_1 + (1-\alpha)\nabla v_2)\|^2 dxdy
\end{aligned} \tag{3.1}$$

Now,

$$\int_\Omega E_t((\alpha U_1 + (1-\alpha)U_2)\cdot \nabla E) dxdy = \alpha \int_\Omega E_t(U_1 \cdot \nabla E) dxdy + (1-\alpha)\int_\Omega E_t(U_2 \cdot \nabla E) dxdy$$

Let $a, b \in \mathbb{R}$ and A, $B \in$ V, an inner product space with inner product $(\cdot)_V$ and let $\|\cdot\|$ be the vector norm for functions defined as

$$\|(f_1, f_2)\|^2 = |f_1|^2 + |f_2|^2.$$

We have,

$$\begin{aligned}
(\alpha a + (1-\alpha)b)^2 &= \alpha^2 a^2 + (1-\alpha)^2 b^2 + \alpha(1-\alpha)2ab \\
&\leq \alpha^2 a^2 + (1-\alpha)^2 b^2 + \alpha(1-\alpha)(a^2 + b^2) \\
&= \alpha a^2 + (1-\alpha)b^2 \qquad \text{where } 0 \leq \alpha \leq 1.
\end{aligned}$$

and

$$\begin{aligned}
\|(\alpha A + (1-\alpha)B)\|^2 &= \alpha^2 \|A\|^2 + (1-\alpha)^2 \|B\|^2 + \alpha(1-\alpha)2(A \cdot B)_V \\
&\leq \alpha^2 \|A\|^2 + (1-\alpha)^2 \|B\|^2 + \alpha(1-\alpha)(\|A\|^2 + \|B\|^2) \\
&= \alpha \|A\|^2 + (1-\alpha)\|B\|^2, \text{ where } 0 \leq \alpha \leq 1.
\end{aligned}$$

Therefore,

$$\begin{aligned}
&\frac{K}{2}\int_\Omega \|(\alpha \nabla u_1 + (1-\alpha)\nabla u_2)\|^2 + \|(\alpha \nabla v_1 + (1-\alpha)\nabla v_2)\|^2 dxdy \\
&\leq \frac{K}{2}\{\alpha \int_\Omega \|\nabla u_1\|^2 + \|\nabla u_2\|^2 dxdy + (1-\alpha)\int_\Omega \|\nabla v_1\|^2 + \|\nabla v_2\|^2 dxdy\}
\end{aligned}$$

Again,

$$\begin{aligned}
\int_\Omega ((\alpha U_1 + (1-\alpha)U_2)\cdot \nabla E)^2 dxdy &= \int_\Omega (\alpha(U_1 \cdot \nabla E) + (1-\alpha)(U_2 \cdot \nabla E))^2 dxdy \\
&\leq \alpha \int_\Omega (U_1 \cdot \nabla E)^2 dxdy + (1-\alpha)\int_\Omega (U_2 \cdot \nabla E)^2 dxdy
\end{aligned}$$

This gives,

$$J(\alpha U_1 + (1-\alpha)U_2) \leq \alpha J(U_1) + (1-\alpha)J(U_2), \qquad 0 \leq \alpha \leq 1 \tag{3.2}$$

So J is a convex functional w.r.t U. □

Theorem 3.2.2. *The unique minimizer of J will be given by the unique solution of $J'(U) = 0$, where $'$ denotes the Gateaux Derivative.*

Proof. See Appendix B □

We now determine the unique solution of $J'(U) = 0$. Now,

$$J(U + \epsilon\overline{U}) = \frac{1}{2}\int_\Omega ((U + \epsilon\overline{U}) \cdot \nabla E) + E_t)^2 dxdy + \frac{K}{2}\int_\Omega \|\nabla(u + \epsilon\overline{u})\|^2 + \|\nabla(v + \epsilon\overline{v})\|^2 \; dxdy$$

where $\overline{U} = \begin{pmatrix} \overline{u} \\ \overline{v} \end{pmatrix} \in Z = (H^1(\Omega))^2$ and $\epsilon > 0$.
This gives

$$J(U + \epsilon\overline{U}) = \frac{1}{2}\int_\Omega E_t^2 + 2E_t((U + \epsilon\overline{U}) \cdot \nabla E) + (U \cdot \nabla E)^2 + \epsilon^2(\overline{U} \cdot \nabla E)^2 + 2\epsilon(U \cdot \nabla E)(\overline{U} \cdot \nabla E)$$
$$+\frac{K}{2}\int_\Omega \|\nabla u\|^2 + \epsilon^2\|\nabla\overline{u}\|^2 + 2\epsilon(\nabla u \cdot \nabla\overline{u}) + \|\nabla v\|^2 + \epsilon^2\|\nabla\overline{v}\|^2 + 2\epsilon(\nabla v \cdot \nabla\overline{v})$$

which implies

$$J(U + \epsilon\overline{U}) - J(U) = \frac{1}{2}\int_\Omega 2\epsilon E_t(\overline{U} \cdot \nabla E) + \epsilon^2(\overline{U} \cdot \nabla E)^2 + 2\epsilon(U \cdot \nabla E)(\overline{U} \cdot \nabla E)$$
$$+\frac{K}{2}\int_\Omega 2\epsilon(\nabla u \cdot \nabla\overline{u}) + 2\epsilon(\nabla v \cdot \nabla\overline{v}) + \epsilon^2\|\nabla\overline{u}\|^2 + \epsilon^2\|\nabla\overline{v}\|^2$$

So we have

$$\lim_{\epsilon\to 0}\frac{J(U + \epsilon\overline{U}) - J(U)}{\epsilon} = \int_\Omega (E_t + (U \cdot \nabla E))(\overline{U} \cdot \nabla E) + K\int_\Omega (\nabla u \cdot \nabla\overline{u}) + (\nabla v \cdot \nabla\overline{v}) \tag{3.3}$$

Now applying integration by parts we get,

$$\int_\Omega (\nabla u \cdot \nabla\overline{u}) = -\int_\Omega (\overline{u}\Delta u) + \int_{\partial\Omega}(\frac{\partial u}{\partial\nu} \cdot \overline{u}),$$
$$\int_\Omega (\nabla v \cdot \nabla\overline{v}) = -\int_\Omega (\overline{v}\Delta v) + \int_{\partial\Omega}(\frac{\partial v}{\partial\nu} \cdot \overline{v})$$

If we assume zero Dirichlet or Neumann boundary conditions on the flow velocity U we have,

$$\int_{\partial\Omega}(\frac{\partial u}{\partial\nu} \cdot \overline{u}) = 0 = \int_{\partial\Omega}(\frac{\partial v}{\partial\nu} \cdot \overline{v})$$

This gives,

$$\lim_{\epsilon\to 0}\frac{J(U + \epsilon\overline{U}) - J(U)}{\epsilon} = \int_\Omega (E_t + (U \cdot \nabla E))(\overline{U} \cdot \nabla E) - K\int_\Omega (\Delta U \cdot \overline{U})$$

Since $\overline{U}$ is arbitrary, so $J'(U)(\overline{U}) = 0$ gives the optimality conditions

$$\left.\begin{aligned}(E_t + U \cdot \nabla E)E_x - K\Delta u = 0 \\ (E_t + U \cdot \nabla E)E_y - K\Delta v = 0\end{aligned}\right\} \tag{3.4}$$

which are the required Euler-Lagrange equations for finding the minimum of the functional J. Equations (3.4) can be written as

$$-\Delta u + \frac{E_x^2}{K}u + \frac{E_xE_y}{K}v = -\frac{E_xE_t}{K}$$
$$-\Delta v + \frac{E_xE_y}{K}u + \frac{E_y^2}{K}v = -\frac{E_yE_t}{K}$$

In matrix notation we have,

$$LU + BU = F, \tag{3.5}$$

where $U = \begin{pmatrix} u \\ v \end{pmatrix}$, $L = \begin{pmatrix} -\Delta & 0 \\ 0 & -\Delta \end{pmatrix}$, $B = \frac{1}{K}\begin{pmatrix} E_x^2 & E_xE_y \\ E_xE_y & E_y^2 \end{pmatrix}$, $F = \frac{1}{K}\begin{pmatrix} -E_xE_t \\ -E_yE_t \end{pmatrix}$.

3.3 Existence and uniqueness of solution of J′(U) = 0

We take $H = (L^2(\Omega))^2$ with the corresponding norm $\|.\|_H$ and $Z = (H^1(\Omega))^2$ with the corresponding norm $\|.\|_Z$ and $\|.\|_{L^2}$ represents the usual norm $L^2(\Omega)$.

3.3.1 Zero Dirichlet boundary condition for velocity

In this case $U \in (H_0^1(\Omega))^2$.

Theorem 3.3.1. *There exists a unique solution for $J'(U) = 0$ in H where J is the functional as in (2.2) and it is assumed that the velocity of the optical flow satisfies zero Dirichlet boundary condition.*

Proof. By (3.5) we have

$$LU + BU = F$$

Since L^{-1} exists by Theorem 3.2.2, this gives us

$$\begin{aligned} U &= -L^{-1}BU + L^{-1}F \\ &= G(U) \end{aligned}$$

We form the following iteration

$$U_{n+1} = G(U_n) \tag{3.6}$$

If we can show that $G : H \to H$ is a contraction mapping, then there exists a fixed point U_0 of (3.6) which is also unique. Now

$$\|G(U_1) - G(U_2)\|_H = \|L^{-1}B(U_1 - U_2)\|_H$$

$$= \left\| \begin{pmatrix} (-\Delta)^{-1}E_x^2(u_1 - u_2) \\ (-\Delta)^{-1}E_x^2(u_1 - u_2) \end{pmatrix} \right\|_H$$

As we have assumed $U \in (H_0^1(\Omega))^2$, it implies

$$\|(-\Delta)^{-1}F\|_H \leq C_1\|F\|_H$$

where C_1 is a constant depending on F and Ω. Therefore,

$$\|G(U_1) - G(U_2)\|_H \leq \frac{C_1}{K}\left\{\left\|E_x^2(u_1-u_2)\right\|_{L^2} + \left\|E_y^2(v_1-v_2)\right\|_{L^2}\right\}$$

$$\leq \frac{C_1}{K}\left\{\|E_x\|_{L^\infty}^2 \|(u_1-u_2)\|_{L^2} + \|E_y\|_{L^\infty}^2 \|(v_1-v_2)\|_{L^2}\right\}$$

$$\leq \frac{C}{K}\left\{\|(u_1-u_2)\|_{L^2} + \|(v_1-v_2)\|_{L^2}\right\}, \text{where } C = max\left\{\|E_x\|_{L^\infty}^2, \|E_y\|_{L^\infty}^2, C_1\right\}$$

$$< \|U\|_H, \qquad \text{if } K > C$$

which is true as K is a parameter chosen by us. So $G : H \to H$ is a contraction mapping. Hence, $J'(U) = 0$ has a unique solution in H. □

We will show later in Section 3.4 that the unique solution obtained above belongs to Z.

3.3.2 Zero Neumann boundary condition for velocity

Next let us assume Neumann boundary condition for the optical flow velocity. In general, it is not possible to show existence and uniqueness of solution for (3.5). But under certain hypothesis it can be shown that problem (3.5) has a unique solution.

We write $J'(U)[V] = 0 \quad \forall V \in Z$ as $A(U,V) = F(V)$ where $A(U,V)$ is a symmetric bi-linear form on $Z \times Z$ associated to the functional (6.1) and $F(V)$ is a linear form on Z defined as

$$A(U,V) = \int_\Omega (U\cdot\nabla E)(V\cdot\nabla E) + K\int_\Omega \nabla u_1\cdot\nabla v_1 + \nabla u_2\cdot\nabla v_2 \tag{3.7}$$

and

$$F(V) = -\int_\Omega E_t\cdot(\nabla E\cdot V) \tag{3.8}$$

where $U = \begin{pmatrix} u_1 \\ u_2 \end{pmatrix}, \quad V = \begin{pmatrix} v_1 \\ v_2 \end{pmatrix}$.

Theorem 3.3.2. *The bi-linear form $A(U,V)$ as given in (3.7) is continuous $\forall\, U, V \in Z$.*

Proof.

$$\begin{aligned}|A(U,V)| &= \left|\int_\Omega (U\cdot\nabla E)(V\cdot\nabla E) + K\int_\Omega (\nabla u_1\cdot\nabla v_1 + \nabla u_2\cdot\nabla v_2)\right| \\ &\leq \|U\cdot\nabla E\|_{L^2}\|V\cdot\nabla E\|_{L^2} + K(\|\nabla u_1\|_H\|\nabla v_1\|_H + \|\nabla u_1\|_H\|\nabla u_1\|_H)\end{aligned}$$

By the inequality,

$$(a+b)^2 \leq (a+b)^2 + (a-b)^2 = 2(a^2+b^2)$$

we have

$$\begin{aligned}\|U\cdot\nabla E\|_{L^2} &\leq \left[2\|E_x\|_{L^\infty}^2\int_\Omega u_1^2 + 2\|E_y\|_{L^\infty}^2\int_\Omega u_2^2\right]^{\frac{1}{2}} \\ &\leq \left[2\max\left\{\|E_x\|_{L^\infty}^2, \|E_y\|_{L^\infty}^2\right\}\right]^{\frac{1}{2}}\|U\|_H.\end{aligned}$$

Hence we obtain

$$|A(U,V)| \leq C_1(\|U\|_H\|V\|_H + \|\nabla u_1\|_H\|\nabla v_1\|_H + \|\nabla u_2\|_H\|\nabla v_2\|_H)$$

$$\leq C_1[\|U\|_H^2 + \|\nabla u_1\|_H^2 + \|\nabla u_2\|_H^2]^{\frac{1}{2}}.[\|V\|_H^2 + \|\nabla v_1\|_H^2 + \|\nabla v_2\|_H^2]^{\frac{1}{2}}$$

$$= C_1\|U\|_Z.\|V\|_Z$$

where $C_1 = 2\max\left\{2\|E_x\|_{L^\infty}^2, 2\|E_y\|_{L^\infty}^2, \frac{K}{2}\right\}$. Hence $A(U,V)$ is continuous $\forall\ U, V \in Z$ □

Theorem 3.3.3. *The linear form $F(V)$ as in (3.8) is continuous $\forall\ V \in Z$.*

Proof.

$$\begin{aligned}|F(V)| &= |\int_\Omega E_t(V\cdot\nabla E| \\ &\leq \|E_t\nabla E\|_H\|V\|_H \\ &\leq \|E_t\nabla E\|_H\|V\|_Z \\ &\leq \|E_t\|_H\|\nabla E\|_H\|V\|_Z \\ &= C_2\|V\|_Z\end{aligned}$$

where $C_2 = |E_t\|_H \cdot \|\nabla E\|_H$. Hence $F(V)$ is continuous $\forall\ V \in Z$ □

Before trying to determine whether a unique solution of $J'(U) = 0$ exists or not, we first state the Lax-Milgram theorem which will be used in the forthcoming stages.

Theorem 3.3.4 (**Lax-Milgram**). *Let V be a Hilbert space , $a(.,.) : V \times V \to \mathbb{R}$ a continuous and coercive bi-linear form, $F(\cdot) : V \to \mathbb{R}$ a linear and continuous functional. Then there exists a unique solution to the problem: find $u \in V$ such that*

$$a(u,v) = F(v) \quad \forall v \in V$$

.

Theorem 3.3.5. *If $A(.,.)$ as in (3.7) is coercive on Z, then $A(U,V) = F(V)$ has a unique solution $\forall\ \ V \in Z$ and hence $J'(U)[V] = 0 \quad \forall V \in Z$ has a unique solution U_0 which is the unique minimizer of the functional $J(U)$ as in (2.2).*

Proof. Using Lax-Milgram's Theorem in Z we get the first part of the theorem. The second part follows from the fact that $A(U,V) = F(V)$ is equivalent to the fact that $J'(U)[V] = 0 \quad \forall V \in Z$. □

Now we will show that the bi-linear form $A(U,V)$ is $Z-$coercive under some given conditions.
Case 1:

First we assume that on a part Ω_1 of the boundary Ω, U vanishes, where $\mu(\Omega_1) > 0$.

Theorem 3.3.6. *Under the above hypothesis, the bi-linear form $A(U,V)$ as in (3.7) is $Z-$coercive.*

Proof. We have,

$$\begin{aligned}A(U,U) &= \int_\Omega (U\cdot\nabla E)^2 + K\int_\Omega (\nabla u_1)^2 + (\nabla u_2)^2 \\ &\geq K\int_\Omega (\nabla u_1)^2 + (\nabla u_2)^2 \\ &\geq K\|U\|_Z. \text{ (By Poincare's Inequality, see [50])}\end{aligned}$$

The bi-linear form $A(U,V)$ is coercive and hence $A(U,V) = F(V)$ has a unique solution for all $V \in Z$. This implies that $J'(U)$=0 has a unique solution U_0 which is the unique minimizer of the functional $J(U)$ as in (2.2). □

Case 2:

In this case we do not assume any condition on the flow velocity across the boundary of Ω. But we assume E_x and E_y are linearly independent and they are in $H^1(\Omega)$. We then show the bi-linear form is coercive.

Theorem 3.3.7. *Under the above hypothesis, the bi-linear form $A(U,V)$ as in (3.7) is $Z-$coercive.*

Proof. The following derivations are based on the work of Horn and Schunck, Nagel and can be found in [90]. We use the Poincare-Wirtinger's Inequality[50]

$$\int_\Omega (U-T)^2 dxdy \leq D \int_\Omega |\nabla U|^2 dxdy \tag{3.9}$$

where

$$T = \frac{1}{|\Omega|}\int_\Omega U dxdy, |\Omega| = \int_\Omega dxdy = 1 \tag{3.10}$$

and D is a constant depending on Ω. Suppose $A(.,.)$ is not coercive. Then there does not exist any constant $M > 0$ such that

$$A(U,U) \geq M\|U\|_Z^2.$$

So for any $M > 0$ there exists $U_M \in Z$ such that

$$A(U_M, U_M) < M\|U_M\|_Z^2.$$

We choose $M = \frac{1}{n}$ and get a sequence of M_n's and correspondingly we will get U_n. Without loss of generality we choose $\|U_n\|_Z = 1$. If not, we can take $V_n = \frac{U_n}{\|U_n\|_Z}$ and replace U_n with V_n. So we get a sequence $\{U_n\}_{n\in\mathbb{N}}$ in Z with $\|U_n\|_Z = 1$ and $A(U_n, U_n) \to 0$ as $n \to \infty$.
From (6.11) using the bi-linear form A we have

$$\int_\Omega (u_n - T_n^1)^2 dxdy \to 0 \tag{3.11}$$

and

$$\int_\Omega (v_n - T_n^2)^2 dxdy \to 0 \qquad \text{for } n \to \infty. \tag{3.12}$$

where

$$T_n^1 = \frac{1}{|\Omega|}\int_\Omega u_n dxdy, T_n^2 = \frac{1}{|\Omega|}\int_\Omega v_n dxdy$$

As,

$$\int_\Omega (E_x u + E_y v)^2 dxdy \leq 2|E_x^2|_\infty \int_\Omega u^2 dxdy + 2|E_y^2|_\infty \int_\Omega v^2 dxdy$$

we have

$$\int_\Omega \left[E_x(u_n - T_n^1) + E_y(v_n - T_n^2)\right]^2 dxdy \to 0 \qquad \text{for } n \to \infty. \tag{3.13}$$

Now

$$\begin{aligned}\left[\int_\Omega (E_xT_n^1 + E_yT_n^2)^2 dxdy\right]^{1/2} &= \left[\int_\Omega (E_xu_n + E_yv_n + E_x(T_n^1 - u_n) + E_y(T_n^2 - v_n))^2 dxdy\right]^{1/2} \\ &\leq \left[\int_\Omega (E_xu_n + E_yv_n)^2 dxdy\right]^{1/2} + \left[\int_\Omega (E_x(T_n^1 - u_n) + E_y(T_n^2 - v_n))^2 dxdy\right]^{1/2} \\ &\leq [A(U_n, U_n)]^{\frac{1}{2}} + \left[\int_\Omega (E_x(T_n^1 - u_n) + E_y(T_n^2 - v_n))^2 dxdy\right]^{1/2} \\ &\to 0 \text{ for } n \to \infty \qquad \text{(Using 3.13)}\end{aligned} \tag{3.14}$$

We have

$$\begin{aligned}\|p+q\|_H^2 &= \|p\|_H^2 + \|q\|_H^2 + 2(p,q) \\ &\geq \|p\|_H^2 + \|q\|_H^2 - 2\|p\|_H\|q\|_H \frac{|(p,q)|}{\|p\|_H\|q\|_H} \\ &\geq \|p\|_H^2 + \|q\|_H^2 - (\|p\|_H^2 + \|q\|_H^2)\frac{|(p,q)|}{\|p\|_H\|q\|_H} \\ &= (\|p\|_H^2 + \|q\|_H^2)\{1 - \frac{|(p,q)|}{\|p\|_H\|q\|_H}\}\end{aligned}$$

We take $p = E_xT_n^1, q = E_yT_n^2$. So we get

$$\int_\Omega (E_xT1_n + E_yT2_n)^2 dxdy \geq \left[\|E_x\|_H^2 (T1_n)^2 + \|E_y\|_H^2 (T2_n)^2\right] \{1 - \frac{|(E_x, E_y)|}{\|E_x\|_H\|E_y\|_H}\} \tag{3.15}$$

As left hand side of (3.15) goes to zero as $n \to \infty$ and by linear independency of E_x and E_y

$$1 - \frac{|(E_x, E_y)|}{\|E_x\|_H\|E_y\|_H} > 0$$

and $\|E_x\|_H$ and $\|E_y\|_H$ are not identically 0, we have

$$T_n^1 \to 0 \text{ and } T_n^2 \to 0 \text{ as } n \to \infty \tag{3.16}$$

But this gives a contradiction as,

$$\begin{aligned}\|U_n\|_Z &= 1 \\ &= \|(U_n - T_n) + U_n\|_Z \\ &\leq \|(U_n - T_n)\|_Z + \|T_n\|_Z \to 0 \text{ as } n \to \infty (\text{by } (3.11), (3.12), (3.16)).\end{aligned}$$

So $A(.,.)$ is coercive. Hence $J'(U) = 0$ has a unique solution $U = U_0$ in Z □

In the Dirichlet case, a unique minimizer of the functional $J(U)$ exists in $H(\Omega)$ and in the Neumann case, a unique minimizer of the functional $J(U)$ exists in Z, provided E_x and E_y are linearly independent or in some part of $\partial\Omega$ there is no velocity flux. But we will now show that if the minimizer of the functional J, as in (2.2), belongs to H, then it is also in Z. So in both the cases we have a unique minimizer in Z.

3.4 Estimates for the minimizer

We now derive some estimates for the unique minimizer obtained in the above cases.

3.4.1 Dirichlet case

Theorem 3.4.1. *The unique minimizer of $J(U)$, $U = U_0$ obtained in Theorem 3.3.1 for the Dirichlet case exists in Z.*

Proof. We have seen that U_0 satisfies (3.5). Then we have,

$$(LU_0, U_0) + (BU_0, U_0) = (F, U_0) \text{ (Taking inner product of (3.5) with } U_0)$$

This gives

$$\|\nabla U_0\|_H^2 + (BU_0, U_0) = (F, U_0)$$

since

$$(LU_0, U_0) = -(\Delta U_0, U_0)$$

Using integration by parts and Dirichlet boundary conditions we get,

$$\begin{aligned}(LU_0, U_0) &= (\nabla U_0, \nabla U_0) \\ &= \|\nabla U_0\|_H^2\end{aligned}$$

Adding $\|U_0\|_H^2$ on both sides we get,

$$\|U_0\|_H^2 + \|\nabla U_0\|_H^2 + (BU_0, U_0) = (F, U_0) + \|U_0\|_H^2 \tag{3.17}$$

Now

$$\sup_{\|U_0\|_H \neq 0} \frac{|(BU_0, U_0)|}{\|U_0\|_H^2} = \|B\|$$

This implies

$$-(BU_0, U_0) \leq \|B\|\|U_0\|_H^2 \tag{3.18}$$

Therefore equation (3.17) gives

$$\begin{aligned}&\|U_0\|_Z^2 = (F, U_0) - (BU_0, U_0) + \|U_0\|_H^2 \\ &\leq \|F\|_H\|U_0\|_H + (1 + \|B\|)\|U_0\|_H^2 \text{ (Using (3.18))} \\ &< \infty \text{ since } U_0 \in H^1(\Omega).\end{aligned} \tag{3.19}$$

Hence $U_0 \in Z$. □

We see that for the Dirichlet case also, the unique minimizer $U_0 \in Z$. Now we will prove an estimate for U_0 in terms of the image derivatives E_x and E_y.

Theorem 3.4.2. *U_0 obtained in Theorem 3.3.1 satisfies*

$$\|U_0\|_Z \leq C\|E_t \nabla E\|_H$$

where constant C depends on Ω and the smoothing parameter K.

Proof. By (3.17) we have $(LU_0, U_0) + (BU_0, U_0) = (F, U_0)$ where $F = -\frac{1}{K}(E_x E_t, E_y E_t)^t$. But $(LU_0, U_0) = \|\nabla U_0\|_H^2$ and

$$\begin{aligned}(BU_0, U_0) &= \left(\begin{pmatrix} \frac{E_x^2}{K} & \frac{E_x E_y}{K} \\ \frac{E_x E_y}{K} & \frac{E_y^2}{K} \end{pmatrix} \begin{pmatrix} u_0 \\ v_0 \end{pmatrix}, \begin{pmatrix} u_0 \\ v_0 \end{pmatrix}\right) \\ &= \frac{1}{K} \begin{pmatrix} E_x^2 u_0 + E_x E_y v_0 \\ E_x E_y u_0 + E_y^2 v_0 \end{pmatrix} \begin{pmatrix} u_0 \\ v_0 \end{pmatrix} \\ &= \frac{1}{K}(u_0 E_x + v_0 E_y)^2 \geq 0.\end{aligned}$$

Hence $\|\nabla U_0\|_H^2 \leq (LU_0, U_0) \leq (F, U_0)$. But $\|\nabla U_0\|_H^2 \geq C(\Omega)\|U_0\|_Z^2$ (By Poincare's inequality where $C(\Omega) > 0$ is a constant depending on Ω).

$$\begin{aligned}
\|U_0\|_Z^2 &\leq \frac{1}{C(\Omega)}(F, U_0) \\
&\leq \frac{1}{C(\Omega)}\|F\|_H\|U_0\|_H \qquad \text{(By Hölder's Inequality)} \\
&\leq \frac{1}{C(\Omega)}\|F\|_H\|U_0\|_Z \\
&= \frac{1}{KC(\Omega)}\|E_t\nabla E\|_H\|U_0\|_Z
\end{aligned}$$

Suppose $U_0 \neq 0$ identically. Then we have the following estimate

$$\|U_0\|_Z \leq \frac{1}{E(\Omega, K)}\|E_t\nabla E\|_H \tag{3.20}$$

where $E(\Omega, K) = KC(\Omega)$. □

3.4.2 Neumann case

Theorem 3.4.3. *U_0 obtained in Theorem 3.3.6 and Theorem 3.3.7 satisfies*

$$\|U_0\|_Z \leq C\|E_t\nabla E\|_H$$

where constant C depends on Ω and the smoothing parameter K.

Proof. For the Neumann Case we have seen from Theorem 3.3.6 and Theorem 3.3.7 that the Bi-linear form $A(U, V)$ is coercive in Z. So there exists a constant $D = D(\Omega, K) > 0$ such that

$$F(U_0) = A(U_0, U_0) \geq D(\Omega, K)\|U_0\|_Z^2 \tag{3.21}$$

where $F(U_0) = E_t(\nabla E.U_0)$. Therefore

$$\begin{aligned}
\|U_0\|_Z^2 &\leq \frac{1}{D(\Omega, K)}F(U_0) \\
&\leq \frac{1}{D(\Omega, K)}\|E_t\nabla E\|_H\|U_0\|_H \\
&\leq \frac{1}{D(\Omega, K)}\|E_t\nabla E\|_H\|U_0\|_Z
\end{aligned}$$

Hence the following estimate holds

$$\|U_0\|_Z \leq \frac{1}{D(\Omega, K)}\|E_t\nabla E\|_H \tag{3.22}$$

□

Comparing the expressions of (3.20) and (3.22), we find that both the estimates are the same except for the constants $E(\Omega)$ and $D(\Omega, K)$. Even the constants depend on the domain Ω and K. So the two estimates for the Dirichlet and the Neumann case are compatible with each other. Hence we see that U_0 depends continuously on the given data i.e the image derivatives.

3.5 Conclusion

In this chapter, we have determined existence of a unique minimizer for the optical flow functional (2.2). For Dirichlet boundary conditions, showing such an existence was straightforward whereas for Neumann boundary conditions, some conditions were required to be imposed on the image sequence E under which a unique minimizer exists. We also derived stability estimates on the minimizer. We have seen in the previous chapter that the finite difference method of Horn and Schunck does not recover fluid flows accurately. In the next chapter we propose an alternate way of tracking fluid flows using the finite element method.

Chapter 4

Finite Element Method for Optical Flow Problem

4.1 Introduction

In Chapter 2 we found that the finite difference iterative scheme for computing optical flow for a given sequence of images gave huge errors. This means that the iterative method fails to capture the motion of the scalars representing image sequences accurately. A plausible reason could be that the finite difference approximation to the Laplacian was obtained using a weighted average of eight neighboring points, leading to inaccurate velocities in directions away from these neighboring points. Thus there is a need of a suitable method for recovery of fluid flow using optical flow techniques. In this chapter we shall discuss the performance of finite element method for determining the fluid flow velocity. We use it to determine the constant flow as in Chapter 2 and compare the results obtained with the Horn and Schunck method.

4.2 Approximation via the Galerkin method

The weak formulation of a pde set on a domain Ω can be written as: find $u \in V$ such that

$$a(u, v) = F(v) \qquad \forall v \in V \tag{4.1}$$

where V is an appropriate Hilbert space, $a(,\cdot,) : V \times V \to \mathbb{R}$ is a continuous bi-linear form, $F(\cdot) : V \to \mathbb{R}$ is a continuous linear functional. Suppose the bi-linear form $a(,\cdot,)$ is coercive. Then under the above hypotheses the Lax-Milgram theorem(Th.3.3.4) ensures existence and uniqueness of the solution.
Let V_h be a family of Hilbert spaces that depends on a positive parameter h, s.t.

$$V_h \subseteq V, \quad \dim V_h = N_h < \infty, \qquad \forall h > 0$$

The approximate problem is to find $u_h \in V_h$ such that

$$a(u_h, v_h) = F(v_h) \qquad \forall v_h \in V_h \tag{4.2}$$

Such type of approximate problem is called the *Galerkin problem*. Let us denote with $\{\phi_j, j = 1, 2, ..., N_h\}$ a basis of V_h. Then it is sufficient that (4.1) be verified for each function of the basis, as all the functions in V_h can be written as a linear combination of the ϕ_j. Then we have,

$$a(u_h, \phi_i) = F(\phi_i), \qquad i = 1, 2, ..., N_h \tag{4.3}$$

As $u_h \in V_h$,

$$u_h(x) = \sum_{j=1}^{N_h} u_j \phi_j(x), x \in \Omega$$

where the $u_j, j = 1, ..., N_h$ are the unknown coefficients. The equations (4.3) then become

$$\sum_{j=1}^{N_h} u_j a(\phi_j, \phi_i) = F(\phi_i), \quad i = 1, 2, ..., N_h \tag{4.4}$$

We denote A by the matrix(called $stiffness\ matrix$) with elements

$$A_{ij} = a(\phi_j, \phi_i)$$

and by f the vector with components $f_i = F(\phi_i)$. If we denote by u the vector having as components the unknown coefficients , (4.4) is equivalent to the linear system

$$Au = f \tag{4.5}$$

We will now show some properties of the matrix A under some given conditions which will enable us to check for the existence of a unique solution of (4.1).

Theorem 4.2.1. *If the bi-linear form $a(,\cdot,)$ is coercive then the matrix A associated to the discretization of (4.1) with the Galerkin method is positive definite.*

Proof. A matrix $B \in \mathbb{R}^{n\times n}$ is said to be positive definite if

$$v^T Bv \geq 0 \quad v \in \mathbb{R}^n \text{ and } v^T Bv = 0 \text{ iff } v = 0 \tag{4.6}$$

Let $v = (v_i) \in \mathbb{R}^{N_h}$. We have by the bi-linearity and coercivity of the form $a(,.,)$,

$$\begin{aligned} v^T Av &= \sum_{j=1}^{N_h}\sum_{i=1}^{N_h} v_i A_{ij} v_j \\ &= \sum_{j=1}^{N_h}\sum_{i=1}^{N_h} v_i a(\phi_j, \phi_i) v_j \\ &= \sum_{j=1}^{N_h}\sum_{i=1}^{N_h} a(v_j\phi_j, v_i\phi_i) \\ &= a(\sum_{j=1}^{N_h} v_j\phi_j, \sum_{i=1}^{N_h} v_i\phi_i) \\ &= a(v_h, v_h) \\ &\geq \alpha\|v_h\|_V^2 \geq 0. \end{aligned}$$

where $v_h(x) = \sum_{j=1}^{N_h} v_j\phi_j(x) \in V_h$. Moreover, if $v^T Av = 0$ then by what we have just obtained,

$$\begin{aligned} &\|v_h\|_V^2 = 0 \\ &\Rightarrow v_h = 0 \\ &\Rightarrow v = 0 \end{aligned}$$

□

Property 4.2.1. *The matrix A is symmetric if and only if the bi-linear form $a(,\cdot,)$ is symmetric.*

Proof. $A_{ij} = a(\phi_i, \phi_j) = a(\phi_j, \phi_i) = A_{ji}$. Hence A is symmetric if and only if the bi-linear form $a(,\cdot,)$ is symmetric. □

4.3 Analysis of the Galerkin method

In this section we will briefly discuss about three of the fundamental properties of Galerkin method:

1. Existence and uniqueness of the discrete solution u_h.
2. Stability of the discrete solution u_h.
3. Convergence of u_h to the exact solution u of problem (4.1) for $h \to 0$.

4.3.1 Existence and uniqueness

The Lax-Milgram theorem (theorem 3.3.4) holds for any Hilbert space ,hence, in particular for the space V_h. Furthermore the bi-linear form $a(,.,)$ and the functional $F(.)$ are the same as in the variational problem (4.1). Thus the hypotheses required by the Lax-Milgram theorem are fulfilled. The following result can be then derived:

Corollary 4.3.1. *If the bi-linear form $a(,.,)$ is coercive then the solution of the Galerkin problem (4.2) exists and is unique.*

4.3.2 Stability

Corollary 4.3.1 helps us to prove the following stability result.

Corollary 4.3.2. *Under the hypotheses of Corollary 4.3.1, the Galerkin method is stable, uniformly with respect to h, as the following upper bound holds for the solution*

$$\|u_h\|_V \leq \frac{1}{\alpha}\|F\|_{V'}$$

where α is the coercivity constant for the bi-linear form $a(,.,)$, and $\|F\|_{V'}$ is the norm of the functional F defined as

$$\|F\|_{V'} = \sup_{v \in V \setminus \{0\}} \frac{|F(v)|}{\|v\|_V}$$

Proof. If u_h is almost everywhere equal to zero we are done, else we have by the coercivity of the bi-linear form $a(,.,)$

$$\alpha\|u_h\|_V^2 \leq a(u_h, u_h) = F(u_h) \leq |F(u_h)|$$

Again as F is linear and continuous, we have

$$|F(u_h)| \leq \|F\|_{V'}\|u_h\|_V$$

Hence the result. □

The stability of the method guarantees that the norm$\|u_h\|_V$ of the discrete solution remains bounded for h tending to zero, uniformly with respect to h.

4.3.3 Convergence

We now want to prove that the weak solution of (4.2) converges to the solution of the problem (4.1) when h tends to zero. Consequently,by taking a sufficiently small h, it will be possible to approximate the exact solution u as accurately as desired by the Galerkin solution u_h. We first prove the following consistency property

Lemma 4.3.1 (Céa)**.** *The Galerkin method is strongly consistent, that is*

$$a(u - u_h, v_h) = 0 \quad \forall v_h \in V_h \tag{4.7}$$

Proof. Since $V_h \subseteq V$, the exact solution u satisfies the weak problem (4.1) for each element $v = v_h \in V_h$, hence we have

$$a(u, u_h) = F(v_h) \quad \forall v_h \in V_h. \tag{4.8}$$

By subtracting side to side (4.2) from (4.8), we obtain

$$a(u, v_h) - a(u_h, v_h) = 0 \quad \forall v_h \in V_h.$$

from which, thanks to the bi-linearity of the form $a(,.,)$, (4.7) follows. □

Next we prove a theorem regarding the error committed when the approximate solution u_h is taken instead of the exact solution u.

Theorem 4.3.1. *If u and u_h denote the solutions of (4.1) and (4.2) respectively, then we have*

$$\|u - u_h\|_V \leq \frac{M}{\alpha} \inf_{w_h \in V_h} \|u - v_h\|_V \tag{4.9}$$

where M and α are the constants of continuity and coercivity respectively for the bi-linear form $a(,.,)$.

Proof. If v_h is an arbitrary element of V_h we obtain

$$a(u - u_h, u - u_h) = a(u - u_h, u - v_h) + a(u - u_h, v_h - u_h).$$

The last term is null thanks to (4.7), as $v_h - u_h \in V_h$. Moreover

$$|a(u - u_h, u - v_h)| \leq M\|u - u_h\|_V \|u - v_h\|_V$$

by exploiting the continuity of the bi-linear form. On the other hand, by the coercivity of $a(,\cdot,)$ it follows

$$a(u - u_h, u - u_h) \geq \alpha \|u - u_h\|_V^2$$

hence we have

$$\|u - u_h\|_V \leq \frac{M}{\alpha} \|u - v_h\|_V \quad \forall v_h \in V_h$$

Such inequality holds for all functions $v_h \in V_h$ and therefore we find

$$\|u - u_h\|_V \leq \frac{M}{\alpha} \inf_{v_h \in V_h} \|u - v_h\|_V \tag{4.10}$$

□

It is then evident that in order for the method to converge, it will be sufficient to require that, for h tending to zero, the space V_h tends to "fill"the entire space V. Precisely it must turn out that

$$\lim_{h \to 0} \inf_{v_h \in V_h} \|v - v_h\|_V = 0 \quad \forall v \in V \tag{4.11}$$

The above property is also known as the **density property**. In that case, the Galerkin method is convergent and it can be written that

$$\lim_{h \to 0} \|u - u_h\|_V = 0$$

The space V_h must therefore be carefully chosen in order to guarantee the density property (4.11). Once this requirement is satisfied, convergence will be verified in any case, independently of how u is made; conversely it will be seen later that the speed with which the discrete solution converges to the exact solution will depend, in general, on both the choice of V_h and the regularity of u. In the following section we will try to achieve specifically the above objective.

4.4 The finite element method

Let Ω be a bounded domain in $\mathbb{R}^n$. The goal of this section is to create approximations of the space $H^1(\Omega)$ that depend on a parameter h.

Definition 4.4.1. *A finite element is a triple $(K, \sum, P)$ such that*

1. *$K \subseteq \Omega$ with a Lipschitz continuous boundary ∂K and interior of K is non-empty.*
2. *$\sum$ is a finite set of linear forms over $C^\infty(K)$. The set $\sum$ is said to be the set of degrees of freedom of the finite element.*
3. *P is a finite dimensional space of real-valued functions over K such that $\sum$ is $P-$unisolvent i.e if $\sum = \{\phi_i\}_{i=1}^N$ and $\alpha_i, 1 \leq i \leq N$ are any scalars, then there exists a unique function $p \in P$ such that*
$$\phi_i(p) = \alpha_i \quad 1 \leq i \leq N \tag{4.12}$$

(4.12) of Definition (4.4.1) is equivalent to the conditions that dim $P = N =$ cardinality of $\sum$ and that there exists a set of functions $\{p_j\}_{j=1}^N$ with $\phi_i(p_j) = \delta_{ij} (1 \leq i, j \leq N)$ which forms a basis of P over $\mathbb{R}$. Given any $p \in P$ we may write

$$p = \sum_{i=1}^{N} \phi_i(p) p_i \tag{4.13}$$

4.4.1 Examples of finite elements

We will now give some examples of finite elements which will be used in the optical flow problem.But before that we define the following

Definition 4.4.2. *An n-simplex is the convex hull in $\mathbb{R}^n$ of $(n+1)$ points $\{a_j\}_{j=1}^{n+1}$ such that if $a_j = \{a_{kj}\}_{k=1}^n$ and A is the matrix*

$$A = \begin{pmatrix} a_{11} & a_{12} & \cdots & a_{1,n+1} \\ a_{21} & a_{22} & \cdots & a_{2,n+1} \\ \vdots & \vdots & \ddots & \vdots \\ a_{n1} & a_{n2} & \cdots & a_{n,n+1} \\ 1 & 1 & 1 & 1 \end{pmatrix}$$

then $det(A) \neq 0$

Definition 4.4.3. *Let $k \geq 0$ be an integer. Then, P_k is the space of all polynomials of degree $\leq k$ in $x_1, x_2, ..., x_n$*

i.e.

$$P_k = \{p(x_1, x_2, ..., x_n) = \sum_{i_1, i_2, .., i_n \geq 0, i_1 + i_2 + .. + i_n \leq k} a_{i_1 i_2 .. i_n} x_{i_1}^{i_1} x_{i_2}^{i_2} .. x_{i_n}^{i_n} \text{ with } a_{i_1 i_2 .. i_n} \in \mathbb{R}\}$$

.

Example 4.4.1 (The n-simplex of Type 1)**.** *Let K be an n-simplex. Let $P_k = P_1$. We define a set $\sum = \{p(a_i); 1 \leq i \leq n+1\}$ of degrees of freedom for $p \in P_k$, where $\{a_i\}_{i=1}^{n+1}$ are the vertices of K. The set $\sum$ determines every polynomial $p \in P_k$ uniquely. Hence $(K, \sum, P_k)$ is a finite element of Type 1.*

Example 4.4.2 (The n-simplex of Type 2)**.** *Let K be an n-simplex with vertices $\{a_i\}_{i=1}^{n+1}$. Let $a_{ij}(i<j)$ be the mid-points of the line joining a_i and a_j i.e.$a_{ij}=\frac{1}{2}(a_i+a_j)$. Let $P_k=P_2$. We define for $p\in P_2$, the set $\sum=\{p(a_i),1\le i\le n+1;p(a_{ij}),1\le i<j\le n+1\}$. Then $\sum$ determines $p\in P_2$ completely. Hence $(K,\sum,P_k)$ is a finite element of Type 2*

Similarly we could use n-simplices of Type r to get other forms of finite elements using P_r.

We saw in the above examples that the set of degrees of freedom for a finite element K(which could be a triangle in 2-d or cube in 3-d) has the following types:

Type 1: ϕ_i^0 given by $p\mapsto p(a_i^0)$. The points $\{a_i^0\}$ were the vertices, the mid-points of sides,etc.

Type 2: $\phi_{i,k}^1$ given by $p\mapsto Dp(a_i^1)(\xi_{i,k}^1)$ where $\{a_i^1\}$ are the vertices of the finite element K and $Dp(a_i^1)$ is the total derivative of p at the point (a_i^1).

Type 3: $\phi_{i,kl}^2$ given $p\mapsto D^2p(a_i^2)(\xi_{i,k}^2,\xi_{i,1}^2)$ where $\{a_i^2\}$ are the vertices of the finite element K and $D^2p(a_i^2)$ is the second derivative of p at the point (a_i^1).

In all the above cases $\{a_i^s\}$ for $s=0,1,2$ are points of K and are called the **nodes of the finite element.**

Definition 4.4.4. *A finite element is called a Lagrange finite element if its degrees of freedom are only of Type 1. Otherwise it is called a Hermite finite element.*

As said before that our aim was to create approximations of the space $H^1(\Omega)$, V_h which depend on a parameter h. We will use the finite elements in the above given examples to create the approximate spaces V_h. But before that we need simple inclusions such as $V_h\subset H^1(\Omega)$ or $V_h\subset H_0^1(\Omega)$. We will establish a simple criterion to realize this.

Theorem 4.4.1. *Let ζ_h be a finite triangulation of Ω such that $\overline{\Omega}=\bigcup_{K\in\zeta_h}K$ where the sets K are the finite elements. If for every $K\in\zeta_h$, $P_k\subset H^1(K)$ and $V_h\subset C^0(\overline{\Omega})$, then $V_h\subset H^1(\Omega)$. If in addition $v=0$ on $\partial\Omega$ for all $v\in V_h$, then $V_h\subset H_0^1(\Omega)$.*

Proof. Let $v\in V_h$. Since $v|K\in L^2(K)$ for every $K\in\zeta_h$ it follows that $v\in L^2(\Omega)$. Hence to complete the proof it only remains to show that for $1\le i\le n$, there exist $v_i\in L^2(\Omega)$ such that for each $\phi\in D(\Omega)$ we have,

$$\int_\Omega \phi v_i dx=-\int_\Omega \frac{\partial\phi}{\partial x_i}v dx \tag{4.14}$$

Then it will follow that $\frac{\partial v}{\partial x_i}=v_i$ and hence $v\in H^1(\Omega)$.

However, $v|_K\in P_k\subset H^1(K)$ implies that $\frac{\partial v|K}{\partial x_i}\in L^2(K),1\le i\le n$. Let $\phi\in D(\Omega)$. Since the boundary ∂K of any K of the triangulation is Lipschitz continuous, we apply integration by parts to get

$$\int_K \frac{\partial v|K}{\partial x_i}\phi dx=-\int_K (v|K)\frac{\partial\phi}{\partial x_i}dx+\int_{\partial K}(v|_K)\phi\nu_{i,K}d\nu_K$$

where $d\nu_K$ is the measure on ∂K and $\overline{\nu}=(\nu_{1,K},....,\nu_{n,K})$ is the outer normal on ∂K Summing over all the finite elements K, we get

$$\begin{aligned}\int_\Omega \phi v_i dx&=\sum_{K\in\zeta_h}\int_K \phi\frac{\partial v|_K}{\partial x_i}dx\\&=-\int_\Omega\frac{\partial\phi}{\partial x_i}v dx+\sum_{K\in\zeta_h}\int_{\partial K}(v|_K)\phi\nu_{i,K}d\nu_K\end{aligned}$$

where v_i is the function whose restriction to each K is $\frac{\partial v|_K}{\partial x_i}$.

The summation on the right-hand side of the above equation is zero for the following reasons:

On the boundary $\partial\Omega$, since $\phi \in D(\Omega)$, the integral corresponding to $\partial K \cap \partial\Omega$ is zero. So the problem, if any, is only on the other portion of the boundary of each K. However, these always occur as common boundaries of adjacent finite elements. The value of $v|_K$ on the common boundary of two adjacent finite elements is the same ($V_h \subset C^0(\overline{\Omega})$). But the outer normals are equal and opposite from orientation considerations.

Hence the contributions from each K along the common boundaries cancel one another. Thus the summation yields only zero. Hence v_i satisfies (4.14) for $1 \leq i \leq n$, and clearly $v_i \in L^2(\Omega)$. The last part of the theorem follows from the characterization of $H_0^1(\Omega)$ spaces. $\square$

4.4.2 Finite element spaces

Now that we have obtained the above inclusions we proceed to give examples of some finite element spaces which approximate the space $H^1(\Omega)$ or $H_0^1(\Omega)$. Before that we consider some assumptions on the triangulation ζ_h of the domain Ω. The h parameter is related to the spacing of the triangulation. We set $h_K = diam(K)$ for each $K \in \zeta_h$, where $diam(K) = \max_{x,y \in K} |x - y|$ is the diameter of the element K. Now we define $h = \max_{K \in \zeta_h} h_K$. Moreover, we will impose the requirement that the triangulation satisfy the following regularity condition. Let ρ_K be the diameter of the circle inscribed in the triangle K (also called the sphericity of K); a family of triangulations $\{\zeta_h, h > 0\}$ is said to be regular if, for a suitable $\delta > 0$, the condition

$$\frac{h_K}{\rho_K} \leq \delta \quad \forall K \in \zeta_h \tag{4.15}$$

is verified. This condition instantly excludes highly deformed triangles. Henceforth we will be using such regular grids.

Now we consider the following family of spaces

$$X_h^r = \{v_h \in C^0(\overline{\Omega}) : v_h|_K \in P_r \quad \forall K \in \zeta_h\}, \quad r = 1, 2, ... \tag{4.16}$$

having denoted by P_r the space of polynomials with degree lower than or equal to r in all the variables. The spaces X_h^r are all subspaces of $H^1(\Omega)$ as they are constituted by differentiable functions except for at most a finite number of points(the vertices x_i of the triangulation ζ_h). They represent possible choices for the space V_h, provided that the boundary conditions are properly incorporated. The fact that the functions of X_h^r are locally(element-wise) polynomials will make the stiffness matrix A in (4.5) easy to compute.

To make the stiffness matrix a sparse matrix, we usually choose a basis $\{\phi_i\}$ for the X_h^r space such that the support of each $\{\phi_i\}$ have non-empty intersection only with that of a negligible number of other functions in the basis. It is also convenient that the basis be Lagrangian: in that case, the coefficients of the expansion of a generic function $v_h \in X_h^r$ on the basis itself will be the values taken by v_h in carefully chosen points, which we call nodes and which might form a superset of the vertices of ζ_h.

We can also define another kind of finite element spaces for rectangular finite elements of type r as described in Section 4.4

$$\overline{X_h^r} = \{v_h \in C^0(\overline{\Omega}) : v_h|_K \in Q_r \quad \forall K \in \zeta_h\}, \quad r = 1, 2, ... \tag{4.17}$$

having denoted by Q_r the space of polynomials with degree lower than or equal to r in each variable. The spaces X_h^r are also subspaces of $H^1(\Omega)$ as they are constituted by differentiable functions except for at most a finite number of points(the vertices of the rectangulation ζ_h). We again choose a Lagrangian basis for the space so that our stiffness matrix is a sparse matrix.

4.5 Interpolation Theory

In the previous section we have outlined the internal approximation method for $H^1(\Omega)$. We are naturally interested in the convergence of the solution $u_h \in V_h$ to the global solution $u \in H^1(\Omega)$. As a key step in this analysis we obtained the error estimate (4.10)

$$\|u - u_h\|_{H^1} \leq \frac{M}{\alpha} \inf_{v_h \in V_h} \|u - v_h\|_{H^1}$$

Let $v \in C^0(\overline{\Omega})$. We now define interpolant of v in the space of X_h^1 determined by the triangulation ζ_h as the function $\Pi_h^1 v$ such that $\Pi_h^1 v(N_i) = v(N_i)$ for each node N_i of ζ_h for $i = 1, 2, ..., N_h$. If $\{\phi_i\}$ is the Lagrangian basis of the space X_h^1, then

$$\Pi_h^1 v(x) = \sum_{i=1}^{N_h} v(N_i)\phi_i(x)$$

The operator $\Pi_h^1 : C^0(\overline{\Omega}) \to X_h^1$, associating a continuous function v to its interpolant $\Pi_h^1 v$ is called interpolation operator.

Analogously we can define an operator $\Pi_h^r : C^0(\overline{\Omega}) \to X_h^r$, for each integer $r \geq 1$. Having denoted by Π_K^r, the local interpolation operator associated to a continuous function v the polynomial $\Pi_K^r v \in P_r(K)$, interpolating v in the degrees of freedom of the element $K \in \zeta_h$, we define

$$\Pi_h^r v \in X_h^r : \quad \Pi_h^r|_K = \Pi_K^r(v|_K) \quad \forall K \in \zeta_h$$

From (4.10) we get

$$\begin{aligned} \|u - u_h\|_{H^1(\Omega)} &\leq \frac{M}{\alpha} \inf_{v_h \in V_h} \|u - v_h\|_{H^1(\Omega)} \\ &= \frac{M}{\alpha} \left[\sum_{K \in \zeta_h} \|u - \Pi_h^r|_K\|^2_{H^1(K)} \right]^{\frac{1}{2}} \end{aligned} \tag{4.18}$$

Thus the problem of estimating $\|u - u_h\|_{H^1(\Omega)}$ is reduced to the problem of estimating $\|u - \Pi_h^r|_K\|_{H^1(K)}$. We will now state the the interpolation error estimates and an estimate for the error $\|u - u_h\|_{H^1(\Omega)}$. The proofs can be found in [80]. To prove these estimates, regularity of the triangulation is used as well as affine and invertible transformation $F_K : \widehat{K} \to K$ between the reference triangle $\widehat{K}$ and the generic triangle K (see Fig 4.1) is used. Such a map is defined by $F_K(\widehat{x}) = B_K\widehat{x} + b_K, B_K \in \mathbb{R}^{2\times 2}, b_K \in \mathbb{R}^2$, and it satisfies the relation $F_K(\widehat{K}) = K$.

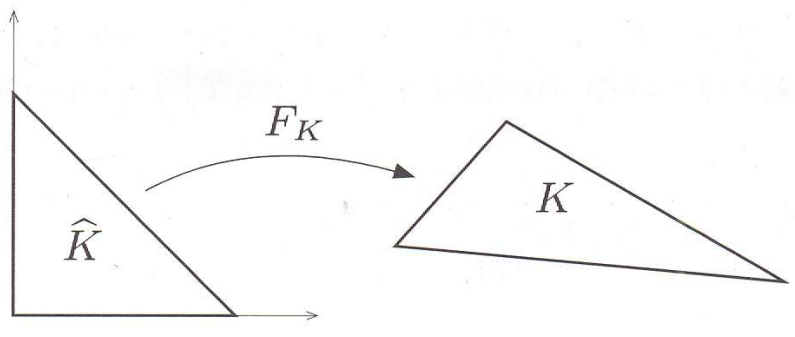

Figure 4.1: The map F_K between the reference triangle $\widehat{K}$ and the generic triangle K [80]

Theorem 4.5.1 (Global estimate for the interpolation error). *Let $\{\zeta_h\}_{h>0}$ be a family of regular grids of the domain Ω and let $m = 0, 1$ and $r \geq 0$. Then there exists a constant $C = C(r,m,\widehat{K}) > 0$ such that*

$$|v - \Pi_h^r v|_{H^m(\Omega)} \leq C \left(\sum_{K \in \tau_h} h_K^{2(r+1-m)} |v|^2_{H^{r+1}(K)} \right)^{\frac{1}{2}} \qquad \forall v \in H^{r+1}(\Omega)$$

In particular we obtain

$$|v - \Pi_h^r v|_{H^m(\Omega)} \leq C h^{r+1-m} |v|_{H^{r+1}(\Omega)} \qquad \forall v \in H^{r+1}(\Omega)$$

Theorem 4.5.2 (Error estimate for the finite element solution). *Let $u \in V$ be the exact solution of the variational problem (1) and u_h be its approximate solution using the finite element method of degree r. If $u \in H^{r+1}(\Omega)$, then the following a priori error estimate hold*

$$\|u - u_h\|_{H^1(\Omega)} \leq \frac{M}{\alpha} C \left(\Sigma_{K \in \tau_h} h_K^{2r} |u|^2_{H^{r+1}(K)} \right)^{\frac{1}{2}}$$

$$\|u - u_h\|_{H^1(\Omega)} \leq \frac{M}{\alpha} C h^r |u|_{H^{r+1}(\Omega)}$$

C is a constant independent of h and u.

4.6 Finite element method for the Optical flow problem (2.2)

Now that we have the required pre-requisites, we will solve the optical flow problem (6.1) using the finite element method. We showed in Theorem 3.2.2 that minimizing the functional J is equivalent to finding a solution of $J'(U) = 0$. We also showed in Section 3.3.2 that we can write $J'(U)[V] = 0 \quad \forall V \in Z$ as $A(U, V) = F(V)$ where $A(U, V) : Z \times Z \to \mathbb{R}$ is a symmetric bi-linear form associated to the functional J given by (3.7) and $F(V) : Z \to \mathbb{R}$ is a linear form given by (3.8). The approximate problem can be written as: find $U_h \in Z_h$ such that

$$A(U_h, V_h) = F(V_h) \quad \forall V_h \in Z_h$$

where Z_h is a suitable approximation of the space Z depending on a parameter h. In the finite element setup, the optical flow problem can be formulated as: find $U_h \in Z_h$ such that

$$\int_\Omega (\nabla E \cdot U_h)(\nabla E \cdot V_h) + K \int_\Omega (\nabla U_h \cdot \nabla V_h) = -\int_\Omega E_t (\nabla E \cdot V_h) \quad \forall V_h \in Z_h$$

We take the approximation of the space Z as the space $Z_h = (\overline{X_h^1})^2$ and use Type 1 rectangular finite elements. The characteristic Lagrangian basis functions are characterized by the following property $\Phi_i \in Z_h$ such that $\Phi_i(x_j) = \delta_{ij}, i, j = 0, 1, ..., N_h$ where N_h are the number of nodes and δ_{ij} being the Kronecker delta. The function Φ_i is therefore piecewise linear in each coordinate, as we have rectangular finite elements, and equal to one at each x_i and zero at the remaining nodes of the triangulation.

4.6.1 Data

Our domain Ω is the unit square in $\mathbb{R}^2$ i.e. $[0, 1] \times [0, 1]$. We have taken our image at time t_0 to be E_0 defined as

$$E_0(x, y) = E(x, y, 0) = e^{[-50 * \{(x-0.5)^2 + (y-0.5)^2\}]}$$

The exact solution is chosen to be the constant velocity $(u, v) = (1, 1)$. At time t, the image will be given by,

$$E(x, y, t) = E_0(x - ut, y - vt) = E(x - ut, y - vt, 0)$$

using the characteristic method. We use the Neumann boundary conditions which are natural boundary conditions.

4.6.2 Programming procedure

We use deal.II libraries in C++ programming language to solve the problem. We refine the domain Ω uniformly three times i.e in the first step we divide Ω into four equal cells. In the second step we divide each of the four cells into equal four cells and so on uptil three times. So the total number of active cells will be 64. Then the degrees of freedom in the refined grid are calculated and we now form the stiffness matrix A and the right hand side f as in (4.5) and hence the linear equation

$$AU = f, U \in T. \tag{4.19}$$

It will be a sparse matrix. It is invertible under the conditions for Neumann boundary conditions in Chapter 3 as the associated bi-linear form is coercive (Theorem 4.2.1). Then the linear system in (4.19) is solved using the conjugate gradient method (See Appendix C). A preconditioner is also used to improve on the condition number of the matrix $\overline{A}$.

4.6.3 Results

With Neumann boundary conditions, Fig 4.2 and Fig 4.3 shows the velocity vector plots for $K = 0.9,\ 1.5$

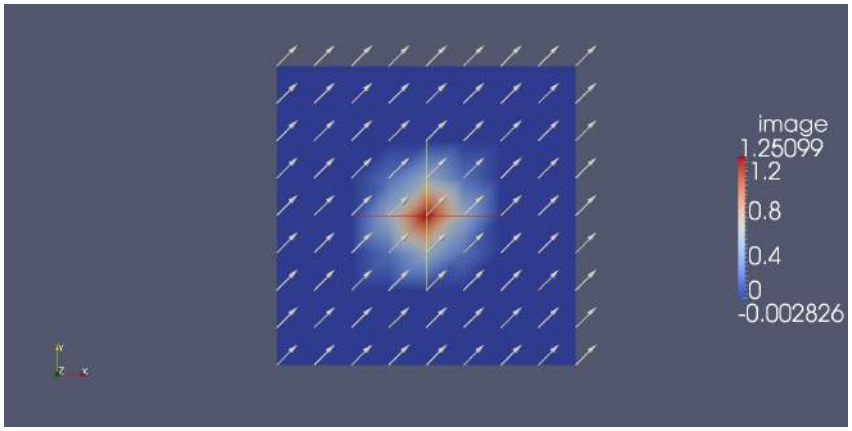

Figure 4.2: Image along with the velocity vectors for $K = 0.9$.

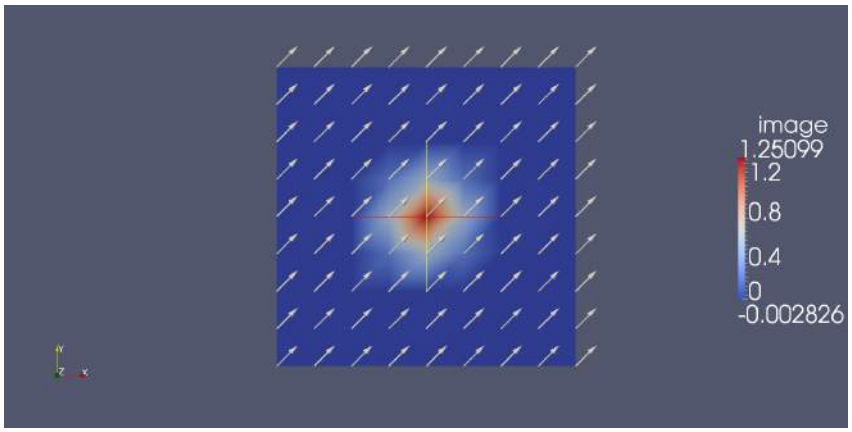

Figure 4.3: Image along with the velocity vectors for $K = 1.5$.

We can see that we recover the velocity with great accuracy. This is also reflected in Table 4.1 through the relative L^2 errors. We changed the smoothing parameter K and calculated the relative L^2 error in the velocity and the advection error. The results are shown in Table 4.1

K	Relative L^2 Error	Advection Error
0.1	5.5502 e-13	9.57645 e-26
0.2	1.35063 e-13	6.84743 e-27
0.3	2.2402 e-13	3.27 e-26
0.9	1.59248 e-13	1.62616 e-27
1	2.21603 e-13	3.56386 e-28
1.1	2.22272 e-13	3.58421 e-28
1.2	2.65804 e-13	5.19862 e-28
1.8	3.47395 e-13	4.95675 e-28
1.9	3.67301e-13	6.14862 e-28
2	4.06641 e-13	8.57827 e-28

Table 4.1: Variation of relative L^2 error and Advection error with the smoothing parameter K

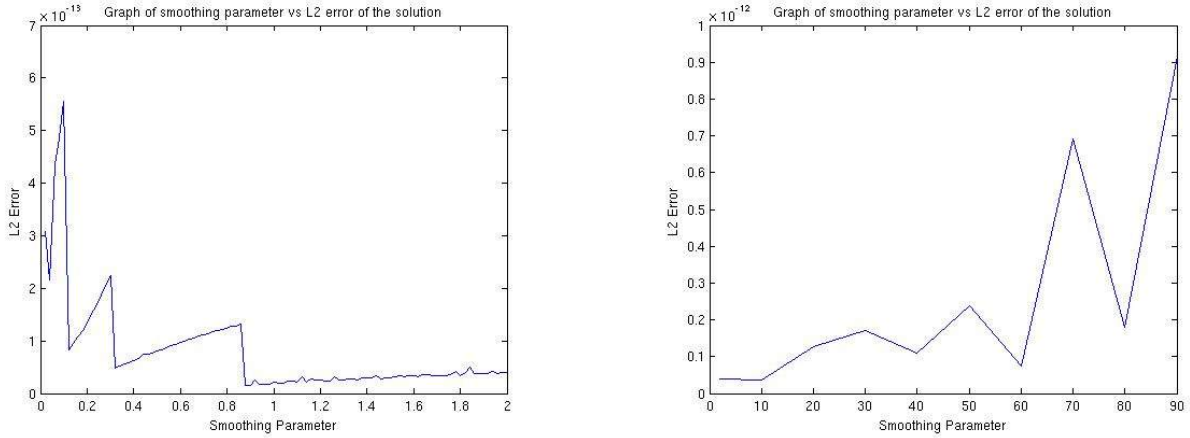

(a) K small

(b) K large

Figure 4.4: Graph of L^2 error vs K.

4.6.4 Conclusions

The order of the advection error is 10^{-28} and the order of the L^2 error is 10^{-13} which suggests that the optical flow velocities obtained using the finite element method satisfy the advection equation and are very close to the actual velocity. Figure 4.4 shows the graph plots of relative L^2 error versus K showing the excellent recovery of the constant flow. So we see that the finite element method is better than the finite difference method in the recovery of fluid flows. So we now proceed to the next chapter to solve the cloud motion problem emulating the optical flow techniques that have been tested uptil now.

Chapter 5

Finite Element method for the Potential flow problem

5.1 Introduction

In this chapter, our aim is to recover incompressible fluid flows. This leads to the inclusion of fluid flow constraints in our model.We assume that the fluid flow is potential and incompressible. We will solve it numerically using the finite element method and test it on constant flows and point vortex flows and formulate a minimization problem. Numerical experiments are performed on constant flows and point vortex flows using finite element method and finally the results are analysed.

5.2 Constraints

Let E be a brightness pattern. We will again assume that brightness of a particular point in the pattern is constant,so

$$\frac{dE}{dt} = 0$$

This implies E satisfies

$$E_x u + E_y v + E_t = 0 \tag{5.1}$$

Let $U = (u, v)$ be the optical flow velocity. Then by our assumption on the flow

$$\begin{aligned} U &= \nabla\Phi \\ \Delta\Phi &= 0 \end{aligned} \tag{5.2}$$

Now to solve for Φ we have to give a boundary condition on it and the natural choice would be to specify the normal rate of change of flux on the boundary. The condition can be written as

$$\nabla\Phi \cdot n = g \tag{5.3}$$

where g is some arbitrary function and n is the unit normal on the boundary of Ω. If U belongs to $Z = (H^1(\Omega))^2$ then g belongs to $H^{\frac{1}{2}}(\partial\Omega)$. Our aim is to determine a suitable g so that U satisfies (5.1), (5.2) and (5.3). Now to solve for Φ from (5.2) and (5.3) we have another constraint to be satisfied i.e

$$\int_{\partial\Omega} g = 0 \tag{5.4}$$

We will now modify the HS functional (6.1) and try to solve the problem incorporating the above constraints.

5.3 Problem Statement

Let $E : \Omega \times \mathbb{R}^+ \longrightarrow \mathbb{R}$, be an image sequence, where $\Omega \subseteq \mathbb{R}^2$ is a bounded domain of the spatial coordinates and $\mathbb{R}^+$ is the domain of the time coordinate. We estimate the optical flow, the field $U \in H^1(\Omega)$ of optical velocities over Ω, by minimizing the functional,

$$J(U) = \frac{1}{2}\int_\Omega (E_t + \nabla E \cdot U)^2 + \frac{K}{2}\int_{\partial\Omega} g^2 \tag{5.5}$$

subject to the constraints (5.2), (5.3) and (5.4), where K is a positive constant.

There are two terms in the functional. The first term comes as a result of the fact that brightness of a particular point in the image pattern is constant. The second term is added to have a control over the normal rate of change of optical flow flux on the boundary.

5.4 Optimization using Lagrange Multipliers

The functional J is to be minimized subject to PDE constraints. This is done by the use of Lagrange multipliers [46]. We first write down the weak form of (5.2). Multiplying (5.2) with a test function $\psi \in H^1(\Omega)$, integrating by parts and using the boundary condition (5.3), we get

$$\int_{\partial\Omega} g\psi d\nu - \int_\Omega \nabla\Phi \cdot \nabla\psi dxdy = 0 \tag{5.6}$$

Hence to determine the optimal solution, the auxiliary functional can be written as

$$\widetilde{J}(\Phi, \psi, \lambda, g) = \frac{1}{2}\int_\Omega (E_t + \nabla E \cdot \nabla\Phi)^2 dxdy + \frac{K}{2}\int_{\partial\Omega} g^2 d\nu + \int_{\partial\Omega} g\psi d\nu - \int_\Omega \nabla\Phi \cdot \nabla\psi dxdy + \lambda \int_{\partial\Omega} g, \tag{5.7}$$

where $\psi \in H^1(\Omega)$ is the Lagrange multiplier corresponding to the constraint (5.2) and (5.3) and $\lambda \in \mathbb{R}$ is the Lagrange multiplier for the constraint (5.4).

5.5 Optimality conditions obtained after minimization of $\widetilde{J}$

Taking the Gateaux derivative of $\widetilde{J}$ in (5.7) wrt ψ, Φ, λ, g, the standard optimality conditions [100] are

$$\frac{\partial\widetilde{J}}{\partial\psi} = 0,\ \frac{\partial\widetilde{J}}{\partial\Phi} = 0,\ \frac{\partial\widetilde{J}}{\partial\lambda} = 0,\ \frac{\partial\widetilde{J}}{\partial g} = 0. \tag{5.8}$$

The first equation in (5.8) gives the weak PDE satisfied by Φ

$$\int_{\partial\Omega} g\widetilde{\psi} d\nu - \int_\Omega \nabla\Phi \cdot \nabla\widetilde{\psi} dxdy = 0, \quad \widetilde{\psi} \in H^1(\Omega) \tag{5.9}$$

The second equation in (5.8) gives the weak PDE satisfied by ψ

$$-\int_\Omega \nabla\psi \cdot \nabla\widetilde{\Phi} + \int_\Omega (E_t + \nabla E \cdot \nabla\Phi)(\nabla E \cdot \nabla\widetilde{\Phi}) = 0, \quad \forall\widetilde{\Phi} \in H^1(\Omega) \tag{5.10}$$

The third equation in (5.8) gives the compatibility condition

$$\int_{\partial\Omega} g = 0 \tag{5.11}$$

The final equation in (5.8) gives the optimality condition

$$\int_{\partial\Omega} (Kg + \psi + \lambda)\widetilde{g} = 0, \quad \forall\widetilde{g} \in H^{\frac{1}{2}}(\partial\Omega) \tag{5.12}$$

(5.12) gives us

$$Kg + \psi + \lambda = 0, \qquad \text{on } \partial\Omega. \tag{5.13}$$

This implies

$$\int_{\partial\Omega} (Kg + \psi + \lambda) d\nu = 0$$

Using (5.11) we get

$$\lambda \int_{\partial\Omega} d\nu = -\int_{\partial\Omega} \psi d\nu$$

This gives

$$\lambda = -\frac{\int_{\partial\Omega} \psi d\nu}{\int_{\partial\Omega} d\nu}$$

Therefore we get

$$g = \frac{1}{K}\left(-\psi + \frac{\int_{\partial\Omega} \psi d\nu}{\int_{\partial\Omega} d\nu}\right) \qquad \text{on } \partial\Omega. \tag{5.14}$$

5.6 Finite Element Method

Now that we have got the equations (5.9), (5.10), (5.11), (5.12), (5.14), we will solve them using finite element method to recover the optical flow velocity for a given image pattern. We use Freefem++ software to achieve this objective. But first we will write down the original space Z where we are trying to find the solution, the approximate space Z_h depending on parameter h and the weak formulations for Φ, ψ in the space Z_h.

Our domain Ω is the unit square in $\mathbb{R}^2$. We take $Z = (H^1(\Omega))^2$ and the approximation of the space Z as the space $Z_h = (X_h^1)^2$ where X_h^1 is the space defined in (4.16).

The weak formulation for ψ is

$$-\int_\Omega \nabla\psi\cdot\nabla\psi_h + \int_\Omega (E_t + \nabla E\cdot\nabla\Phi)(\nabla E\cdot\nabla\psi_h) = 0, \quad \forall\psi_h \in X_h^1(\Omega) \tag{5.15}$$

The weak formulation for Φ is

$$\int_{\partial\Omega} g\Phi_h - \int_\Omega \nabla\Phi\cdot\nabla\Phi_h = 0, \quad \forall\Phi_h \in X_h^1(\Omega) \tag{5.16}$$

5.7 Image Data

We have taken our image at time t_0 to be E_0 defined as:-

$$E_0(x, y) = E(x, y, 0) = e^{[-50*\{(x-0.5)^2+(y-0.5)^2\}]}$$

and for testing the accuracy of the method we move the image with a predefined constant velocity of $u = 1.0$ and $v = 1.0$. So at time t, the image will be given by,

$$E(x, y, t) = E_0(x - ut, y - vt) = E(x - ut, y - vt, 0)$$

using the characteristic method.
We define the relative L^2 error in velocity as

$$\text{Relative } L^2 \text{ error} = \frac{\|U_e - U_o\|}{\|U_e\|} \tag{5.17}$$

and the advection error as

$$\text{Advection Error} = \|E_t + U_o \cdot \nabla E\| \tag{5.18}$$

where U_e is the exact velocity and U_o is the obtained velocity and the norm $\|\cdot\|$ is the usual L^2 norm for vector functions.

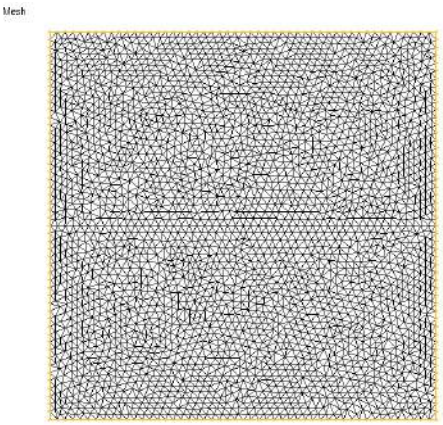

Figure 5.1: Mesh

5.8 Numerical Algorithm

The steps for solving the problem are enumerated below

1. We divide Ω into triangular finite elements.
2. We then give an arbitrary starting value of g and solve for Φ using its weak formulation. We note while solving for Φ we are using Neumann boundary conditions and so the solution is unique upto a constant. To remove ambiguity arising from the constants we modify the weak formulation for Φ as

$$\int_{\partial\Omega} g\Phi_h - \int_{\Omega} \nabla\Phi\cdot\nabla\Phi_h - \epsilon\int_{\Omega}\Phi\Phi_h = 0, \quad \forall\Phi_h \in X_h^1(\Omega)$$

   where $\epsilon = 10^{-10}$. So unless Φ is of order $\frac{1}{\epsilon}$ we satisfy (5.11) and also the solution obtained is unique and it is almost equal to the solution obtained from (5.16).
3. After we get Φ, we substitute it in (5.15) and solve for ψ.
4. We then modify g using (5.14).
5. Now we check the L^2 error of the difference of the modified g and the previous value of g. If the difference is less than a given value of tolerance, then we have obtained the solution Φ and hence the flow velocity $U = (\partial_x(\Phi), \partial_y(\Phi))$ else we use the modified value of g to again solve for Φ, ψ and then repeat the procedure.

5.9 Numerical Results

We divide Ω into triangles as seen in Fig 5.1. The image E is shown in Fig 5.2. Figure 5.3 shows the velocity vector plots for various values of K. We note that for $K = 1$ the magnitude of the velocity vectors are too high which suggests that $K = 1$ is not a good choice. But for $K = 1.1, 1.5, 1.75, 2$ we see that the average magnitude is near to 0.5 and it decreases as we increase K. Table 5.1 shows the relative L^2 errors and the advection errors for different values of K. Our tolerance level is set at 10^{-10}. We can see from above table that if $K \leq 1$ then the method does not converge at all. But even if we increase K then the method converges but as we increase K the relative L^2 error increases, not rapidly. But the advection error decreases as $K \geq 1.1$ even though the order of the error is 10^{-5}. Also time taken to compile is proportional to K. So to have a balance between the control of L^2 error and the advection error we would want to choose K such that the L^2 error is the minimum as the order of the L^2 error is much greater

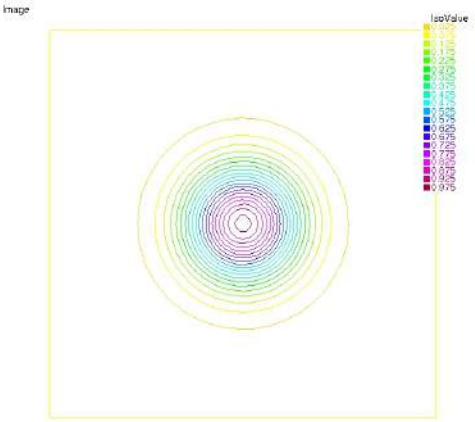

Figure 5.2: Image E

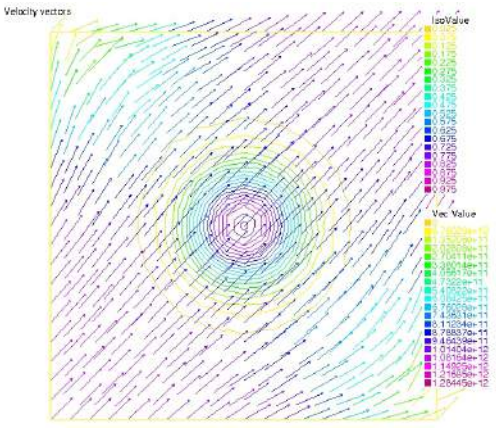

(a) K=1

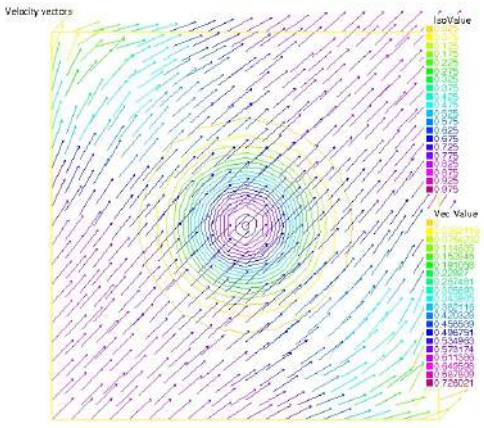

(b) K=1.5

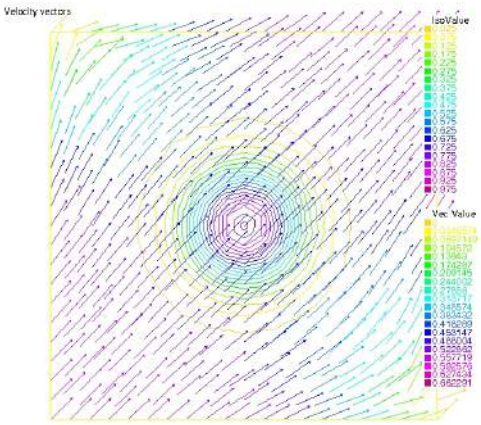

(c) K=1.75

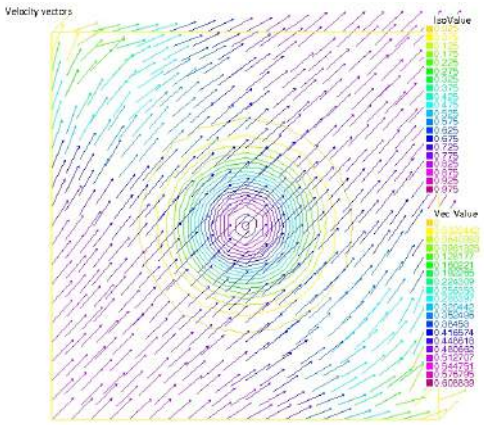

(d) K=2

Figure 5.3: Velocity plots for constant flow

K	Time taken/ Number of steps	Relative L^2 error	Advection error	Method Convergence Status
0.8	315 steps	-	-	No
1	315 steps	-	-	No
1.01	315 steps	-	-	No
1.06	315 steps	-	-	No
1.08	315 steps	-	-	No
1.09	315 steps	-	-	No
1.1	850.45 sec	0.530761	8.53735 e-5	Yes
1.2	47.375 sec	0.550122	8.16886 e-5	Yes
1.5	13.24 sec	0.599979	7.23131 e-5	Yes
1.75	9.23 sec	0.633987	6.599943 e-5	Yes
2	7.31 sec	0.662754	6.06881 e-5	Yes
3	4.33 sec	0.743681	4.59114 e-5	Yes

Table 5.1: Variation of relative L^2 error and advection error with the smoothing parameter K

than the advection error.The results suggest that the optical flow velocity could be sensitive to K. Smaller values of K cannot be taken. Too higher values of K might over-regularize the flow velocity. So there exists an optimal value of K for which the relative L^2 error is the minimum. This is shown in Figure 5.4 From the above results we have an intuitive feeling that the optical flow velocity might depend on K. So we try for another example where the above given image E is subject to a point vortex.

5.10 Flow due to point vortex

We consider the same domain and the same image E. We now introduce a point vortex of strength $\kappa = 100.0$, whose singularity lies at the point $(-1, -1)$ i.e. outside the domain. The velocity components are given as

$$\begin{aligned} u &= -\frac{\kappa(y+1)}{2\pi\left[(x+1)^2+(y+1)^2\right]} \\ v &= \frac{\kappa(x+1)}{2\pi\left[(x+1)^2+(y+1)^2\right]} \end{aligned} \tag{5.19}$$

To test the method, we move the image E with the velocity $U = (u, v)$ according to the advection equation $E_t + U \cdot \nabla E = 0$ and then we will recover the velocity U. The results obtained are shown in Figure 5.5

5.11 Numerical Results

We see a similar trend as we had got for the case of constant flow. We note that for $K = 1$ the magnitude of the velocity vectors are too high which suggests that $K = 1$ is not a good choice. But for $K = 1.1, 1.2, 1.4, 1.8, 2, 2.5, 3$ we see that the average magnitude is near to 1 and it decreases as we increase K. Table 5.2 shows the relative L^2 errors for different values of K. Our tolerance level in this case is set at 10^{-7}. We can see from above table that if $K \leq 1$ then the method does not converge at all. But even if we increase K then the method converges but as we increase K the relative L^2 error increases, not rapidly. Again the time taken to compile is proportional to K. So we would want to choose K such that the L^2 error is the minimum. As in both the cases of constant flow and point vortex flow, we see the same behavior of the

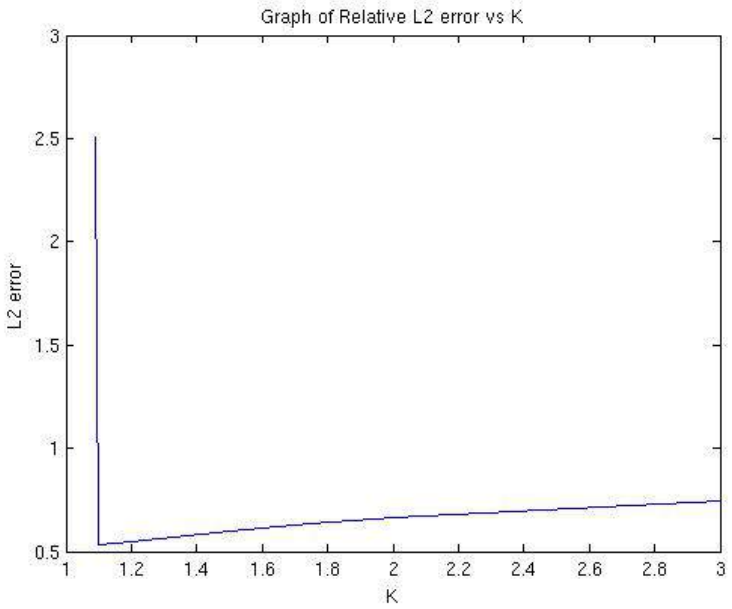

Figure 5.4: Graph of Relative L2 error vs K showing existence of an optimal K

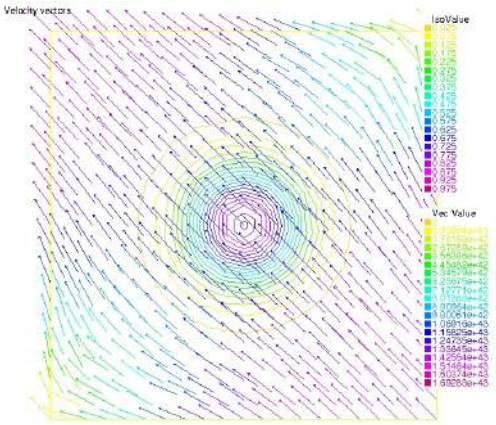

(a) K=0.8

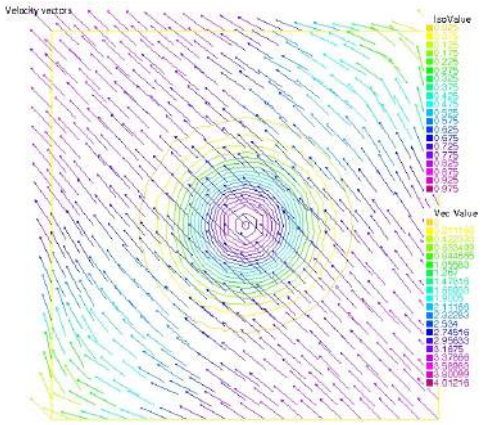

(b) K=1.4

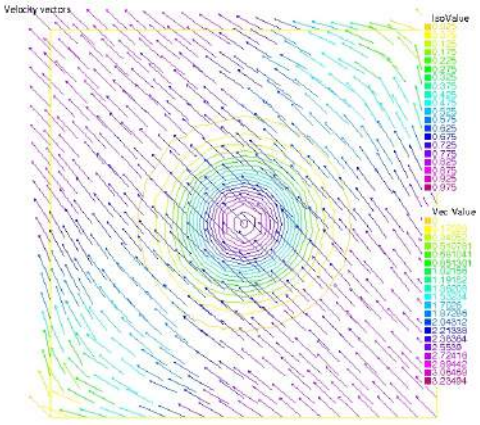

(c) K=2

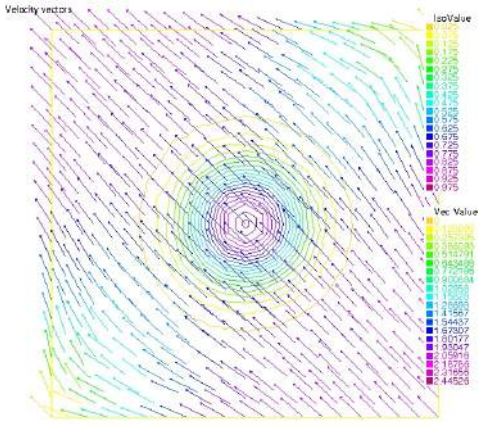

(d) K=3

Figure 5.5: Velocity plots for flow due to point vortex

K	Time taken/ Number of steps	Relative L^2 error	Advection Error	Method Convergence Status
0.8	315 steps	-	-	No
1	315 steps	-	-	No
1.04	315 steps	-	-	No
1.08	315 steps	-	-	No
1.1	869.78 sec	0.562607		Yes
1.2	42.79 sec	0.580036	4.81059 e-4	Yes
1.4	16.3 sec	0.611268	4.36944 e-4	Yes
1.8	8.3 sec	0.662055	3.70100 e-4	Yes
2	6.87 sec	0.682904	3.44042 e-4	Yes
2.5	5.06 sec	0.725437	2.92845 e-4	Yes
3	4.28 sec	0.75802	2.55113 e-4	Yes

Table 5.2: Variation of relative L^2 error with the smoothing parameter K for vortex flow.

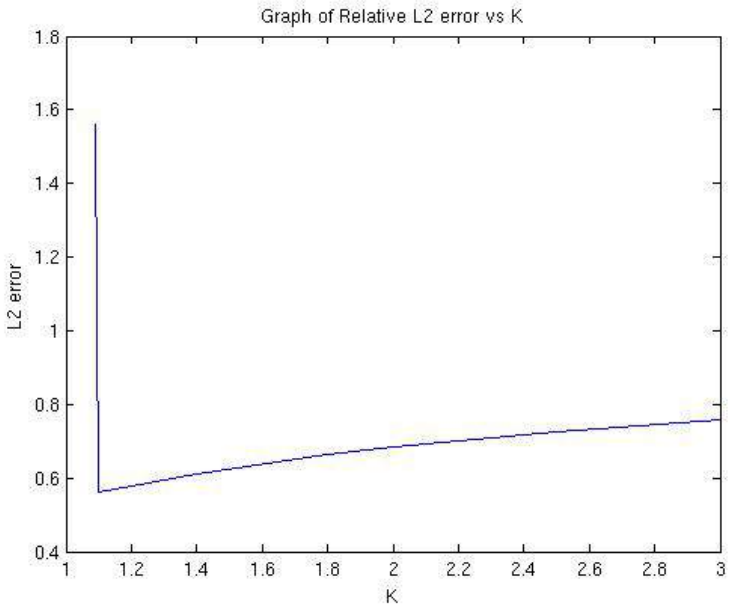

Figure 5.6: Graph of Relative L2 error vs K showing existence of an optimal K for vortex flow.

flow velocity with K we can now predict that for this method we have an universal optimal K which would minimize the L^2 error in the flow velocity. We again plot a graph to see which could be the optimal K. This is shown in Figure 5.6. We compare the two graphs Graph 5.4 and Graph 5.6 and we find that the optimal K lies between 1.1 and 1.2 and for both the cases values are almost equal.

5.12 Conclusions

We formulated a constraint-based minimization problem to recover incompressible flows given a sequence of images of scalars. Additionally, it was assumed that the flow was irrotational and hence it can be given by the potential of some function ϕ. To introduce boundary conditions in the problem, a Neumann boundary condition for the velocity potential was incorporated in the model and put as a control in the minimization problem. The numerical results show that the relative L^2 error in the velocity depends on K and there exists an optimal K for which

the relative L^2 error is the least. A mathematical theory to determine the convergence of the method with respect to K and determining the optimal K would be an interesting problem which the authors plan to address in future. But as the L^2 error in the velocity is of the order 0.5, it suggests that the above method is not that accurate in recovering incompressible flows. One plausible reason could be the boundary condition. The Neumann boundary condition for the velocity potential transforms to the normal component of the velocity on the boundary. There is no information of the tangential velocity component and hence the flow is not well recovered. Hence there is a need to propose a different model for recovering incompressible flows. One way of doing this is to include it as a constraint and, using the boundary velocity information, try and recover the velocity. This method is employed in the next chapter.

Chapter 6

Steady State Flow Recovery

6.1 Introduction

In the previous chapter we found that the recovery of constant optical flow velocities was not accurate assuming potential and incompressible flow constraints. Therefore, in this chapter, we propose an alternate algorithm based on variational methods to recover the optical velocities for flow governed by Stokes and Navier-Stokes equations. We formulate a minimization problem and determine conditions under which unique solution exists. Numerical results using finite element method not only support theoretical results but also show that Stokes flow forced by a potential are recovered almost exactly.

6.2 Variational Formulation

To estimate fluid flow, we trace passive scalars that are propagated by the flow. Examples of such scalars are smoke, brightness patterns of dense rain-bearing clouds whose intensity remains constant atleast for a short time span. These scalars can be represented by a function $E : \Omega \times \mathbb{R}^+ \longrightarrow \mathbb{R}$ so that $E(x, y, t)$ for $(x, y) \in \Omega$ represents a snapshot of the image of the scalars at time $t \in \mathbb{R}^+$. Here Ω is a bounded convex subset of $\mathbb{R}^2$. Let us assume our image $E(x, y, t) \in W^{1,\infty}(\Omega)$, for each t and hence in $L^2(\Omega)$ (as Ω is bounded). Let the field of optical velocities over Ω at a fixed time $t = t_0$ be $U(x, y, t_0) = (u, v)(x, y, t_0)$ and $X = (H^1(\Omega))^2$. Then $U \in X$ is obtained by minimizing the functional,

$$J(U) = \frac{1}{2}\int_\Omega (E_t + U \cdot \nabla E)^2 dxdy + \frac{K}{2}\int_\Omega \|\nabla U\|^2 dxdy, \quad K > 0 \tag{6.1}$$

where E_t and ∇E are evaluated at $t = t_0$, and

$$\|\nabla U\|^2 = \|\nabla u\|^2 + \|\nabla v\|^2$$

Without loss of generality let $t_0 = 0$. The first term in (6.1) represents the constant brightness assumption of the tracers. The second term represents a regularization term for the flow velocities. Such a functional was first considered by Horn and Schunck[49] and subsequently by many others [14, 13, 65, 66, 67, 68] to efficiently estimate rigid body motion. Here it is used to track the underlying fluid flow motion. Such a connection between optical flow and fluid flow tracking is essential because if a proper connection is found then techniques from optical flow to determine high-resolution velocity fields from various images in continuous patterns can be used. To use (6.1) to track fluid flows, we need to include fluid dynamics and enforce proper boundary conditions. Hence we enforce the incompressible fluid flow constraint

$$\nabla \cdot U = 0 \tag{6.2}$$

So the minimization problem can be stated as

$$\min_{U \in X} \quad \{J(U) |\ \nabla \cdot U = 0\} \tag{P}$$

The boundary conditions on the flow velocity could be either Dirichlet or Neumann.

6.3 Existence and Uniqueness Of Minimizer

We show existence of a unique global minimizer for Problem (P). Before that we state some standard definitions and results.

6.3.1 Preliminary Results

Let $(Z, \|\cdot\|_Z)$ be a Banach space.

Theorem 6.3.1. *Let $J : Z \to \mathbb{R} \cup \{-\infty, \infty\}$ be a convex functional on Z. If J is bounded from above in a neighborhood of a point $U_0 \in Z$, then it is locally bounded i.e. each $U \in Z$ has a neighborhood on which J is bounded.*

Definition 6.3.1. *A functional J defined on Z is said to be **locally Lipschitz** if at each $U \in Z$ there exists a neighborhood $N_\epsilon(U)$ and a constant $R(U)$ such that if $V, W \in N_\epsilon(U)$, then*

$$|J(V) - J(W)| \leq R\|V - W\|_Z$$

*If this inequality holds throughout a set $Y \subseteq Z$ with R independent of U then we say that J is **Lipschitz** on Y.*

Theorem 6.3.2. *Let J be convex on Z. If J is bounded from above in a neighborhood of one point of X, then J is locally Lipschitz in Z.*

Theorem 6.3.3. *Let J be convex on Z. If J is bounded from above in an neighborhood of one point of Z, then J is continuous on Z.*

Theorem 6.3.1, 6.3.2, 6.3.3 and Definition 6.3.1 can be found in [82]. The following theorem from [15] is used to establish a unique global minimizer for (P).

Theorem 6.3.4 (Existence and uniqueness of global minimizer)**.** *Let $J : Z \to \mathbb{R} \cup \{-\infty, \infty\}$ be a lower semi-continuous strictly convex functional. Also let J be coercive i.e.*

$$\lim_{\|U\|_Z \to +\infty} J(U) = \infty.$$

Let C be a closed and convex subset of Z. Then J has a unique global minimum over C.

Let us now verify the conditions stated in Theorem (6.3.4) for the functional J in (6.1). Let $H = L^2(\Omega)$, $H_1 = (L^2(\Omega))^2$ and $Z = X$ with norms $\|U\|_H = \|u\|_{L^2} + \|v\|_{L^2}$ and $\|U\|_Z = \|u\|_{H^1} + \|v\|_{H^1}$.

Theorem 6.3.5. *The functional given in (6.1) is strictly convex with respect to U under the assumption that E_x and E_y are linearly independent i.e there does not exist non-zero constants c_1 and c_2 such that $c_1 E_x(x, y) + c_2 E_y(x, y) = 0$, for all $(x, y) \in \Omega$.*

Proof. Let $U_1 = \begin{pmatrix} u_1 \\ v_1 \end{pmatrix}$ and $U_2 = \begin{pmatrix} u_2 \\ v_2 \end{pmatrix}$ where $(\cdot)$ is the usual inner product on $\mathbb{R}^2$. Then for $0 < \alpha < 1$ and $U_1 \neq U_2$, we have

$$\begin{aligned} J(\alpha U_1 + (1-\alpha)U_2) &= \frac{1}{2}\int_\Omega ((\alpha U_1 + (1-\alpha)U_2)\cdot\nabla E) + E_t)^2 dxdy \\ &\quad + \frac{K}{2}\int_\Omega \left[\|\nabla(\alpha u_1 + (1-\alpha)u_2)\|^2 + \|\nabla(\alpha v_1 + (1-\alpha)v_2)\|^2\right] dxdy \\ &\leq \frac{1}{2}\int_\Omega \left[\{(\alpha U_1 + (1-\alpha)U_2)\cdot\nabla E\}^2 + 2E_t^2 + 2E_t\{(\alpha U_1 + (1-\alpha)U_2)\cdot\nabla E\}\right] dxdy \\ &\quad + \frac{K}{2}\int_\Omega \left[\|(\alpha\nabla u_1 + (1-\alpha)\nabla u_2)\|^2 + \|(\alpha\nabla v_1 + (1-\alpha)\nabla v_2)\|^2\right] dxdy \end{aligned}$$

Now

$$\begin{aligned} &\frac{K}{2}\int_\Omega \left[\|(\alpha\nabla u_1 + (1-\alpha)\nabla u_2)\|^2 + \|(\alpha\nabla v_1 + (1-\alpha)\nabla v_2)\|^2\right] dxdy \\ \leq &\frac{K}{2}\left(\alpha\int_\Omega \left[\|\nabla u_1\|^2 + \|\nabla v_1\|^2\right] dxdy + (1-\alpha)\int_\Omega \left[\|\nabla u_2\|^2 + \|\nabla v_2\|^2\right] dxdy\right) \end{aligned} \tag{6.3}$$

and

$$\begin{aligned} \int_\Omega [(\alpha U_1 + (1-\alpha)U_2)\cdot\nabla E]^2 dxdy \leq \alpha\int_\Omega (U_1\cdot\nabla E)^2 dxdy \\ +(1-\alpha)\int_\Omega (U_2\cdot\nabla E)^2 dxdy. \end{aligned} \tag{6.4}$$

Equality holds in (6.3) iff

$$\nabla u_1 = \nabla u_2,\ \nabla v_1 = \nabla v_2 \tag{6.5}$$

and in (6.4) iff

$$U_1\cdot\nabla E = U_2\cdot\nabla E. \tag{6.6}$$

From (6.5) we have

$$u_1 - u_2 = c_1, \qquad v_1 - v_2 = c_2 \tag{6.7}$$

where c_1 and c_2 are constants. From (6.6) we get

$$E_x(u_1 - u_2) + E_y(v_1 - v_2) = 0. \tag{6.8}$$

But as E_x and E_y are linearly independent, (6.7) and (6.8) gives

$$u_1 = u_2, \qquad v_1 = v_2$$

which implies

$$U_1 = U_2.$$

Hence for $U_1 \neq U_2$ we have,

$$\int_\Omega ((\alpha U_1 + (1-\alpha)U_2)\cdot\nabla E)^2 dxdy < \alpha\int_\Omega (U_1\cdot\nabla E)^2 dxdy + (1-\alpha)\int_\Omega (U_2\cdot\nabla E)^2 dxdy.$$

This gives

$$J(\alpha U_1 + (1-\alpha)U_2) < \alpha J(U_1) + (1-\alpha)J(U_2), \qquad 0 < \alpha < 1. \tag{6.9}$$

This implies that J is a strictly convex functional w.r.t U. □

Theorem 6.3.6. *The constraint set (6.2) given as $C = \{U \in Z : \nabla\cdot U = 0\}$ is a closed subspace of Z.*

Proof. For $U_1, U_2 \in C$ we have

$$\nabla \cdot (\alpha U_1 + \beta U_2) = \alpha(\nabla \cdot U_1) + \beta(\nabla \cdot U_2) \qquad \forall \alpha, \beta \in \mathbb{R}.$$

Hence

$$\alpha U_1 + \beta U_2 \in C, \qquad \alpha, \beta \in \mathbb{R}.$$

Now consider a sequence $\{U_n\}_n \in C$ such that it converges to U in $\|.\|_Z$. We need to show that $U \in C$. Since $U_n \to U$ in C, we have $U_n \to U$ in Z and $\nabla \cdot U_n = 0$. Now $U_n \to U$ in Z gives $U_n \to U$ in H_1 and $\nabla U_n \to \nabla U$ in H_1. This implies $\nabla \cdot U_n \to \nabla \cdot U$ in H_1 which in turn implies $\nabla \cdot (U_n - U) \to 0$ in H_1. Finally writing $\nabla \cdot U = \nabla \cdot (U - U_n) + \nabla \cdot U_n$ we see that $\nabla \cdot U \to 0$ as $n \to \infty$. This shows that $U \in C$ and so C is a closed subspace of Z and hence convex. □

Thus J is a strict convex function defined on H and the constraint set (6.2) denoted as K is a closed subspace of Z. We now show that J is continuous and coercive.

Theorem 6.3.7. *The functional J as given in (6.1) is continuous*

Proof. We will use the Theorem 6.3.3 to prove our statement. We assume

$$\|E\|_{W^{1,\infty}(\Omega)} \leq M.$$

As $0 \in Z$, we consider a neighborhood of zero given as $N_1 = \{U : \|U\|_Z < 1\}$. Now

$$\begin{aligned}
|J(U)| &= \left| \frac{1}{2} \int_\Omega (U \cdot \nabla E + E_t)^2 \, dxdy + \frac{K}{2} \int_\Omega \left[\|\nabla u\|^2 + \|\nabla v\|^2 \right] dxdy \right| \\
&\leq \frac{1}{2} \int_\Omega (U \cdot \nabla E + E_t)^2 \, dxdy + \frac{K}{2} \|U\|_Z^2 \\
&\leq \frac{1}{2} \int_\Omega \left(E_t^2 + (U \cdot \nabla E)^2 + 2E_t(U \cdot \nabla E) \right) dxdy + \frac{K}{2} \|U\|_Z^2
\end{aligned}$$

Using Hölder's inequality and L^∞ bound on E and its derivatives we get

$$\begin{aligned}
|J(U)| &\leq \frac{1}{2} \int_\Omega \left[M^2 + M^2(u+v)^2 \right] dxdy \\
&\quad + 2M \left(\int_\Omega (\nabla E)^2 \right)^{1/2} \left(\int_\Omega U^2 \right)^{1/2} dxdy + \frac{K}{2} \|U\|_Z^2 \\
&\leq \frac{M^2}{2} \int_\Omega \left[1 + 2(u^2 + v^2) \right] dxdy + M(\int_\Omega M^2)^{1/2} \|U\|_Z + \frac{K}{2} \|U\|_Z^2 \\
&\leq \frac{M^2}{2} (\int_\Omega 1) + M^2 \|U\|_Z^2 + M^2 (\int_\Omega 1) + \frac{K}{2} \|U\|_Z^2 \\
&< \frac{3M}{2} \mu(\Omega) + M^2 + \frac{K}{2} \qquad (\text{ as } \|U\|_Z < 1) \\
&< \infty.
\end{aligned}$$

where $\mu(\Omega)$ is the measure of Ω. This gives us $J(U)$ is bounded above in N_1. As J is convex (by Theorem 6.3.5), it implies J is continuous for all $U \in Z$ (by Theorem 6.3.3). □

Theorem 6.3.8. *The functional J as given in (6.1) is coercive under the assumption that E_x and E_y are linearly independent.*

Proof. The functional J in (6.1) can be written as

$$J(U) = J_1(U) + \int_\Omega \{E_t^2 + 2E_t(U \cdot \nabla E)\} dxdy$$

where

$$J_1(U) = \int_\Omega (U \cdot \nabla E)^2 dxdy + \frac{K}{2} \int_\Omega \|\nabla U\|^2 dxdy. \tag{6.10}$$

To show $J(U)$ is coercive we need to show $J_1(U)$ is coercive as it is quadratic in U. We use the Poincare-Wirtinger's Inequality

$$\int_\Omega (U - T)^2 dxdy \leq D \int_\Omega \|\nabla U\|^2 dxdy \tag{6.11}$$

where

$$T = \frac{1}{\mu(\Omega)} \int_\Omega U dxdy \tag{6.12}$$

and D is a constant depending on Ω. Suppose J_1 is not coercive. Then there does not exist any constant $M > 0$ such that

$$J_1(U) \geq M\|U\|_Z^2 \qquad \forall U \in Z$$

because if it was so then $J_1 \to \infty$ as $\|U\|_Z \to \infty$. So for any $M > 0$ there exists $U_M \in Z$ such that

$$J_1(U_M) < M\|U_M\|_Z^2.$$

We choose $M = \frac{1}{n}$ and get a sequence of M_n's and correspondingly get U_n. Without loss of generality, let us assume $\|U_n\|_Z = 1$. If not, we can take $V_n = \frac{U_n}{\|U_n\|_Z}$ and replace U_n with V_n. So we get a sequence $\{U_n\}_{n\in\mathbb{N}}$ in Z with $\|U_n\|_Z = 1$ and $J_1(U_n) \to 0$ as $n \to \infty$. Using (6.10) and (6.11) we have

$$\int_\Omega (u_n - T_n^1)^2 dxdy \to 0 \tag{6.13}$$

and

$$\int_\Omega (v_n - T_n^2)^2 dxdy \to 0 \qquad \text{for } n \to \infty. \tag{6.14}$$

where

$$T_n^1 = \frac{1}{\mu(\Omega)} \int_\Omega u_n dxdy, \qquad T_n^2 = \frac{1}{\mu(\Omega)} \int_\Omega v_n dxdy.$$

As

$$\int_\Omega (E_x u + E_y v)^2 dxdy \leq 2|E_x^2|_\infty \int_\Omega u^2 dxdy + 2|E_y^2|_\infty \int_\Omega v^2 dxdy$$

we have

$$\int_\Omega \left(E_x(u_n - T_n^1) + E_y(v_n - T_n^2)\right)^2 dxdy \to 0 \qquad \text{as } n \to \infty. \tag{6.15}$$

Now

$$\begin{aligned}
\left(\int_\Omega (E_x T_n^1 + E_y T_n^2)^2 dxdy\right)^{1/2} &= \left(\int_\Omega (E_x u_n + E_y v_n + E_x(T_n^1 - u_n) + E_y(T_n^2 - v_n))^2 dxdy\right)^{1/2} \\
&\leq \left(\int_\Omega (E_x u_n + E_y v_n)^2 dxdy\right)^{1/2} \\
&+ \left(\int_\Omega (E_x(T_n^1 - u_n) + E_y(T_n^2 - v_n))^2 dxdy\right)^{1/2} \\
&\leq (J_1(U_n))^{1/2} + \left(\int_\Omega (E_x(T_n^1 - u_n) + E_y(T_n^2 - v_n))^2 dxdy\right)^{1/2} \\
&\to 0 \text{ for } n \to \infty. \qquad \text{(Using (6.15))}
\end{aligned}$$

Let $a = E_x T_n^1, \quad b = E_y T_n^2$. Then

$$\begin{aligned}
\|a+b\|_H^2 &= \|a\|_H^2 + \|b\|_H^2 + 2(a,b)_H \\
&\geq \|a\|_H^2 + \|b\|_H^2 - 2\|a\|_H\|b\|_H \frac{|(a,b)|_H}{\|a\|_H\|b\|_H} \\
&\geq \|a\|_H^2 + \|b\|_H^2 - (\|a\|_H^2 + \|b\|_H^2)\frac{|(a,b)|_H}{\|a\|_H\|b\|_H} \\
&= (\|a\|_H^2 + \|b\|_H^2)\{1 - \frac{|(a,b)|_H}{\|a\|_H\|b\|_H}\}
\end{aligned}$$

where $(a,b)_H$ is the usual inner product in H. So we get

$$\int_\Omega (E_x T_n^1 + E_y T_n^2)^2 dxdy \geq \left(\|E_x\|_H^2 (T_n^1)^2 + \|E_y\|_H^2 (T_n^2)^2\right)\{1 - \frac{|(E_x,E_y)|_H}{\|E_x\|_H\|E_y\|_H}\}. \tag{6.16}$$

As left hand side of (6.16) $\to 0$ as $n \to \infty$ and by linear independency of E_x and E_y

$$1 - \frac{|(E_x,E_y)|_H}{\|E_x\|_H\|E_y\|_H} > 0$$

and since $\|E_x\|_H$ and $\|E_y\|_H$ are not identically 0, we have

$$T_n^1 \to 0 \text{ and } T_n^2 \to 0 \text{ as } n \to \infty \tag{6.17}$$

But this gives a contradiction as $\|U_n\|_Z \leq \|(U_n - T_n)\|_Z + \|T_n\|_Z$ and hence $\|U_n\|_Z \to 0$ as $n \to \infty$ (using (6.13),(6.14),(6.17)). So J_1 is coercive and hence J is coercive. □

By Theorem 6.3.4, the problem (P) has a unique global minimum.

6.4 Exact recovery of Stokes flow

We now write down the optimality conditions for the minimizer of (P). Using Lagrange multipliers, the auxiliary functional can be written as

$$\widetilde{J}(U,p) = \frac{1}{2}\int_\Omega (E_t + U\cdot\nabla E)^2 \, dxdy + \frac{K}{2}\int_\Omega \|\nabla U\|^2 \, dxdy + \int_\Omega (\nabla\cdot U)p \, dxdy$$

Taking Gateaux derivative of $\widetilde{J}$ wrt U and p, the standard optimality conditions [100] are

$$\frac{\partial \widetilde{J}}{\partial U} = 0 \quad \text{and} \quad \frac{\partial \widetilde{J}}{\partial p} = 0. \tag{6.18}$$

The first equation in (6.18) gives

$$\int_\Omega (E_t + (U\cdot\nabla E))(\overline{U}\cdot\nabla E) + K\int_\Omega (\nabla u\cdot\nabla\overline{u}) + (\nabla v\cdot\nabla\overline{v}) + \int_\Omega (\nabla\cdot\overline{U})p = 0, \quad \forall\, \overline{U} \in Z \tag{6.19}$$

with prescribed Dirichlet boundary conditions

$$U = U_b \qquad \text{on } \partial\Omega. \tag{6.20}$$

The second equation in (6.18) gives

$$\int_\Omega (\nabla\cdot U)\overline{p} = 0 \qquad \forall \overline{p} \in L^2(\Omega) \tag{6.21}$$

Performing an integration by parts on the second term on the left in (6.19) and taking $\overline{U}$ to be an arbitrary function in Z, together with (6.21) the following PDE is obtained

$$\begin{aligned} K\Delta U - \nabla p &= -(E_t + U \cdot \nabla E)\nabla E \\ \nabla \cdot U &= 0 \end{aligned} \tag{6.22}$$

subject to (6.20).

Theorem 6.4.1. *Let E in the right hand side of (6.22) be advected with velocity U_e i.e.*

$$E_t + U_e \cdot \nabla E = 0$$

with U_e satisfying (6.20) and incompressible Stokes equation

$$\begin{aligned} &\alpha\Delta U_e + \nabla q = f, \qquad \alpha > 0 \\ &\nabla \cdot U_e = 0. \end{aligned} \tag{6.23}$$

If f is given by a potential $f = \nabla\phi$ for smooth ϕ, then $U = U_e$ is the only solution of (6.22) which is independent of any $K > 0$. In other words the flow is recovered exactly irrespective of K.

Proof. Eq. (6.22) can rewritten as

$$\alpha\Delta U - \frac{\alpha}{K}\nabla p = -\frac{\alpha}{K}(E_t + U \cdot \nabla E)\nabla E \tag{6.24}$$

Since $f = \nabla\phi$, Eq. (6.23) can be rewritten as

$$\alpha\Delta U_e + \nabla(q + \phi) = 0$$

As the image E is advected with velocity, U_e is a solution of Eq. (6.24) with $p = -\frac{K}{\alpha}(q + \phi)$ and right hand side as zero. As the solution of (6.22) is unique, $U = U_e$ is the unique solution of (6.22) which is independent of any $K > 0$. □

The result of Theorem 6.4.1 is verified in the numerical examples in Section 6.6 where we have considered incompressible Stokes flow under various boundary conditions and find that the flow is recovered with a high precision. Also as Navier-Stokes flow at low Reynolds number represents Stokes flow, we recover low Reynolds number Navier-Stokes flow accurately.

6.5 Finite element method for the Optical flow problem (6.1)

Eq. (6.22) is solved using the finite element method. Combining equations (6.19) and (6.21) along with the boundary conditions (6.20) gives the weak formulation of the PDE to be solved to determine the minimizer. Let T_h be a triangulation of domain Ω and let K be a triangle in T_h. Let Z_h and X_h be two finite element spaces with triangulation parameter h such that

$$Z_h \subset Z, \qquad X_h \subset L^2(\Omega)$$

Then the discrete problem is to find $(U_h, p_h) \in (Z_h \cap Z_b) \times X_h$ such that

$$\begin{aligned} \int_\Omega (E_t + (U_h \cdot \nabla E))(\nabla E \cdot \overline{U}_h) + K\int_\Omega (\nabla u_h \cdot \nabla \overline{u}_h) + (\nabla v_h \cdot \nabla \overline{v}_h) + \int_\Omega (\nabla \cdot \overline{U}_h) p_h = 0 \\ \int_\Omega (\nabla \cdot U_h)\overline{p}_h = 0 \end{aligned} \tag{6.25}$$

where $(\overline{U}_h, \overline{p}_h) \in Z_h \times X_h$.
Let us define the following Taylor-Hood finite element spaces

$$Z_h(\Omega) = \{U_h \in (C^0(\Omega))^2 : U_h|_K \text{ is a polynomial of degree 2 and } U_h = 0 \text{ on } \partial\Omega\} \tag{6.26}$$

and

$$X_h(\Omega) = \{p_h \in C^0(\Omega) : p_h|_K \text{ is a polynomial of degree 1}\} \tag{6.27}$$

which satisfy the LBB condition [38]. We now describe the procedure to determine E, E_t and ∇E.

6.5.1 Image data

Our aim is to generate a sequence of synthetic images E and try to recover the velocity given the information of the derivatives of E. For this purpose E is chosen whose analytic expression is known at time $t = 0$ and hence its gradients can be computed exactly. To advect E with velocity U_e exactly, E_t at $t = 0$ is generated from the equation

$$E_t(x, y, 0) = -U_e \cdot \nabla E(x, y, 0)$$

where U_e represents the velocity obtained by solving incompressible Stokes flow

$$\begin{aligned} \Delta U + \nabla p &= f \\ \nabla \cdot U &= 0 \end{aligned} \tag{6.28}$$

or Navier-Stokes flow

$$\begin{aligned} -\alpha \Delta U + (U \cdot \nabla)U + \nabla p &= f, \\ \nabla \cdot U &= 0 \end{aligned} \tag{6.29}$$

using finite element method with appropriate boundary conditions, where $\alpha = 1/Re$ and Re is the Reynolds number. In practice, derivatives of images will be computed using some finite differences which will introduce errors in the computed velocity.

6.5.2 Test Flows

Two types of flows are considered: one in a lid-driven cavity and the other past a cylinder. For flows in a lid-driven cavity, the domain is $\Omega = [0, 1] \times [0, 1]$. The boundary conditions are

$$U = \begin{cases} (1, 0) & \text{on } y = 1 \\ (0, 0) & \text{elsewhere} \end{cases} \tag{6.30}$$

with image at time t_0 defined as

$$E_0(x, y) = E(x, y, 0) = e^{-50[(x-1/2)^2 + (y-1/2)^2]}$$

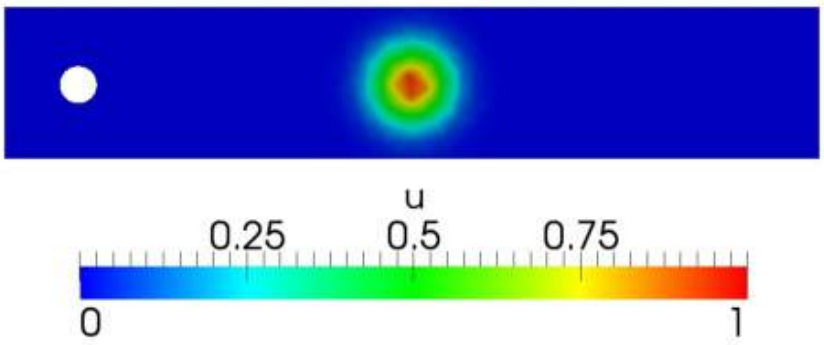

Figure 6.2: Image at time $t = 0$

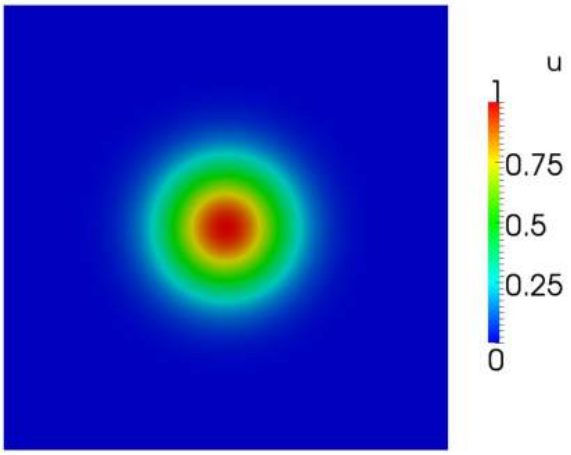

Figure 6.1: Image at time $t = 0$

For flows past a cylinder, the domain Ω is a rectangle in $\mathbb{R}^2$ given as $[0, 2.2] \times [0, 0.41]$ with a closed disk inside it centered at $(0.2, 0.2)$ and radius 0.05. The boundary conditions are

$$U = \begin{cases} (0,0) & \text{on } y = 0, y = 0.41 \text{ and on the surface of the disk} \\ (0, \frac{6y(0.41-y)}{0.41^2}) & \text{on } x = 0 \end{cases} \tag{6.31}$$

with image at time t_0 defined as

$$E_0(x, y) = E(x, y, 0) = e^{-50[(x-1.1)^2+(y-0.2)^2]}$$

To compute U_e, Eq. (6.28) or (6.29) is solved subject to the boundary conditions given in (6.30) or (6.31). But exact analytic expressions of solutions to (6.28) or (6.29) with the specified boundary conditions are usually not known. So finite element method is used to obtain U_e.

6.5.3 Mesh

For flows in a lid-driven cavity, the domain $\Omega = [0, 1] \times [0, 1]$ is triangulated with 100 points on each side as shown in Figure 6.3. There are 20000 triangles with 10201 degrees of freedom. For flows past a cylinder, the mesh used is shown in Figure 6.4. It comprises of 200 points on the longer boundary, 80 points on the shorter boundary and 100 points on the circular boundary. There are 28582 triangles with 14605 degrees of freedom.

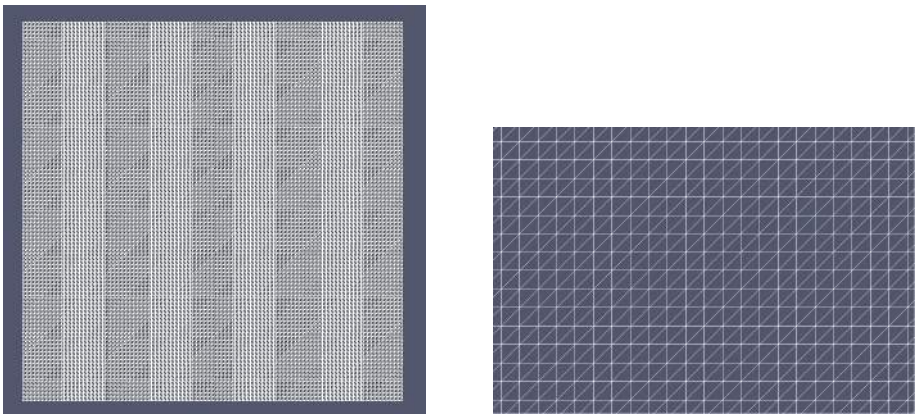

(a) Full Mesh (b) Zoomed View

Figure 6.3: Mesh for the lid-driven cavity flows. Figure 6.4a shows the full domain with the mesh. Figure 6.4b shows a zoomed view of the triangulation

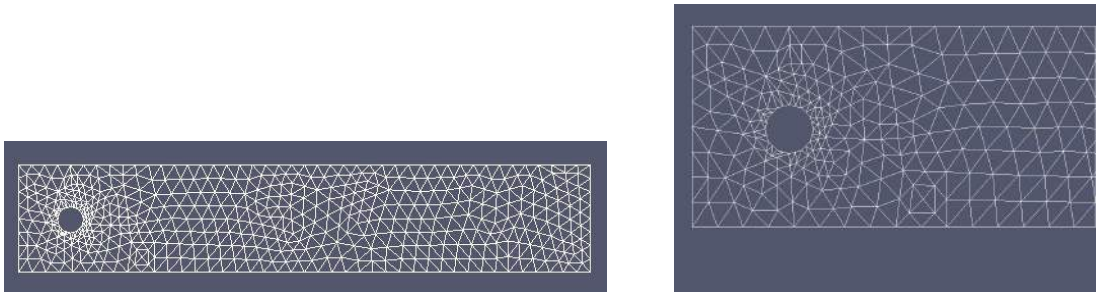

(a) Full Mesh (b) Zoomed View

Figure 6.4: Mesh for the lid-driven cavity flows. Figure 6.4a shows the full domain with the mesh. Figure 6.4b shows a zoomed view of the triangulation near the inner circular boundary

6.5.4 Solving the Stokes equation

To solve (6.28), let us write the weak formulation as: find $U \in Z_b = \{U \in Z : U = U_b \text{ on } \partial\Omega\}$ and $p \in L^2(\Omega)$ such that

$$\int_\Omega \nabla U \cdot \nabla V + \int_\Omega (\nabla \cdot V)p + \int_\Omega (\nabla \cdot U)q + \int_\Omega f \cdot V = 0 \qquad \forall (V, q) \in Z \times L^2(\Omega) \tag{6.32}$$

We also fix the value of p to be zero at a point $X_0 \in \partial\Omega$ to obtain uniqueness. The discrete problem is to find $(U_h, p_h) \in (Z_h \cap Z_b) \times X_h$ such that

$$\int_\Omega \nabla U_h \cdot \nabla V_h - \int_\Omega (\nabla \cdot V_h)p_h - \int_\Omega (\nabla \cdot U_h)q_h = \int_\Omega f \cdot V_h \qquad \forall (V_h, q_h) \in Z_h \times X_h \tag{6.33}$$

where Z_h and X_h are defined in (6.26) and (6.27) respectively. Solving Eq. 6.33 with domains, boundary conditions and meshes defined in Sections 6.5.2 and 6.5.3 gives U_e.

6.5.5 Solving the Navier-Stokes equation

Equation (6.29) is a non-linear equation in U. So the method of Picard iteration, which is an easy way of handling nonlinear PDEs, is used. In this method, a previous solution in the nonlinear terms is used so that these terms become linear in the unknown U. The strategy is also known as the method of successive substitutions [52]. In our case, we seek a new solution U^{k+1} in iteration $k+1$ such that (U^{k+1}, p^{k+1}) solves the linear problem

$$\begin{aligned} -\alpha \Delta U^{k+1} + (U^k \cdot \nabla)U^{k+1} + \nabla p^{k+1} &= f, \\ \nabla \cdot U^{k+1} &= 0 \end{aligned} \tag{6.34}$$

with given boundary conditions, where U^k is known. The variational formulation for (6.34) can be written as: find $U^{k+1} \in Z_b = \{U \in Z : U = U_b \text{ on } \partial\Omega\}$ and $p^{k+1} \in L^2(\Omega)$ such that

$$\begin{aligned} \int_\Omega \alpha \nabla U^{k+1} \cdot \nabla V + \int_\Omega \left[(U^k \cdot \nabla)U^{k+1}\right] \cdot V - \int_\Omega (\nabla \cdot V)p^{k+1} - \int_\Omega (\nabla \cdot U^{k+1})q \\ - \int_\Omega f \cdot V = 0 \quad \forall (V, q) \in Z \times L^2(\Omega) \end{aligned} \tag{6.35}$$

We start with initial guess $U^0 = (0, 0)$ and employ the finite element method as described in Section (6.5.4) to determine U^{k+1}. Finally, we stop at the $k + 1^{th}$ stage if $\|U^{k+1} - U^k\| < \epsilon$. We choose $\epsilon = 10^{-7}$. Hence we have $U_e = U^{k+1}$.
Finally, the relative L^2 error in velocity is defined as

$$\text{Relative } L^2 \text{ error} = \frac{\|U_e - U_o\|}{\|U_e\|} \tag{6.36}$$

and the advection error is defined as

$$\text{Advection Error} = \|E_t + U_o \cdot \nabla E\| \tag{6.37}$$

where U_e is the exact velocity and U_o is the obtained velocity and the norm $\|\cdot\|$ is the usual L^2 norm for vector functions as defined earlier.

6.6 Numerical Examples

6.6.1 Stokes Flow in a lid driven cavity

The exact flow is given by solving (6.28) with $f = (1, 100)$ in lid-driven cavity. Figure (6.5) shows plots of velocity vectors for various K. The velocity is recovered with a very high degree

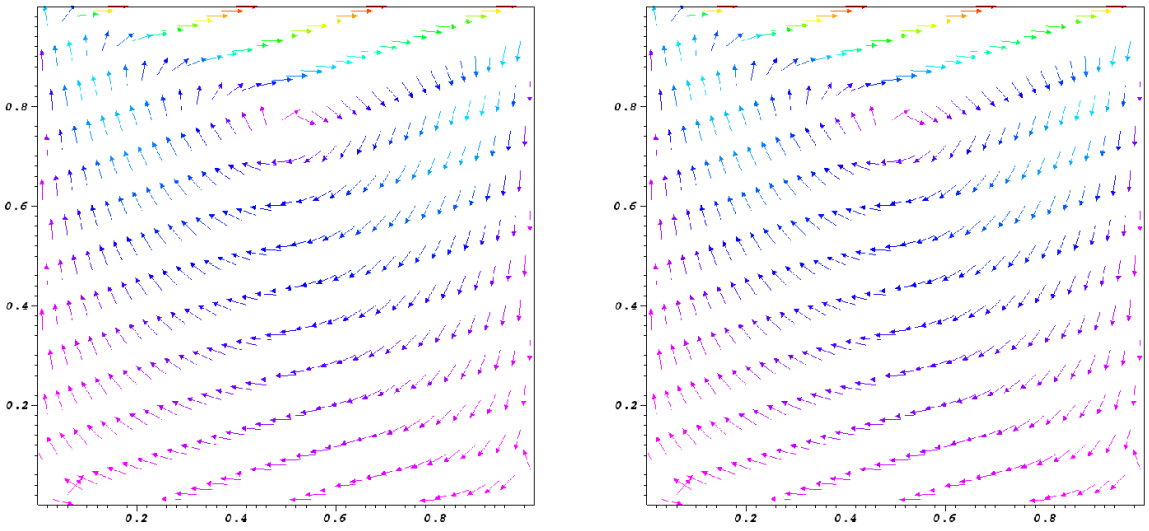

(a) Exact (b) K=0.001

(c) K=5 (d) K=35

Figure 6.5: Velocity plots for Stokes flow in a lid driven cavity

of accuracy. This is also reflected in the relative L^2 errors given in Table (6.1). Also Table (6.1) shows that the advection errors are very small and so the recovered velocity preserves the advection properties of the image. The streamline plots for the velocity given in Figures (6.6) shows that large vortex in the center and the two small vortices at the bottom corners are detected with good accuracy which is actually very important in atmospheric flows. It is notable that the regularization parameter K has minimal effect on the behavior of the solutions which is consistent with the fact that it is not a physical parameter and hence any positive value of K can be used to determine the velocity. This perfectly justifies the result proved in Theorem 6.4.1.

6.6.2 Stokes flow past a cylinder

The exact flow is given by solving (6.28) as a flow past a cylinder with $f = (1, 100)$. Figure (6.7) shows plots of velocity vectors for various K. Again the velocity is recovered with a very high degree of accuracy. Table (6.2) shows the relative L^2 errors and the advection errors, which are quite small, justifying good recovery of flows. The streamline plots for the velocity is given in

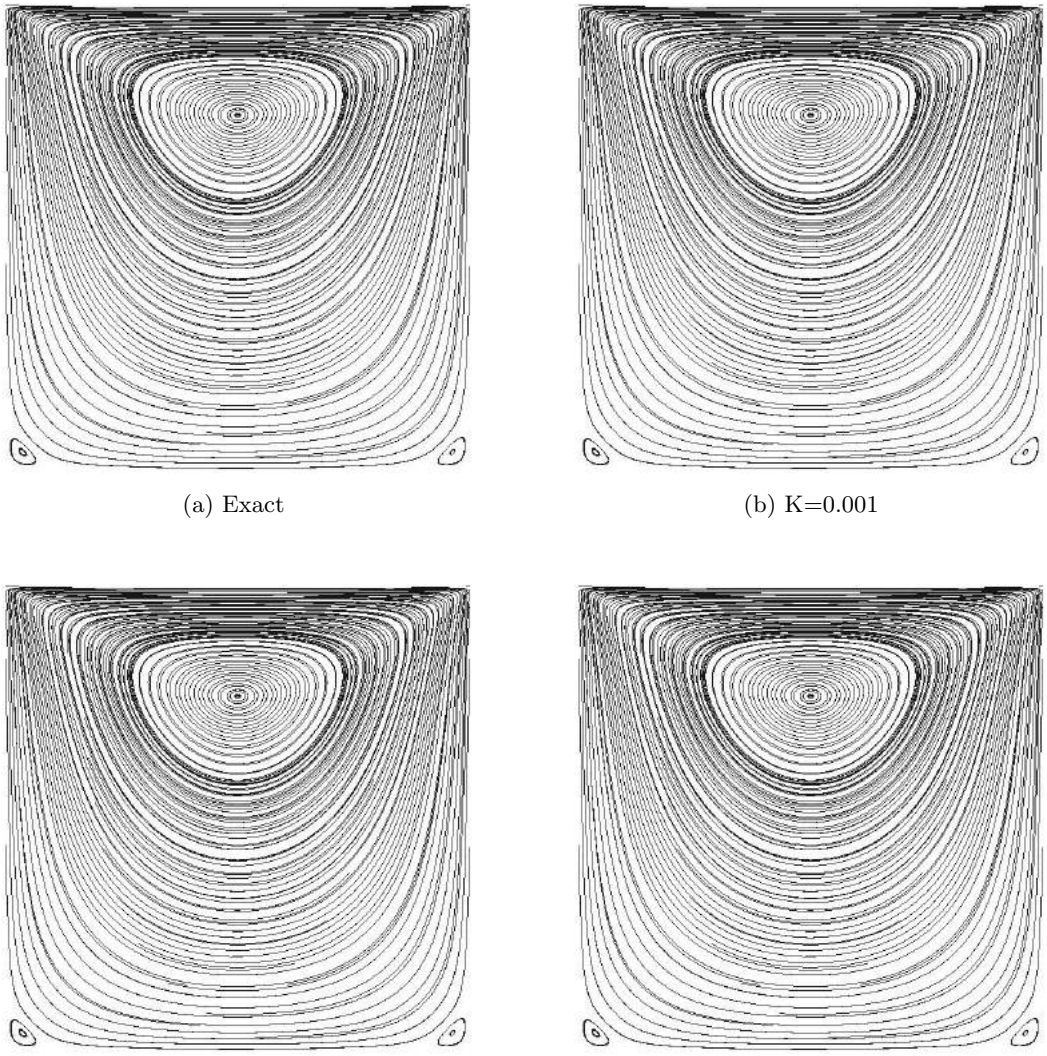

(a) Exact

(b) K=0.001

(c) K=5

(d) K=35

Figure 6.6: Streamline plots for Stokes flow in a lid driven cavity

K	Relative L^2 Error	Advection Error
0.001	4.55e-08	9.62e-26
5	4.56e-08	6.83e-27
110	4.49e-08	2.51e-27
300	4.48e-08	4.11e-27
600	4.42e-08	3.57e-28

Table 6.1: Variation of relative L^2 error and advection error with K for Stokes flow in a lid driven cavity

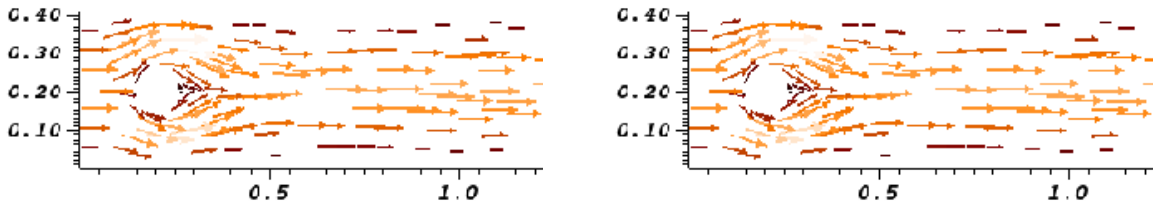

(a) Exact (b) K=0.001

(c) K=5 (d) K=35

Figure 6.7: Velocity plots for Stokes flow past a cylinder

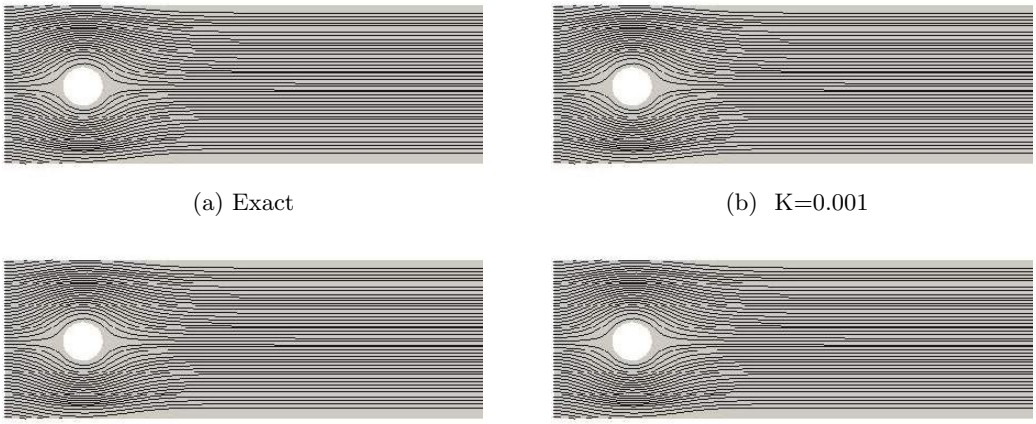

(a) Exact (b) K=0.001

(c) K=5 (d) K=35

Figure 6.8: Streamline plots for Stokes flow past a cylinder

Figure (6.8). As with the case of Stokes flow in a lid driven cavity, there is no dependence of the obtained solutions on K.

6.6.3 Navier-Stokes flow in a lid driven cavity for $Re = 1$ and 1000

Here we consider motion governed by Navier-Stokes flows for $Re = 1$ and 1000. The exact flow is given by solving (6.29) with $f = (1, 100)$ in a lid-driven cavity. Figures (6.9) and (6.11) show the velocity vector plots for $Re = 1$ and $Re = 1000$ respectively. The plots show good recovery for $Re = 1$, whereas for $Re = 1000$ the relative L^2 error is on the higher side. This is also reflected in Tables (6.3) and (6.4). The streamline plots given by Figures (6.10), (6.12) show that for lower Reynolds number flows the vortices are well recovered whereas for higher Reynolds number flows the vortices are recovered though not to a greater degree of accuracy. Tables (6.3) and (6.4) suggests that the advection error for lower Reynolds number flows is very low compared to higher Reynolds number flows. This is because at low Reynolds number, Navier-Stokes flows represents Stokes flows and hence they are recovered well. For higher Reynolds number flows, the non-linear convection term dominates and so a very good flow recovery is not possible with our linear model. However we note that even for higher Reynolds number flows, the solution

K	Relative L^2 Error	Advection Error
0.001	1.44e-8	3.76e-28
5	1.53e-8	6.43e-27
110	1.47e-8	6.69e-28
300	1.42e-8	5.25e-28
600	1.69e-8	5.32e-28

Table 6.2: Variation of relative L^2 error and advection error with K for Stokes flow past a cylinder

K	Relative L^2 Error	Advection Error
0.001	3.56e-4	2.7e-11
5	3.61e-4	2.8e-11
110	3.44e-4	3.1e-11
300	3.48e-4	2.9e-11
600	3.4e-4	2.6e-11

Table 6.3: Variation of relative L^2 error and advection error with K for Navier-Stokes flow in a lid driven cavity for $Re = 1$

obtained is independent of K.

6.6.4 Navier-Stokes flow past a cylinder.

The exact flow is given by solving (6.29) as a flow past a cylinder with $f = (1, 100)$. Figures (6.13) and (6.15) show the velocity vector plots for $Re = 1$ and $Re = 1000$ respectively. The plots show good recovery for $Re = 1$, whereas for $Re = 1000$ the relative L^2 error is on the higher side which is also reflected in Tables (6.5) and (6.6). The streamline plots given by Figures (6.14) and (6.16) show that vortices for low Reynolds number flows are captured well whereas for higher Reynolds number flows, the vortices behind the cylinder are not captured. This suggests there is a need to include extra assumptions in our model for high Reynolds number flows.

6.7 Conclusion

A variational technique for tracking instantaneous motion from flow images using the well-known OFM has been formulated. In the present work, these flow images have been generated by numerically solving the 2D incompressible Stokes equation (6.28) or the Navier-Stokes equations (6.29) for $Re = 1$ and 1000. Incompressibility is the only constraint imposed in the variational

K	Relative L^2 Error	Advection Error
0.001	5.81e-1	2.8e-8
5	5.95e-1	3.6e-8
110	6.12e-1	4.1e-8
300	6.07e-1	2.5e-8
600	5.86e-1	5.2e-8

Table 6.4: Variation of relative L^2 error and advection error with K for Navier-Stokes flow in a lid driven cavity for $Re = 1000$

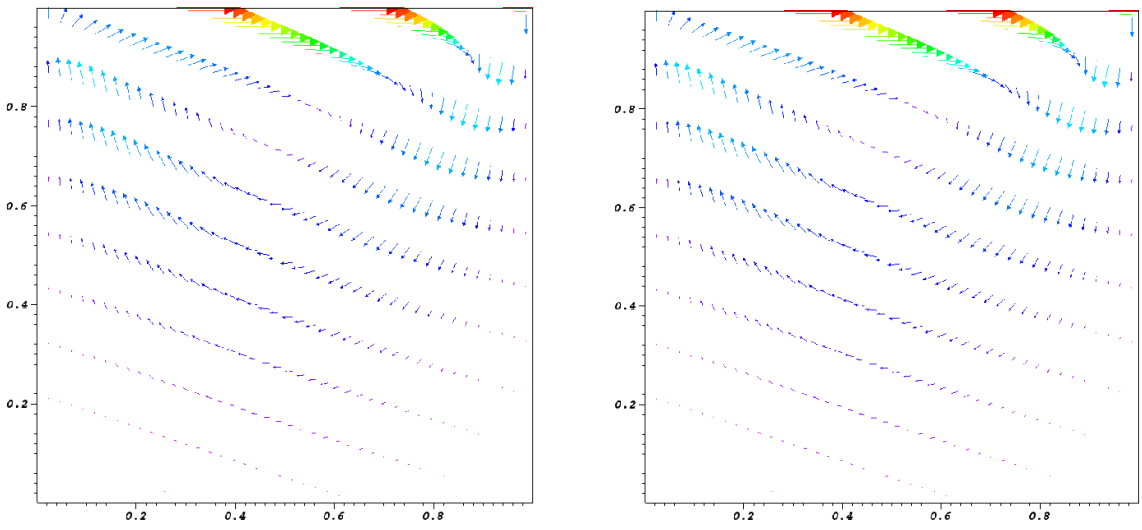

(a) Exact (b) K=0.001

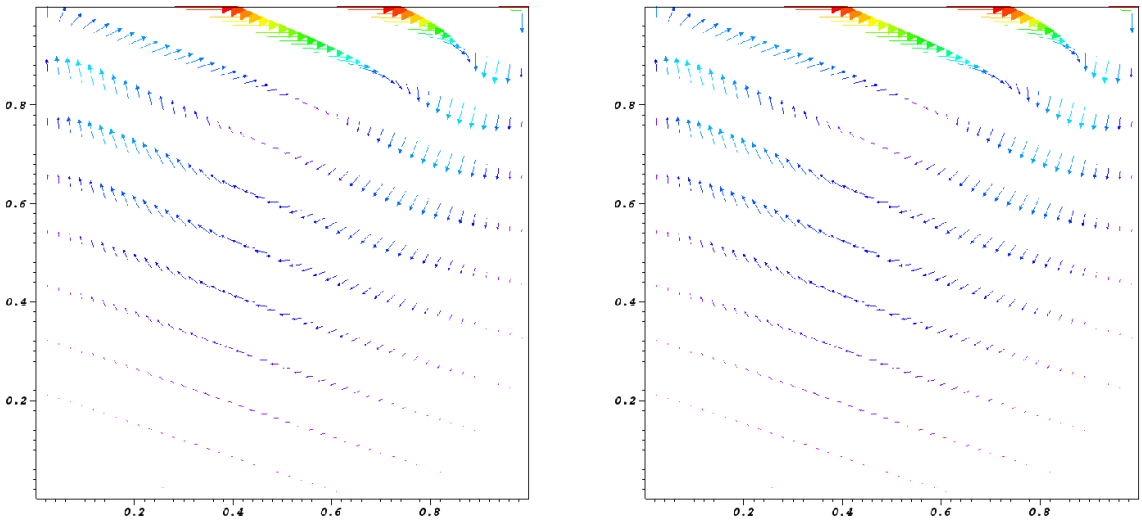

(c) K=5 (d) K=35

Figure 6.9: Velocity plots for Navier-Stokes flow in a lid driven cavity for $Re = 1$

K	Relative L^2 Error	Advection Error
0.001	1.01e-4	2.0e-11
5	1.11e-4	2.0e-11
110	1.24e-4	2.1e-11
300	1.15e-4	2.5e-11
600	1.08e-4	2.6e-11

Table 6.5: Variation of relative L^2 error and advection error with K for Navier-Stokes flow past a cylinder for $Re = 1$

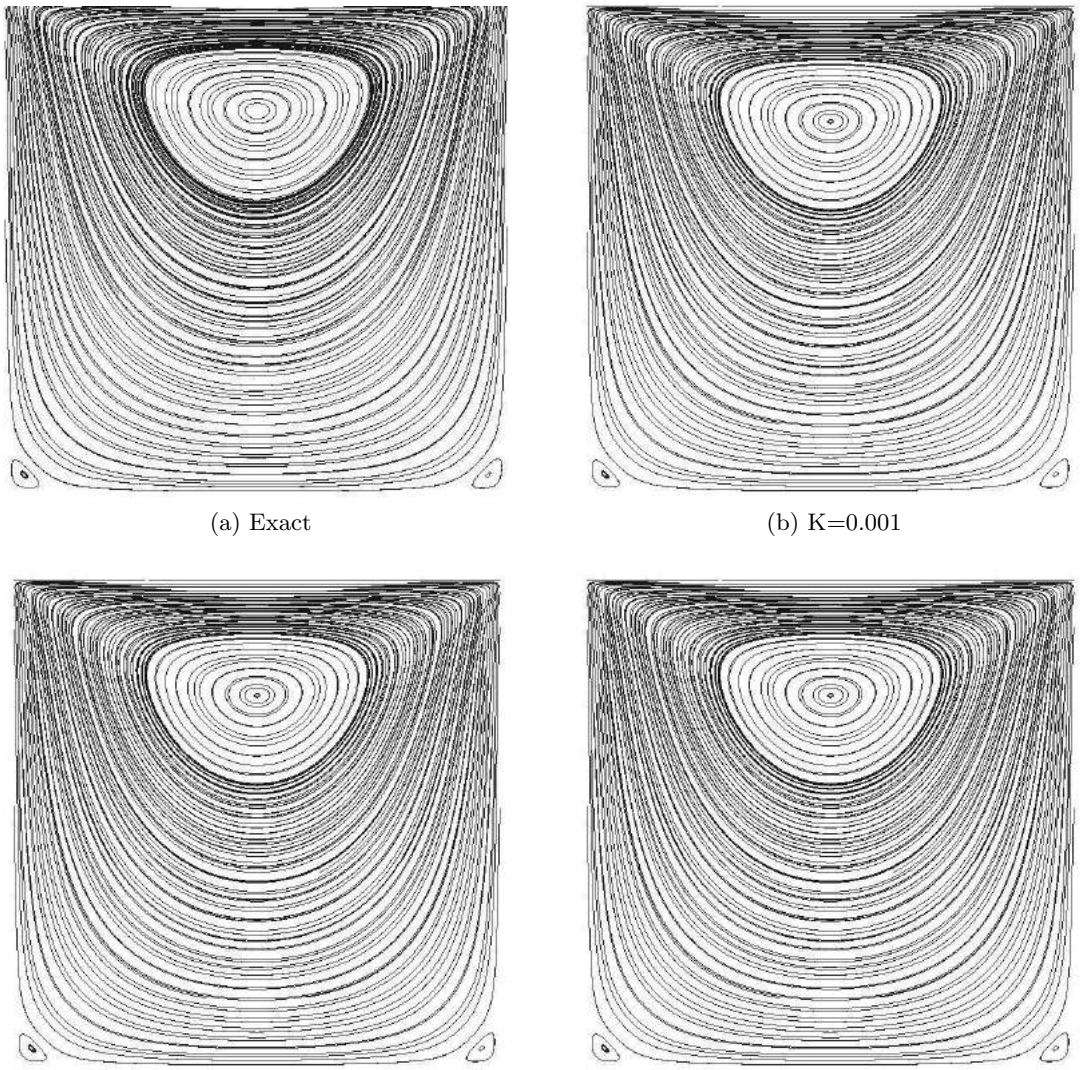

(a) Exact (b) K=0.001

(c) K=5 (d) K=35

Figure 6.10: Streamline plots for Navier-Stokes flow in a lid driven cavity for $Re = 1$

K	Relative L^2 Error	Advection Error
0.001	7.23e-1	4.3e-8
5	6.56e-1	4.6e-8
110	6.12e-1	4.6e-8
300	6.33e-1	4.5e-8
600	6.86e-1	4.7e-8

Table 6.6: Variation of relative L^2 error and advection error with K for Navier-Stokes flow past a cylinder for $Re = 1000$

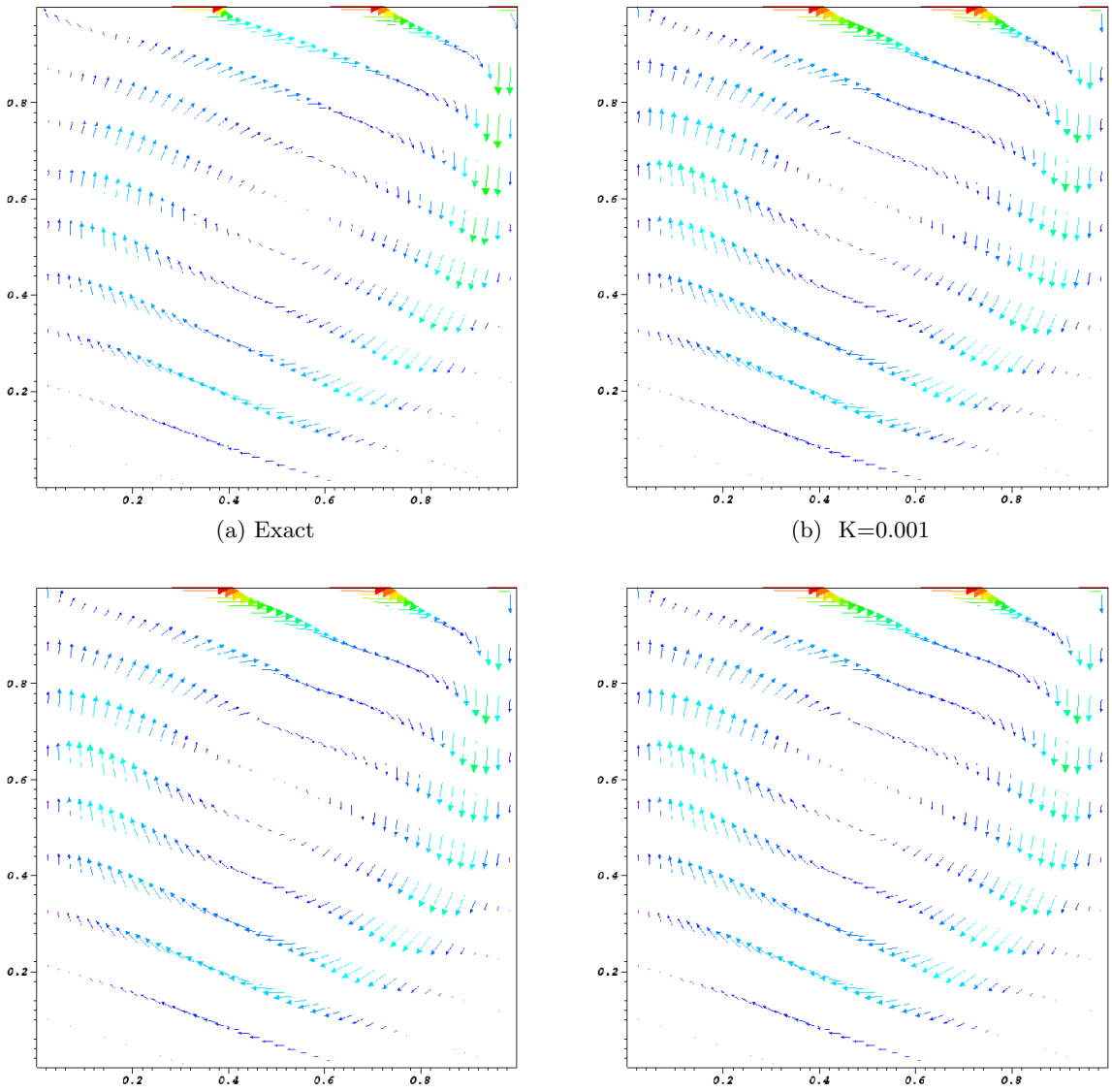

(a) Exact (b) K=0.001

(c) K=5 (d) K=35

Figure 6.11: Velocity plots for Navier-Stokes flow in a lid driven cavity for $Re = 1000$

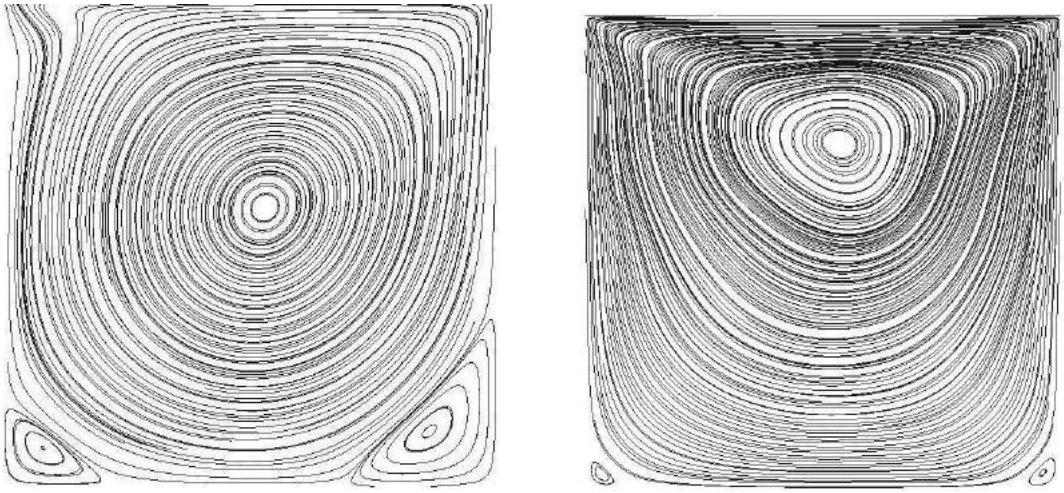

(a) Exact (b) K=0.001

(c) K=5 (d) K=35

Figure 6.12: Streamline plots for Navier-Stokes flow in a lid driven cavity for $Re = 1000$

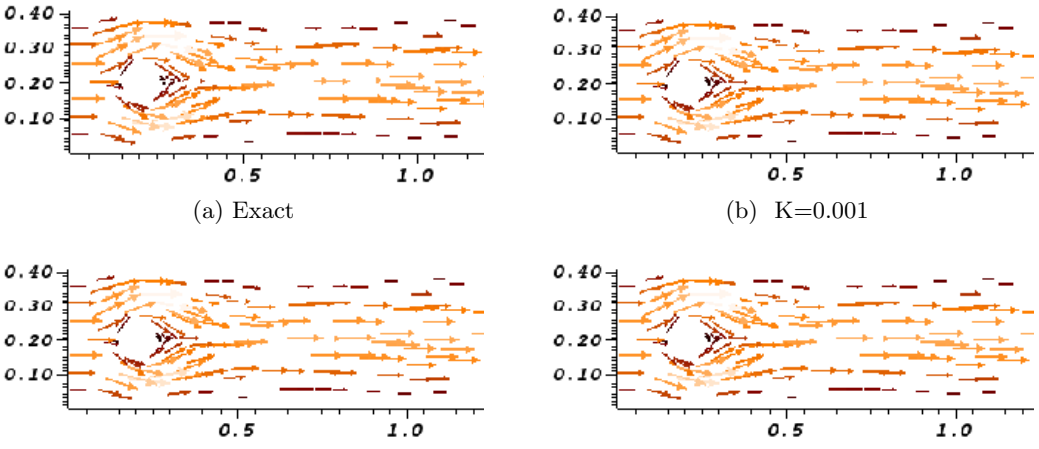

(a) Exact (b) K=0.001

(c) K=5 (d) K=35

Figure 6.13: Velocity plots for Navier-Stokes flow past a cylinder for $Re = 1$

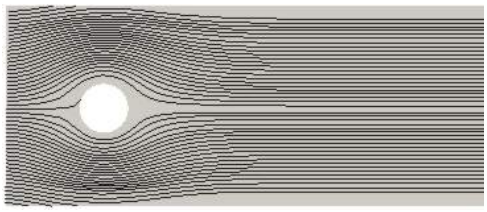

(a) Exact

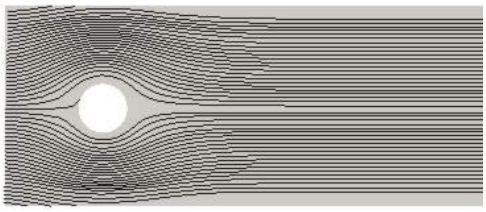

(b) K=0.001

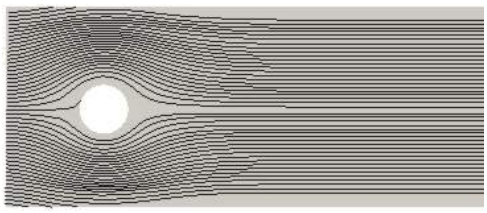

(c) K=5

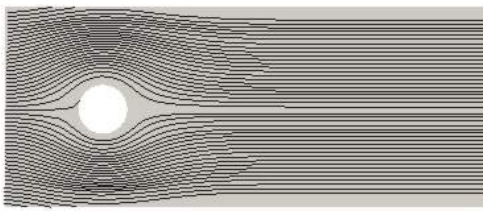

(d) K=35

Figure 6.14: Streamline plots for Navier-Stokes flow past a cylinder for $Re = 1$

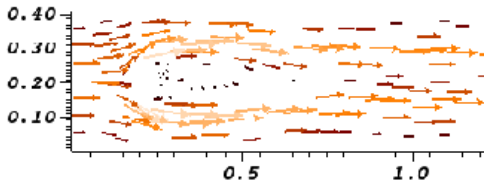

(a) Exact

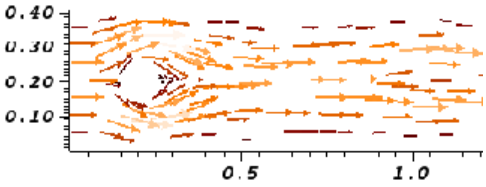

(b) K=0.001

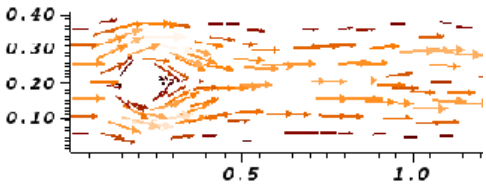

(c) K=5

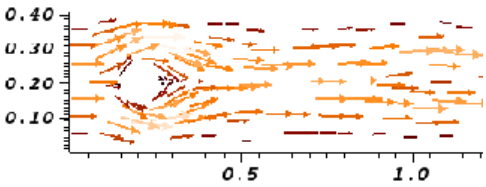

(d) K=35

Figure 6.15: Velocity plots for Navier-Stokes flow past a cylinder for $Re = 1000$

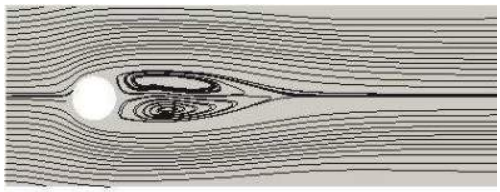

(a) Exact

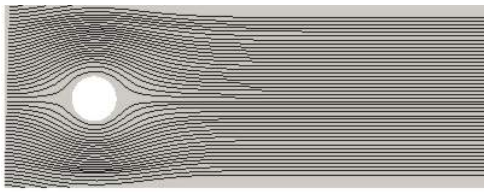

(b) K=0.001

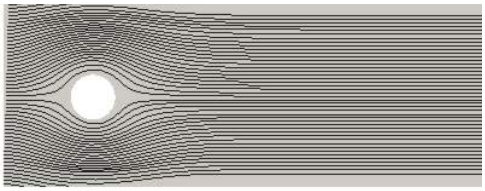

(c) K=5

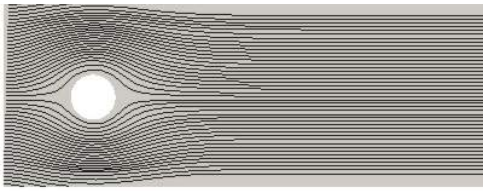

(d) K=35

Figure 6.16: Streamline plots for Navier-Stokes flow past a cylinder for $Re = 1000$

formulation. Using FEM in the present variational approach method, it is shown that the velocities are recovered almost exactly for Stokes flow forced by potential. For Navier-Stokes flow the method performs very well for $Re = 1$ compared to $Re = 1000$. This is because Stokes flow is a linearized version of the Navier-Stokes flow for low Reynolds number. But nevertheless, in both the cases the physical features of fluid flow like vortex structures are captured well. This is particularly attractive for the cloud motion problem. The simplicity of our variational approach makes it computationally attractive. In the next chapter, we extend this variational approach to track high Reynolds number flows as well by including non-linear effects.

Chapter 7

Time Dependent Flow Recovery

7.1 Introduction

In the previous chapter, we had used a variational approach by minimizing a functional with data given at a fixed time t to recover incompressible flows. We found out that even though the method was efficient and recovered Stokes flow exactly, it fails to recover vortex structures for high Reynolds number flows. As a consequence, in this chapter, we formulate a minimization problem by penalizing the tracking or advection error over space and time. Hence we also consider time integrals. We use the vorticity-streamfunction formulation for the Euler and Navier-Stokes equations. This is because our main aim is to capture vortex structures and vorticity can be directly obtained as an output rather than computing the curl of the velocity which could lead to numerical errors. We present three kind of formulations based on the Helmholtz decomposition of the velocity vector field, use a space-time discontinuous Galerkin finite element method and numerically investigate the motion due to vortex flows satisfying Euler and Navier-Stokes equations at high Reynolds number.

7.2 Variational Formulation

To estimate fluid flow, passive scalars propagated by the flow are traced. Examples of such scalars are smoke and brightness patterns of dense rain-bearing clouds whose intensity remains constant atleast for a short time span. These scalars can be represented by a function $E : \Omega \times \mathbb{R}^+ \longrightarrow \mathbb{R}$ so that $E(x, y, t)$ for $(x, y) \in \Omega$ represents snapshots of the image of the scalars at various times $t \in \mathbb{R}^+$. Here Ω is a bounded convex subset of $\mathbb{R}^2$. We assume our image $E(x, y, t) \in W^{1,\infty}(\Omega)$, for each t and hence in $L^2(\Omega)$ (as Ω is bounded). The constant brightness assumption of the tracers gives us the optical flow equation

$$\frac{\partial E}{\partial t} + \widetilde{\mathbf{U}} \cdot \nabla E = 0 \tag{7.1}$$

where $\widetilde{\mathbf{U}}(\mathbf{x}, t)$ is the optical velocity i.e, the velocity of the fluid which propagates the scalars in the images. Estimating fluid motion of E is the inverse problem of determining $\widetilde{\mathbf{U}}$ from the image sequence represented by E. To estimate fluid flow, we need to include flow dynamics as constraints. We assume $\widetilde{\mathbf{U}}$ satisfies the 2D incompressible Euler (Navier-Stokes) equations i.e the vorticity $\omega = \nabla \times \widetilde{\mathbf{U}}$ satisfies

$$\begin{aligned} &\omega_t + \widetilde{\mathbf{U}} \cdot \nabla \omega = 0 \ (\frac{1}{Re}\Delta\omega), \quad (\mathbf{x}, t) \in \Omega \times (0, T] \\ &\omega(\mathbf{x}, 0) = \omega_0(\mathbf{x}), \quad \mathbf{x} \in \Omega \end{aligned} \tag{7.2}$$

where Re is the Reynolds number. We also impose the boundary condition

$$\omega = 0, \quad \mathbf{x} \in \partial\Omega_- \ (\partial\Omega \text{ for Navier-Stokes})$$

where $\partial\Omega_-$ is the inflow boundary

$$\partial\Omega_- = \{\mathbf{x} \in \partial\Omega \colon \widetilde{\mathbf{U}} \cdot n < 0\} \tag{7.3}$$

where n is the unit normal on the boundary of Ω. We assume that all vortex stay in the interior of the domain at all times $t \in [0, T]$. Again, as $\nabla \cdot \widetilde{\mathbf{U}} = 0$, $\exists \ \ \psi : \Omega \times \mathbb{R}^+ \longrightarrow \mathbb{R}$, called streamfunction, such that

$$\widetilde{\mathbf{U}}(\mathbf{x}, t) = \nabla^{\perp}\psi(\mathbf{x}, t).$$

Hence ψ is governed by

$$-\Delta\psi = \omega \quad \text{ in } \Omega. \tag{7.4}$$

For solving (7.4), we impose the boundary condition

$$\frac{\partial\psi}{\partial n} = g(\mathbf{x}, t) \qquad \text{on } \partial\Omega \quad \forall t \in [0, T]. \tag{7.5}$$

For uniqueness, ψ is chosen to satisfy

$$\int_\Omega \psi = 0 \qquad \forall t \in [0, T]. \tag{7.6}$$

We assume $\omega_0 \in L^\infty(\Omega)$ and $g(\cdot, t) \in H^{-1/2}(\partial\Omega) \quad \forall t \in [0, T]$. Given E, our aim is to determine appropriate g and ω_0 so that (7.2), (7.3), (7.4), (7.5), (7.6) can be solved to determine $\widetilde{\mathbf{U}}$. Such a pair (g, ω_0) can be obtained by minimizing the functional

$$J(\psi(\omega_0, g), \omega_0, g) = \frac{1}{2}\int_Q (E_t + \nabla^{\perp}\psi.\nabla E)^2 + \frac{\alpha^2}{2}\int_0^T \int_{\partial\Omega} |g|^2 + \frac{\beta^2}{2}\int_\Omega |\omega_0|^2 \tag{7.7}$$

where α and β are regularization parameters and $Q = (0, T) \times \Omega$. The minimization problem can be stated as

$$\min_{(\omega_0, g)} \quad \{J(\omega_0, g) : (7.2) - (7.6) \text{ is satisfied.}\} \tag{P}$$

We consider three different formulations. In the first case, a linearized version of (7.2) is considered where the total velocity is a perturbation of a known flow which is constant. The motivation for such an assumption originates from the Helmholtz decomposition of the velocity vector field. Since we are dealing with vortex based flows, our aim is to capture vortex structures well. So splitting up the velocity field into its translational and rotational part with known translational components enables us to capture vortex structures well. This is also demonstrated in the numerical examples. At the theoretical level, we also show existence of a unique velocity field which is very important from the computational perspective. In the second case, we again consider a linearized version of (7.2) where the total velocity is a perturbation of an unknown constant velocity. This in principle is the Helmholtz decomposition with both the translational and rotational part unknown. From the numerical test cases in Section 7.7, it can be seen that vortex properties are recovered well. Finally, we consider the general case when the total non-linear velocity is unknown. Since there is no extra assumption on the properties on the velocity field, we are unable to show existence of a unique velocity field which leads to a not so good recovery of vortex structures. This is expected as the flow dynamics does not include rotational properties and without prior information of the boundary conditions and initial vorticity, it poses a major challenge in recovery of vortex based flows.

7.3 Formulation 1 - Linearized Flow

We assume

$$\widetilde{\mathbf{U}} = \mathbf{U}_0 + \mathbf{U}$$

where $\mathbf{U}_0$ is a known constant and $\mathbf{U}$ is assumed to be small relative to $\mathbf{U}_0$. Linearizing (7.2) about $\mathbf{U}_0$ and combining (7.4), (7.6) we get

$$\begin{aligned} &\omega_t + \mathbf{U}_0 \cdot \nabla\omega = 0 \ (\frac{1}{Re}\Delta\omega), \quad (\mathbf{x}, t) \in \Omega \times (0, T] \\ &\omega(\mathbf{x}, 0) = \omega_0(\mathbf{x}), \quad \mathbf{x} \in \Omega \end{aligned} \tag{7.8}$$

$$\begin{aligned} -\Delta\psi &= \omega, \quad \text{in } \Omega \\ \frac{\partial\psi}{\partial n} &= g, \quad \text{on } \partial\Omega \\ \int_\Omega \psi &= 0 \qquad \forall t \in [0, T] \end{aligned} \tag{7.9}$$

where $\mathbf{U} = \nabla^\perp\psi$ and $\omega = \nabla \times \mathbf{U}$. The boundary condition now becomes

$$\omega = 0, \quad \mathbf{x} \in \partial\Omega_- \ (\partial\Omega \text{ for Navier-Stokes}) \tag{7.10}$$

where $\partial\Omega_-$ is the inflow boundary given as

$$\partial\Omega_- = \{\mathbf{x} \in \partial\Omega \colon \mathbf{U}_0 \cdot n < 0\}$$

where n is the unit normal on the boundary of Ω.
Our aim is to determine $\mathbf{U}$, and hence the total velocity $\widetilde{\mathbf{U}}$, by minimizing the functional

$$J(g, \omega_0) = \frac{1}{2}\int_Q (E_t + (\nabla^\perp\psi(g, \omega_0) + \mathbf{U}_0) \cdot \nabla E)^2 + \frac{\alpha^2}{2}\int_0^T \int_{\partial\Omega} |g|^2 + \frac{\beta^2}{2}\int_\Omega |\omega_0|^2 \tag{P_1}$$

subject to (7.8), (7.9) and (7.10).

7.3.1 Existence and Uniqueness of Minimizer

We want to show existence of a unique minimizer of (P_1). Let $Z = L^2([0, T]; H^{\frac{1}{2}}(\partial\Omega)) \times L^2(\Omega)$ with the norm $\|(g, \omega_0)\|_Z = \left(\int_0^T \int_{\partial\Omega} |g|^2 + \int_\Omega |\omega_0|^2\right)^{1/2}$.

Theorem 7.3.1. *The functional J given in (P_1) is strictly convex with respect to (ω_0, g)*

Before proving Theorem (7.3.1) we show that (ψ, ω) given by (7.8) and (7.9) is linear in (ω_0, g).

Lemma 7.3.1. *(ψ, ω) given by (7.8) and (7.9) is linear in $(g, \omega_0) \in L^2([0, T]; H^{\frac{1}{2}}(\partial\Omega)) \times L^2(\Omega)$*

Proof. Let (ψ_1, ω_1) and (ψ_2, ω_2) satisfy (7.8) and(7.9) for (g^1, ω_0^1) and $(g^2, \omega_0^2) \in L^2([0, T]; H^{\frac{1}{2}}(\partial\Omega)) \times L^2(\Omega)$ respectively. Let us consider $\widetilde{\omega}_0 = \alpha\omega_0^1 + \beta\omega_0^2$ for $\alpha, \beta \in \mathbb{R}$. Then we see that $\widetilde{\omega} = \alpha\omega_1 + \beta\omega_2$ satisfy (7.8) for initial condition $\widetilde{\omega}_0$. Now let $\widetilde{\psi} = \alpha\psi_1 + \beta\psi_2$. Then we see that $\widetilde{\psi}$ satisfies

$$\begin{aligned} -\Delta\widetilde{\psi} &= \widetilde{\omega}, \qquad \text{in } \Omega \\ \frac{\partial\widetilde{\psi}}{\partial n} &= \widetilde{g}, \qquad \text{on } \partial\Omega \\ \int_\Omega \widetilde{\psi} &= 0 \qquad \forall t \in [0, T] \end{aligned} \tag{7.11}$$

where $\widetilde{g} = \alpha g^1 + \beta g^2$. This shows (ψ, ω) is linear in (g, ω_0) □

Proof of Theorem 7.3.1. Let $X_1 = (g^1, \omega_0^1)$ and $X_2 = (g^2, \omega_0^2)$. Then for $0 < \lambda < 1$, we have

$$\begin{aligned}
J(\lambda X_1 + (1-\lambda)X_2) &= \frac{1}{2}\int_Q \{E_t + \Big[\nabla^\perp \psi(\lambda X_1 + (1-\lambda)X_2) + \mathbf{U}_0\Big] \cdot \nabla E\}^2 \\
&+ \frac{\alpha^2}{2}\int_0^T \int_{\partial\Omega} \left|\lambda g^1 + (1-\lambda)g^2\right|^2 + \frac{\beta^2}{2}\int_\Omega \left|\lambda\omega_0^1 + (1-\lambda)\omega_0^2\right|^2 \\
&= \frac{1}{2}\int_Q \{(E_t + \mathbf{U}_0 \cdot \nabla E) + \Big[\nabla^\perp \psi(\lambda X_1 + (1-\lambda)X_2)\Big] \cdot \nabla E\}^2 \\
&+ \frac{\alpha^2}{2}\int_0^T \int_{\partial\Omega} \left|\lambda g^1 + (1-\lambda)g^2\right|^2 + \frac{\beta^2}{2}\int_\Omega \left|\lambda\omega_0^1 + (1-\lambda)\omega_0^2\right|^2 \\
&\leq \frac{1}{2}\int_Q 2(E_t + \mathbf{U}_0 \cdot \nabla E)^2 + \Big(\Big[\lambda\nabla^\perp \psi(X_1) + (1-\lambda)\nabla^\perp \psi(X_2)\Big] \cdot \nabla E\Big)^2 \\
&+ \frac{1}{2}\int_Q 2(E_t + \mathbf{U}_0 \cdot \nabla E) \cdot \Big(\Big[\lambda\nabla^\perp \psi(X_1) + (1-\lambda)\nabla^\perp \psi(X_2)\Big] \cdot \nabla E\Big) \\
&+ \frac{\alpha^2}{2}\left(\lambda\int_0^T \int_{\partial\Omega} \left|g^1\right|^2 + (1-\lambda)\int_0^T \int_{\partial\Omega} \left|g^2\right|^2\right) \\
&+ \frac{\beta^2}{2}\left(\lambda\int_\Omega \left|\omega_0^1\right|^2 + (1-\lambda)\int_\Omega \left|\omega_0^2\right|^2\right) \\
&\qquad \text{(Using Lemma 7.3.1 and convexity of } L^2 \text{ norm)}
\end{aligned} \tag{7.12}$$

Equality holds iff $X_1 = X_2$. So for $X_1 \neq X_2$, we have

$$J(\lambda X_1 + (1-\lambda)X_2) < \lambda J(X_1) + (1-\lambda)J(X_2), \qquad 0 < \lambda < 1$$

This shows J is strictly convex with respect to (ω_0, g). □

Theorem 7.3.2. *The constraint set $C = \{\omega \in L^2([0,T]; L^2(\Omega)) : \omega$ satisfies (7.8) and (7.10)$\}$ is given by the level set of a convex function.*

Proof. For the vorticity equation in (7.8) corresponding to Euler's flow, there is a unique solution $\omega \in L^2([0,T]; L^2(\Omega))$ and it can be given by $S(t)\omega_0$ where $(S(t))_{t\geq 0}$ is a C_0-semi-group of contractions in $L^2([0,T]; L^2(\Omega))$ [11]. For the vorticity equation in (7.8) corresponding to Navier-Stokes flow, there exists a unique solution $\omega \in L^2([0,T]; L^2(\Omega))$ and it can be given by $\widetilde{S}(t)\omega_0$ where $(\widetilde{S}(t))_{t\geq 0}$ is a C_0-semi-group of contractions in $L^2([0,T]; L^2(\Omega))$ [21]. Both the solutions for Euler and Navier-Stokes equations represented by ω satisfy

$$\|\omega(.,t)\|_{L^2(\Omega)} \leq \|\omega_0\|_{L^2(\Omega)} \tag{7.13}$$

by the boundedness of the operator S. Let

$$A : L^2(\Omega) \longrightarrow L^2([0,T]; L^2(\Omega))$$

be defined as

$$A(\omega_0) = S(t)\omega_0 \text{ (or } \widetilde{S}(t)\omega_0)$$

where ω satisfies (7.8). As $S(\widetilde{S})$ is a bounded linear bijection, A is a bounded linear bijection. Consider the function

$$F(\omega_0) = A(\omega_0) - \omega$$

where $\omega \in L^2([0,T]; L^2(\Omega))$ and satisfies (7.8). This is a convex bijection and hence the constraint set (7.8) and (7.10) is given by

$$F(\omega_0) = 0$$

i.e. the level set of a convex function. □

Theorem 7.3.3. *The constraint set (7.9) is given by the level set of a convex function.*

Proof. The constraint set (7.9) is given as

$$\begin{aligned} &-\Delta\psi(\mathbf{x},t)=\omega, \quad \mathbf{x}\in\Omega \\ &\frac{\partial\psi}{\partial n}=g(\mathbf{x},t), \text{ in } \partial\Omega, \quad \forall t\in[0,T]. \\ &\int_\Omega \psi=0 \qquad \forall t\in[0,T] \end{aligned} \tag{7.14}$$

We have

$$-\int_\Omega(\Delta\psi(\mathbf{x},t))\phi(\mathbf{x})dx=-\int_\Omega\omega(\mathbf{x},t)\phi(\mathbf{x})dx, \qquad \forall\phi\in H^1(\Omega) \tag{7.15}$$

Using integration by parts we obtain

$$\int_\Omega\nabla\psi(\mathbf{x},t)\cdot\nabla\phi(\mathbf{x})-\int_{\partial\Omega}g(\mathbf{x},t)\phi(\mathbf{x})=-\int_\Omega\omega(\mathbf{x},t)\phi(\mathbf{x}) \qquad \forall t\in[0,T] \tag{7.16}$$

Setting $\phi=\psi$, taking modulus on both sides of (7.16) and using Holder's inequality and Poincare-Wirtinger inequality gives

$$\|\psi\|_{H^1(\Omega)}\leq\|g\|_{H^{\frac{1}{2}}(\partial\Omega)}+\|\omega\|_{L^2(\Omega)} \tag{7.17}$$

which implies

$$\int_0^T\|\psi\|_{H^1(\Omega)}\leq\int_0^T\|g\|_{H^{\frac{1}{2}}(\partial\Omega)}+\int_0^T\|\omega\|_{L^2(\Omega)} \tag{7.18}$$

where

$$\|g\|_{H^{\frac{1}{2}}(\partial\Omega)}=\int_{\partial\Omega}|g|^2$$

Let us consider the solution operator of (7.14)

$$B:L^2([0,T];H^1(\Omega))\longrightarrow L^2([0,T];H^{\frac{1}{2}}(\partial\Omega))$$

$$\psi\longmapsto g$$

We now show that B^{-1} is a bounded linear bijection. For a fixed $\omega\in L^2([0,T];L^2(\Omega))$, given $g\in L^2([0,T];H^{\frac{1}{2}}(\partial\Omega))$ there exists a unique $\psi\in L^2([0,T];H^1(\Omega))$ such that ψ satisfies (7.14). This shows that B is a bijection. Also B^{-1} is convex for if ψ_1 and ψ_2 satisfy (7.14) for boundary data g_1 and g_2 respectively then $\lambda\psi_1+(1-\lambda)\psi_2$ is a solution of (7.14) for boundary data $\lambda g_1+(1-\lambda)g_2$. By (7.18), B^{-1} is bounded. Hence B^{-1} is a bounded linear bijection. Now consider the function

$$G(g)=B^{-1}(g)-\psi$$

for any fixed $\omega\in L^2([0,T];L^2(\Omega))$ where $\psi\in L^2([0,T];H^1(\Omega))$ and satisfies (7.14). This is a convex bijection and hence the constraint set (7.14) is given by

$$G(g)=0$$

i.e. the level set of a convex function. □

So the set

$$C=\{(g,\omega_0)\in Z:F(\omega_0)=0, \quad G(g)=0\} \tag{7.19}$$

is a closed convex subset of Z. We now show that J is continuous and coercive.

Theorem 7.3.4. *The functional J given in (P_1) is continuous*

Proof. We will use Theorem 6.3.3 to prove our statement. We assume

$$\|E\|_{W^{1,\infty}(Q)} \leq M. \tag{7.20}$$

As $0 \in Z$, we consider a neighborhood of zero given as $N_1 = \{(g, \omega_0) : \|(g, \omega_0)\|_Z < 1\}$. Now

$$\begin{aligned} |J(g,\omega_0)| &= \frac{1}{2}\int_Q (E_t + (\nabla^\perp\psi(g,\omega_0) + \mathbf{U}_0).\nabla E)^2 + \frac{\alpha^2}{2}\int_0^T\int_{\partial\Omega}|g|^2 + \frac{\beta^2}{2}\int_\Omega |\omega_0|^2 \\ &\leq \frac{1}{2}\int_Q \Big(E_t^2 + (\nabla^\perp\psi(g,\omega_0)\cdot\nabla E)^2 + 2E_t(\nabla^\perp\psi(g,\omega_0)\cdot\nabla E)\Big) + C_1\|(g,\omega_0)\|_Z^2 \end{aligned}$$

Using Hölder's inequality and (7.20), (7.13) and (7.17) we get

$$\begin{aligned} |J(g,\omega_0)| &< \frac{3M}{2}\mu(Q) + M^2\|(g,\omega_0)\|_Z^2 + C_1\|(g,\omega_0)\|_Z^2 \\ &< \frac{3M}{2}\mu(Q) + M^2 + C_1 \\ &< \infty. \end{aligned}$$

where $\mu(Q)$ is the measure of Q. This gives us $J(U)$ is bounded above in N_1. As J is convex (by Theorem 7.3.1) it implies J is continuous for all $U \in Z$ (by Theorem 6.3.3). □

Theorem 7.3.5. *The functional J given in (P_1) is coercive for $\alpha > 0$ and $\beta > 0$.*

Proof. From (P_1) we get

$$J(g,\omega_0) \geq \frac{\alpha^2}{2}\int_0^T\int_{\partial\Omega}|g|^2 + \frac{\beta^2}{2}\int_\Omega|\omega_0|^2$$

As $\alpha,\ \beta > 0$, let $L = \min\{\alpha, \beta\}$. Then $L > 0$. So we have

$$J(g,\omega_0) \geq \langle\left(\int_0^T\int_{\partial\Omega}|g|^2 + \int_\Omega|\omega_0|^2\right) = L\|(g,\omega_0)\|_Z^2$$

So if $\|(g,\omega_0)\|_Z \to \infty$ then $J(g,\omega) \to \infty$. Hence J is coercive. □

J is a strictly convex continuous coercive functional on Z and the constraint set C given in (7.19) is convex. By Theorem 6.3.4, the convex minimization problem (7.7) has a unique global minimizer.

7.3.2 Optimization using Lagrange Multipliers

In Section (7.3.1), we showed existence of a unique minimizer of J defined in (P_1). Now we determine the optimum solution. The functional J is to be minimized subject to PDE constraints. This is done by the use of Lagrange multipliers [46]. We first write down the weak forms of (7.8) and (7.9). Multiplying (7.8) with a test function $y \in H^1([0,T]; L^2(\Omega))$, integrating by parts with respect to t and incorporating initial conditions for ω, we get

$$\int_Q(-\omega y_t + (\mathbf{U}_0\cdot\nabla\omega)y) + \int_\Omega\omega(T)y(T) - \omega_0 y(0) = 0. \tag{7.21}$$

If we consider the Navier-Stokes equation then performing an integration by parts over Ω and using boundary conditions on ω, we get

$$\int_Q(-\omega y_t + (\mathbf{U}_0\cdot\nabla\omega)y) + \int_\Omega\omega(T)y(T) - \omega_0 y(0) + \frac{1}{Re}\int_Q\nabla\omega\cdot\nabla y = 0. \tag{7.22}$$

Multiplying (7.9) with a test function $\phi \in L^2([0,T]; H_a^1(\Omega))$, integrating by parts over Ω, and using boundary conditions on ψ we get

$$\int_Q (\nabla\psi \cdot \nabla\phi - \omega\phi) - \int_0^T \int_{\partial\Omega} g\phi = 0. \tag{7.23}$$

Hence to determine the optimal solution, the auxiliary functional can be written as

$$\begin{aligned}\widetilde{J}(y,\omega,\phi,\psi,g,\omega_0) = J + \int_Q (-\omega y_t + (\mathbf{U}_0 \cdot \nabla\omega)y) + \int_\Omega \omega(T)y(T) - \omega_0 y(0) \\ + \int_Q (\nabla\psi \cdot \nabla\phi - \omega\phi) - \int_0^T \int_{\partial\Omega} g\phi \; (+\frac{1}{Re}\int_Q \nabla\omega \cdot \nabla y)\end{aligned} \tag{7.24}$$

where y is the Lagrange Multiplier corresponding to the first constraint (7.8) and ϕ is the Lagrange Multiplier corresponding to the second constraint (7.14). Here $\omega, y \in L^2([0,T]; L^2(\Omega))$ and $\psi, \phi \in L^2([0,T]; H_a^1(\Omega))$ where

$$H_a^1(\Omega) = \{\psi \in H^1(\Omega) : \int_\Omega \psi = 0\}$$

7.3.3 PDE's obtained after minimization of $\widetilde{J}$

Taking the Gateaux derivative of $\widetilde{J}$ in (7.24) wrt $y, \omega, \phi, \psi, g, \omega_0$, the standard optimality conditions [100] are

$$\frac{\partial\widetilde{J}}{\partial y} = 0, \; \frac{\partial\widetilde{J}}{\partial\omega} = 0, \; \frac{\partial\widetilde{J}}{\partial\phi} = 0, \; \frac{\partial\widetilde{J}}{\partial\psi} = 0, \; \frac{\partial\widetilde{J}}{\partial g} = 0, \; \frac{\partial\widetilde{J}}{\partial\omega_0} = 0. \tag{7.25}$$

The first and second equations in (7.25) gives the vorticity equation and its adjoint

$$\begin{aligned}&\omega_t + \mathbf{U}_0 \cdot \nabla\omega = 0 \; (\frac{1}{Re}\Delta\omega) \\ &\omega(\mathbf{x}, 0) = \omega_0(\mathbf{x}) \\ &\omega = 0, \quad \mathbf{x} \in \partial\Omega_- \; (\partial\Omega)\end{aligned} \tag{7.26}$$

$$\begin{aligned}&y_t + \mathbf{U}_0 \cdot \nabla y = 0 \; (-\frac{1}{Re}\Delta y) \\ &y(\mathbf{x}, T) = 0 \\ &y = 0 \text{ on } \partial\Omega\end{aligned} \tag{7.27}$$

The third and fourth equations in (7.25) gives the equation for streamfunction and its adjoint

$$\begin{aligned}&-\Delta\psi = \omega, \quad \mathbf{U} = \nabla^\perp\psi \\ &\frac{\partial\psi}{\partial n} = g \\ &\int_\Omega \psi = 0\end{aligned} \tag{7.28}$$

$$\begin{aligned}&\Delta\phi = -\nabla E \cdot \nabla^\perp F \\ &\frac{\partial\phi}{\partial n} = -F\frac{\partial E}{\partial t} \\ &\int_\Omega \phi = 0\end{aligned} \tag{7.29}$$

where $F = E_t + \widetilde{\mathbf{U}} \cdot \nabla E$. The fifth and sixth equations in (7.25) gives the optimality conditions

$$\alpha^2 g = \phi, \qquad \beta^2\omega_0 = y(0) \tag{7.30}$$

7.4 Finite Element Method for problem (P_1)

Equations (7.26), (7.27), (7.28), (7.29) and (7.30) are solved using space-time finite elements, considering time as the third dimension. The equations (7.26) and (7.27) represent the forward vorticity equation and its backward adjoint equation. For Navier-Stokes flow, the solutions to the equations are smooth because of the presence of an extra diffusivity term on the right hand side. So continuous Galerkin finite elements are used. For Euler's flow, vorticity is non-smooth. Since our aim is to capture vortex structures well, we use discontinuous Galerkin method. The equations (7.28) and (7.29) represent the streamfunction equation and its adjoint equation which are elliptic in nature and hence they are solved using continuous Galerkin finite elements.

7.4.1 Discontinuous Galerkin formulation for vorticity equation for Euler's flow

Equations (7.26) and (7.27) are solved using the finite element method. Since we are interested in tracking discontinuous vortices, discontinuous Galerkin finite elements are used. It is an explicit method and hence there is no global matrix inversion. Also stability and energy conservation is maintained. The normal velocity $\mathbf{U}\cdot n$ is continuous across the element boundary and hence use of correct upwind flux is possible maintaining the stability [25, 26]. Let T_h be a triangulation of domain Q and consider the space of piecewise polynomials

$$V_h^k = \{v \in L^2(Q) : V|_K \in \mathbb{P}_0 \quad \forall K \in T_h\} \tag{7.31}$$

where $\mathbb{P}_0(K)$ is the space of constant polynomials on K. The vorticity equation associated to Euler's flow given in (7.26) can be rewritten in conservative form as

$$\widetilde{\nabla}\cdot\omega B = 0$$

where

$$\widetilde{\nabla} = (\frac{\partial}{\partial x}, \frac{\partial}{\partial y}, \frac{\partial}{\partial t})$$

and

$$B = (u_0, v_0, 1)$$

Multiplying by a function $v \in L^2(Q)$ with $\text{supp}(v) = K$ and integrate by parts

$$\int_{\partial K}(B.n)\omega v - \int_K \omega(B.\nabla v) = 0$$

We consider the upwind flux to approximate the first term in the integral given by

$$H(\omega_+, \omega_-, n) = (B.n)^+\omega_+ + (B.n)^-\omega_-$$

where

$$(B.n)^+\omega_+ + (B.n)^-\omega_- = \begin{cases} (B.n)\omega_+ & \text{if } (B.n) \geq 0 \\ (B.n)\omega_- & \text{if } (B.n) < 0 \end{cases}$$

Then the DG scheme in K is given as

$$\int_{\partial K} H(\omega_+^h, \omega_-^h, n)v^h - \int_K \omega^h(B.\nabla v^h) = 0$$

Incorporating the boundary conditions and adding the equations for all elements the discrete problem is to find $\omega^h \in V_h^k$ such that

$$-\sum_{K\in\tau_h}\int_K \omega^h(B.\nabla v^h) + \sum_{e\in\Gamma_I}\int_e H(\omega_+^h, \omega_-^h, n)[\![v^h]\!] + \int_{\Gamma_-} H(\omega_+^h, \omega_0, n) + \int_{\Gamma_+}((B.n)\omega^h v^h) = 0$$
$$\forall v^h \in V_h^k \tag{7.32}$$

where Γ_I represents the interior edges, Γ_- represents the inflow boundary given by

$$\Gamma_- = \{\mathbf{x} \in \partial\Omega : B.n(\mathbf{x}) < 0\} \tag{7.33}$$

and Γ_+ represents the outflow boundary. A detailed analysis of the scheme can be found in [27].

For the adjoint equation (7.27) the same DG formulation in (7.32) is used with ω^h replaced y^h, $B = (-u_0, -v_0, -1)$ and inflow boundary conditions as $y^h = 0$ using (7.33).

7.4.2 Continuous Galerkin formulation for vorticity equation for Navier-Stokes

For the vorticity equation associated to Navier-Stokes flow given in (7.26) let us define the continuous space

$$W_h^k = \{v \in C^0(Q) : V|_K \in \mathbb{P}_k \quad \forall K \in T_h\} \tag{7.34}$$

where $\mathbb{P}_k(K)$ is the space of polynomials of degree k on K. We choose $k = 1$ for our computations unless otherwise mentioned. The discrete problem is to find $\omega^h \in W_h^k$ such that

$$\int_Q (-\omega^h v_t^h + (\mathbf{U}_0 \cdot \nabla\omega^h)v^h) + \frac{1}{Re}\int_Q \nabla\omega^h \cdot \nabla v^h + \int_\Omega \Big(\omega^h(T)v^h(T) - \omega_0 v^h(0)\Big) = 0 \qquad \forall v^h \in W_h^k \tag{7.35}$$

In a similar way, the discrete problem for the adjoint equation (7.27) is to find $y^h \in W_h^k$ such that

$$\int_Q \left(y^h v_t^h - (\mathbf{U}_0 \cdot \nabla y^h)v^h\right) - \frac{1}{Re}\int_Q \nabla y^h \cdot \nabla v^h + \int_\Omega y^h(0)v^h(0)\Big) = 0 \qquad \forall v^h \in W_h^k \tag{7.36}$$

with inflow boundary conditions $y^h = 0$.

7.4.3 Continuous Galerkin formulation for streamfunction equation

To solve the streamfunction equation given by (7.28), the problem can be stated as: given ω and g, we want to find $\psi \in L^2([0,T]; H_a^1(\Omega))$ such that

$$\int_Q (\nabla\psi \cdot \nabla\bar{\psi} + \omega\bar{\psi}) - \int_0^T \int_{\partial\Omega} g\bar{\psi} = 0, \qquad \forall \bar{\psi} \in L^2([0,T]; H_a^1(\Omega)) \tag{7.37}$$

As (7.37) is solved using finite element method, we need to determine a discrete approximation of the space $L^2([0,T]; H_a^1(\Omega))$. But this is difficult in practice. Also the compatibility condition

$$\int_Q \omega + \int_0^T \int_{\partial\Omega} g = 0$$

needs to be satisfied for existence of solutions. In order to overcome these issues, Lagrange multipliers are used to add the constraint (7.6) to (7.37). So the modified weak formulation is to find $(\psi, s) \in L^2([0,T]; H^1(\Omega)) \times \mathbb{R}$ such that

$$\int_Q (\nabla\psi\cdot\nabla\bar{\psi}+\omega\bar{\psi}) + \int_Q \bar{s}\psi + \int_Q s\bar{\psi} - \int_0^T \int_{\partial\Omega} g\bar{\psi} = 0, \qquad \forall(\bar{\psi}, \bar{s}) \in L^2([0,T]; H^1(\Omega)) \times \mathbb{R} \tag{7.38}$$

This determines a discrete approximation of the space $L^2([0,T]; H^1(\Omega))$. Also the compatibility condition is automatically taken care of. So the discrete problem is to find $(\psi^h, s) \in W_h^k \times \mathbb{R}$ such that

$$\int_Q (\nabla\psi^h \cdot \nabla\bar{\psi}^h + \omega\bar{\psi}^h) + \int_Q \bar{s}\psi^h + \int_Q s\bar{\psi}^h - \int_0^T \int_{\partial\Omega} g\bar{\psi}^h = 0, \qquad \forall(\bar{\psi}^h, \bar{s}) \in W_h^k \times \mathbb{R} \tag{7.39}$$

A similar approach is used to solve the adjoint equation (7.29). After substituting the value of g and ω_0 from (7.30) in (7.32), (7.35) and (7.39), the discrete weak forms for the vorticity and streamfunction equations and their adjoints are combined and solved in a coupled way to obtain $\mathbf{U}$ and hence $\widetilde{\mathbf{U}}$. Next we describe the procedure to determine $E, E_t, \nabla E$.

7.4.4 Image Data

Our aim is to generate a sequence of synthetic images E and try to recover the velocity given the information of the derivatives of E. For this purpose E is chosen whose analytic expression at $t = 0$ is

$$E_0(x, y) = E(x, y, 0) = e^{-50[(x-1/2)^2+(y-1/2)^2]}.$$

To get E at all times, we solve the advection equation

$$\begin{aligned} &E_t + \mathbf{U}_e \cdot \nabla E = 0, \quad (\mathbf{x}, t) \in \Omega \times (0, T] \\ &E(x, 0) = E_0, \quad \text{in } \Omega \\ &E = 0, \quad \text{on } \Gamma_- \end{aligned} \tag{7.40}$$

where U_e represents the velocity obtained by solving incompressible Euler (7.42) or Navier-Stokes flow (7.43) using finite element method with appropriate boundary conditions and Γ_- is given by (7.33) with $B = (\mathbf{U}_e, 1)$. We want E and its derivatives to be differentiable. Hence the weak formulation can be stated as: find $E \in H^2_c(Q)$ such that

$$\int_Q (E_t + \mathbf{U}_e \cdot \nabla E)\widetilde{E} = 0$$

for all $\widetilde{E} \in H^2_0(Q)$ where

$$H^2_c(Q) = \{E \in H^2(Q) : E(x, 0) = E_0 \text{ in } \Omega,\ E = 0 \text{ on } \Gamma_-\}.$$

The discrete problem is to find $E^h \in W^k_h \cap H^2_c(Q)$ such that

$$\int_Q (E^h_t + \mathbf{U}_e \cdot \nabla E^h)\widetilde{E}^h = 0 \tag{7.41}$$

for all $\widetilde{E}^h \in W^k_h \cap H^2_0(Q)$. Equation (7.41) is solved using space-time finite element method with quadratic elements. Thus the solution E^h can be written as

$$E^h = \sum_i E^h_i \phi_i$$

where ϕ_i are basis functions of W^k_h which are continuous and piecewise quadratic polynomials in each element. Hence the derivatives of E are evaluated by computing the derivatives of ϕ_i. The unsteady incompressible Euler equations can be written in vorticity-streamfunction form as

$$\begin{aligned} &\omega_t + \mathbf{U}_e \cdot \nabla \omega = 0, \quad (\mathbf{x}, t) \in \Omega \times (0, T] \\ &\omega(\mathbf{x}, 0) = \omega_0(\mathbf{x}), \quad \mathbf{x} \in \Omega \\ &-\Delta\psi = \omega, \quad \text{in } \Omega \\ &\psi = g_1, \quad \text{on } \partial\Omega \end{aligned} \tag{7.42}$$

where $\mathbf{U}_e = \nabla^\perp \psi$ and $\omega = \nabla \times \mathbf{U}_e$. The unsteady incompressible Navier-Stokes equations can be written in vorticity-streamfunction form as

$$\begin{aligned} &\omega_t + \mathbf{U}_e \cdot \nabla \omega = \frac{1}{Re}\Delta\omega, \quad (\mathbf{x}, t) \in \Omega \times (0, T] \\ &\omega(\mathbf{x}, 0) = \omega_0(\mathbf{x}), \quad \mathbf{x} \in \Omega \\ &\Delta\psi = \omega, \quad \text{in } \Omega \\ &\psi = \psi_b, \quad \text{on } \partial\Omega \end{aligned} \tag{7.43}$$

where $\mathbf{U}_e = \nabla^{\perp}\psi$, $\omega = \nabla \times \mathbf{U}_e$ and Re is the Reynolds number. ψ_b is a prescribed boundary condition. In practice, derivatives of images will be computed using some finite differences which will introduce errors in the computed velocity.

7.4.5 Test Vortex Flows

Our domain is $Q = (0,T)\times\Omega$, where $\Omega = [0,1]\times[0,1]$. Two types of vortex flows are considered.
Vortex 1: The tangential velocity distribution for the initial condition for vorticity is prescribed between an outer radius $r = R_O$, and a core radius $r = R_C$. For radius greater than R_O the tangential velocity is set to be zero. The tangential velocity of the vortex is expressed as follows:

$$u_\theta(r) = \begin{cases} U_c\frac{r}{R_C} & r < R_C \\ Ar + \frac{B}{r} & R_C \le r \le R_O \end{cases} \tag{7.44}$$

where

$$A = \frac{U_C R_C}{R_O^2 - R_C^2}, B = \frac{U_C R_C R_O^2}{R_O^2 - R_C^2}$$

Then the initial vorticity is given by

$$\omega(x,y,0) = \begin{cases} 2A, & R_C \ge r \le R_0 \\ 2A_1, & r \le R_C \end{cases} \tag{V1}$$

where $A_1 = \frac{U_C}{R_C}$. Our computations are done with $R_O = 0.2$ and $R_C = 0.1$.
Vortex 2: A vortex patch whose initial condition is as follows:

$$\omega(x,y,0) = \begin{cases} -2, & 0.2 \le x \le 0.6,\ 0.1 \le y \le 0.4 \\ 2, & 0.2 \le x \le 0.6,\ 0.55 \le y \le 0.85 \\ 0 & \text{otherwise} \end{cases} \tag{V2}$$

On $\partial\Omega$, Dirichlet boundary condition $\mathbf{U}_e = (0.5, 0)$ is imposed. This is equivalent to Dirichlet boundary condition $\psi = -0.5y$.

7.4.6 Mesh

The computations are done using COMSOL Multiphysics. The domain Q is partitioned into tetrahedrons as shown in Figure 7.1. The average mesh size is $h = 0.01$. There are 196365 triangles with 1640836 degrees of freedom. Computations for Navier-Stokes flow are done with $Re = 1000$.

7.4.7 Solving equations (7.42) and (7.43)

To solve (7.42) and (7.43) using finite element method to determine $\mathbf{U}_e$, a similar kind of approach for the vorticity equations as described in Section 7.4.1 and 7.4.2 is used. For solving the streamfunction equation, the weak formulation is to find $\psi \in L^2([0,T]; H_b^1(\Omega))$ such that

$$\int_Q (\nabla\psi\cdot\nabla\bar{\psi} + \omega\bar{\psi}) - \int_0^T\int_{\partial\Omega} g\bar{\psi} = 0, \qquad \forall\bar{\psi} \in L^2([0,T]; H_b^1(\Omega)) \tag{7.45}$$

where

$$H_b^1(\Omega) = \{\psi \in H^1(\Omega) : \psi = \psi_b \text{ on } \partial\Omega\}$$

So the discrete problem is to find $\psi^h \in W_h^k \cap H_b^1$ such that

$$\int_Q (\nabla\psi^h\cdot\nabla\bar{\psi}^h + \omega\bar{\psi}^h) = 0, \qquad \forall\bar{\psi}^h \in W_h^k \cap H_0^1(\Omega) \tag{7.46}$$

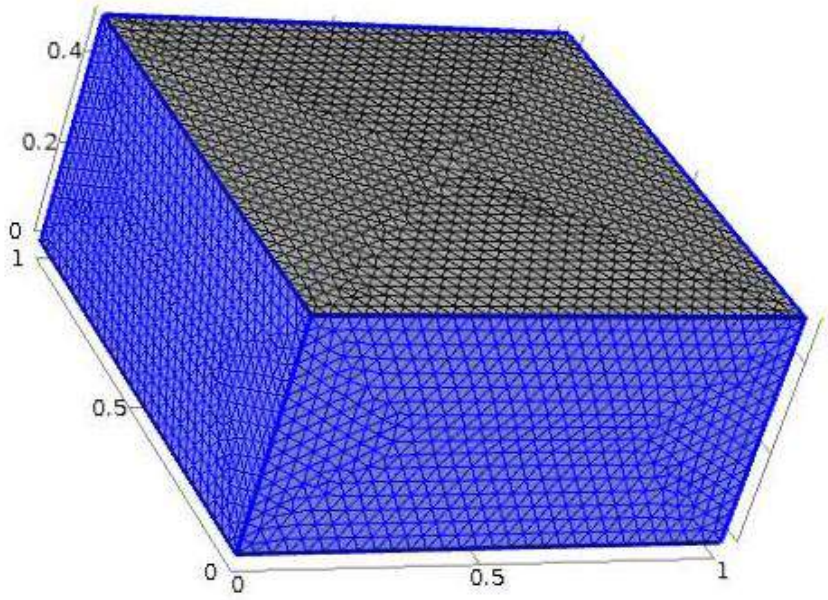

Figure 7.1: 3D mesh

The discrete weak forms as given in Section 7.4.1 and (7.46) for the vorticity equation and streamfunction equation are combined and solved in a coupled way to obtain $\mathbf{U}_e$. Finally the relative L^2 error in velocity is defined as

$$\text{Relative } L^2 \text{ error} = \frac{\|\mathbf{U}_e - \mathbf{U}_o\|}{\|\mathbf{U}_e\|} \tag{7.47}$$

and the advection error is defined as

$$\text{Advection Error} = \|E_t + \mathbf{U}_o \cdot \nabla E\| \tag{7.48}$$

where $\mathbf{U}_e$ is the exact velocity and $\mathbf{U}_o$ is the obtained velocity and the norm $\|\cdot\|$ is the usual L^2 norm in Q for vector functions.

7.5 Numerical Examples

7.5.1 Advection of vortex 1 and vortex 2 under Euler's flow

The exact flow is given by solving (7.42) with initial vorticity given by (7.44) and (V2) and boundary condition for streamfunction given in Section (7.4.5). Figure (7.2) and (7.3) shows the velocity and vorticity plots at time $t = 0.5$. The figures show that the translational velocity, which is the constant velocity $(0.5, 0)$, is well captured. Also the vortex movement is well recovered. Table (7.1) and (7.2) shows the relative L^2 error and the advection error for various values of α and β. It has been numerically tested that for higher values of α and β of the order of 10^2 or greater gives bad results. This is because we are over-penalizing the initial vorticity and the boundary condition for the streamfunction leading to larger errors in the flow estimation. So for best results, we choose the value of α and β to be in the range of $[0.1, 10]$.

7.5.2 Advection of vortex 1 and vortex 2 under Navier-Stokes flow

The exact flow is given by solving (7.43) with initial vorticity given by (7.44) and (V2) and boundary condition for streamfunction given in Section (7.4.5). Figure (7.4) and (7.5) shows

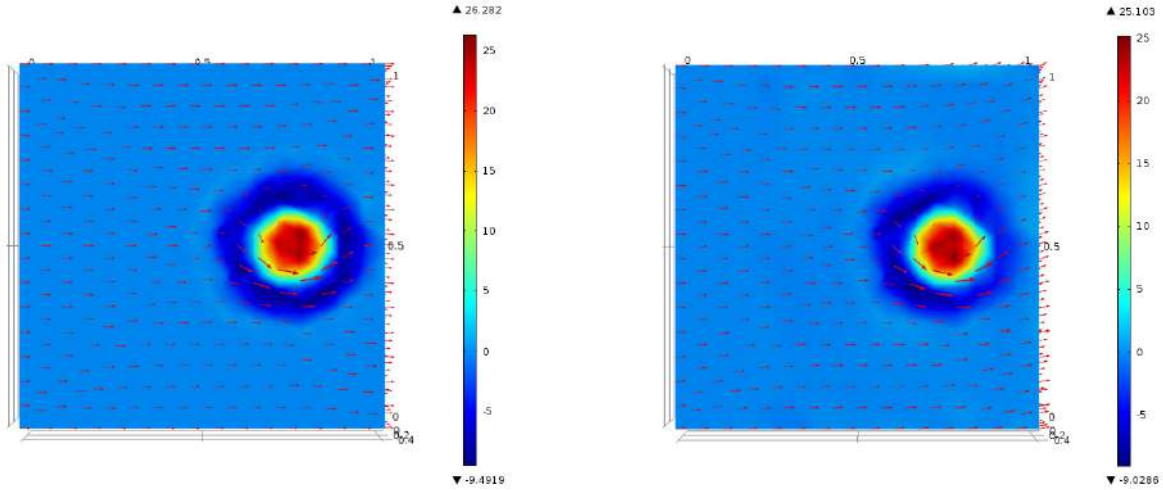

(a) Exact (b) Recovered

Figure 7.2: Velocity and vorticity plots for vortex motion (7.44) under Euler's flow at $t = 0.5$ for $\alpha = \beta = 1$

α	β	Relative L^2 Error	Advection Error
0.01	0.01	2.5e-3	1.6 e-4
1	1	2.8e-3	1.6 e-4
10	10	2.7e-3	1.5 e-4

Table 7.1: Relative L^2 Errors and Advection Errors for different values of α and β

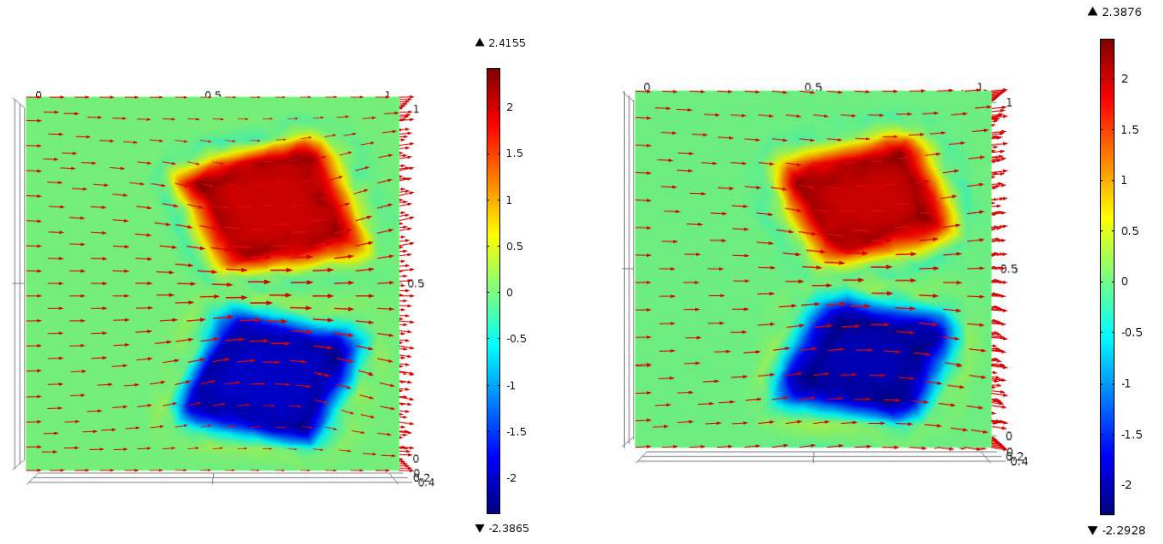

(a) Exact (b) Recovered

Figure 7.3: Velocity and vorticity plots for vortex motion (V2) under Euler's flow at $t = 0.5$ for $\alpha = \beta = 1$

α	β	Relative L^2 Error	Advection Error
0.01	0.01	3.1e-3	1.1 e-4
1	1	3.2e-3	1.1 e-4
10	10	3.2e-3	1.1 e-4

Table 7.2: Relative L^2 Errors and Advection Errors for different values of α and β

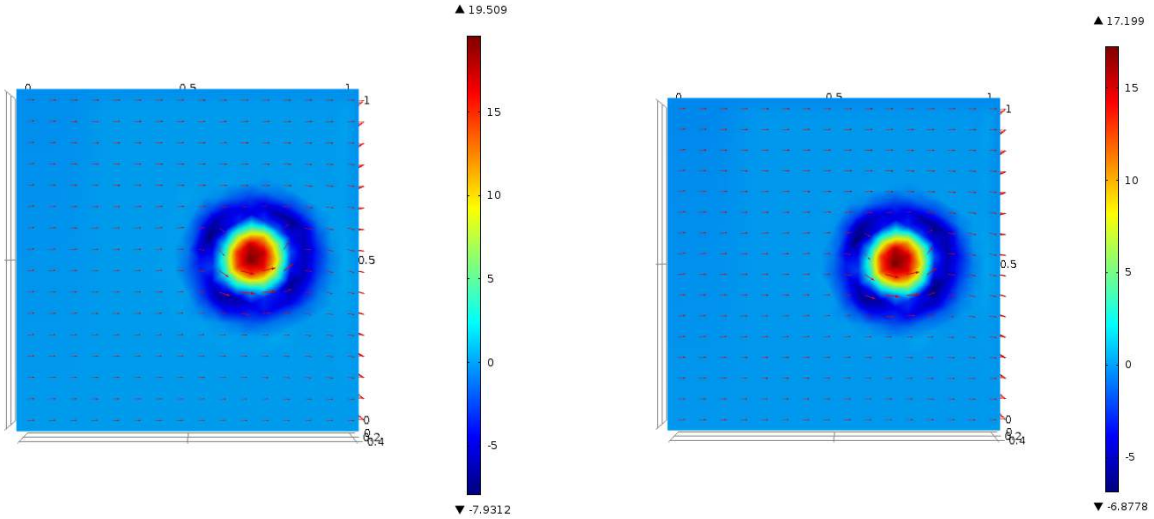

(a) Exact (b) Recovered

Figure 7.4: Velocity and vorticity plots for vortex motion (7.44) under Navier-Stokes flow at $t = 0.5$ for $\alpha = \beta = 1$

the velocity and vorticity plots at time $t = 0.5$. Again the figures show that the translational velocity, which is the constant velocity $(0.5, 0)$, is well captured. Also the vortex movement is well recovered. We note the diffusivity of the vortex structures as is expected in Navier-Stokes flows. Table (7.3) and (7.4) shows the relative L^2 error and the advection error for various values of α and β.

7.6 Formulation 2 - Linearized Flow

We now assume

$$\widetilde{\mathbf{U}} = \mathbf{U}_0 + \mathbf{U}$$

but now $\mathbf{U}_0$ is curl free, incompressible and unknown. Also $\mathbf{U}$ is assumed to be small relative to $\mathbf{U}_0$. This is the Helmholtz decomposition of $\widetilde{\mathbf{U}}$. Since $\mathbf{U}_0$ is unknown, we assume it is smooth and hence we add a regularization term to the functional J given in (P_1). Our aim is

α	β	Relative L^2 Error	Advection Error
0.01	0.01	5.1e-3	2.2 e-4
1	1	5.2e-3	2.2 e-4
10	10	5.1e-3	2.6 e-4

Table 7.3: Relative L^2 Errors and Advection Errors for different values of α and β

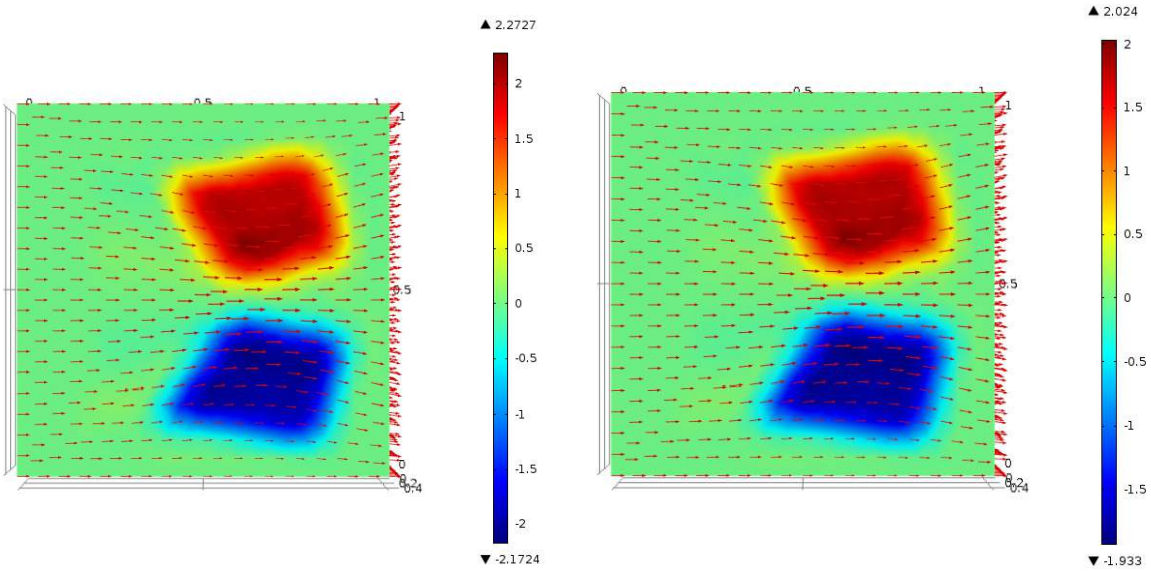

(a) Exact (b) Recovered

Figure 7.5: Velocity and vorticity plots for vortex motion (V2) under Navier-Stokes flow at $t = 0.5$ for $\alpha = \beta = 1$

α	β	Relative L^2 Error	Advection Error
0.01	0.01	4.4e-3	2.7 e-4
1	1	4.1e-3	2.5 e-4
10	10	4.3e-3	2.4 e-4

Table 7.4: Relative L^2 Errors and Advection Errors for different values of α and β

to determine $\mathbf{U}$ and hence the total velocity $\widetilde{\mathbf{U}}$ by minimizing

$$J_1(\psi, \omega_0, g, \mathbf{U}_0) = \frac{1}{2}\int_Q (E_t + \widetilde{\mathbf{U}}.\nabla E)^2 + \frac{\alpha^2}{2}\int_0^T \int_{\partial\Omega} |g|^2 + \frac{\beta^2}{2}\int_\Omega |w_0|^2 + \frac{\gamma^2}{2}\int_\Omega |\nabla \mathbf{U}_0|^2 \quad (7.49)$$

subject to the constraint set (7.8), (7.9) and (7.10).

7.6.1 Optimization using Lagrange Multipliers

Using the weak forms for the vorticity and the streamfunction equations given by (7.62)(or (7.63)) and (7.64) in Section 7.8.1, to determine the optimal solution, the auxiliary functional can be written as

$$\begin{aligned}\widetilde{J}(y, \omega, \phi, \psi, \mathbf{U}_0, g, \omega_0) = J_1 + \int_Q (-\omega y_t + (\mathbf{U}_0 \cdot \nabla\omega)y) + \int_\Omega \omega(T)y(T) - \omega_0 y(0) \\ + \int_Q (\nabla\psi \cdot \nabla\phi - \omega\phi) - \int_0^T \int_{\partial\Omega} g\phi \ (+\frac{1}{Re}\int_Q \nabla\omega \cdot \nabla y)\end{aligned} \quad (7.50)$$

where y is the Lagrange Multiplier corresponding to the first constraint set (7.8) and ϕ is the Lagrange Multiplier corresponding to the second constraint set (7.14). Here $\omega, y \in L^2([0,T]; L^2(\Omega))$ and $\psi, \phi \in L^2([0,T]; H_a^1(\Omega))$ where

$$H_a^1(\Omega) = \{\psi \in H^1(\Omega) : \int_\Omega \psi = 0\}$$

7.6.2 PDE's obtained after minimization of $\widetilde{J}$

Taking the Gateaux derivative of $\widetilde{J}$ in (7.50) wrt $y, \omega, \phi, \psi, g, \omega_0$, the standard optimality conditions [100] are

$$\frac{\partial\widetilde{J}}{\partial y} = 0, \ \frac{\partial\widetilde{J}}{\partial\omega} = 0, \ \frac{\partial\widetilde{J}}{\partial\phi} = 0, \ \frac{\partial\widetilde{J}}{\partial\psi} = 0, \ \frac{\partial\widetilde{J}}{\partial\mathbf{U}_0} = 0, \ \frac{\partial\widetilde{J}}{\partial g} = 0, \ \frac{\partial\widetilde{J}}{\partial\omega_0} = 0 \quad (7.51)$$

The first and second equations in (7.51) gives the vorticity equation and its adjoint

$$\begin{aligned}&\omega_t + \mathbf{U}_0 \cdot \nabla\omega = 0 \ (\frac{1}{Re}\Delta\omega) \\ &\omega(\mathbf{x}, 0) = \omega_0(\mathbf{x}) \\ &\omega = 0, \quad \mathbf{x} \in \partial\Omega_- \ (\partial\Omega)\end{aligned} \quad (7.52)$$

$$\begin{aligned}&y_t + \mathbf{U}_0 \cdot \nabla y = 0 \ (-\frac{1}{Re}\Delta y) \\ &y(\mathbf{x}, T) = 0 \\ &y = 0 \text{ on } \partial\Omega\end{aligned} \quad (7.53)$$

The incompressibility of $\mathbf{U}_0$ is essential in obtaining (7.53). The third and fourth equations in (7.51) gives the equations for the streamfunction and its adjoint

$$\begin{aligned}&-\Delta\psi = \omega, \quad \mathbf{U} = \nabla^\perp\psi \\ &\frac{\partial\psi}{\partial n} = g \\ &\int_\Omega \psi = 0\end{aligned} \quad (7.54)$$

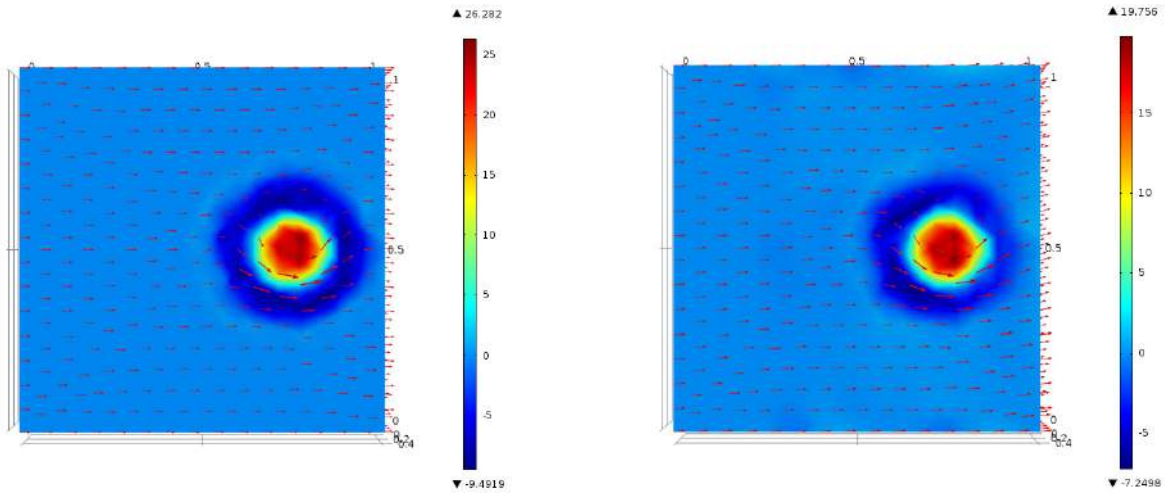

(a) Exact (b) Recovered

Figure 7.6: Velocity and vorticity plots for vortex motion (7.44) under Euler's flow at $t = 0.5$ for $\alpha = \beta = \gamma = 1$

$$\begin{aligned} \Delta\phi &= -\nabla E.\nabla^{\perp} F \\ \frac{\partial \phi}{\partial n} &= -F\frac{\partial E}{\partial t} \\ \int_{\Omega} \phi &= 0 \end{aligned} \tag{7.55}$$

The fifth equation in (7.51) gives the PDE satisfied by $\mathbf{U}_0$ with the boundary conditions

$$\begin{aligned} F\nabla E + y\nabla\omega - \gamma^2 \Delta \mathbf{U}_0 &= 0 \\ \frac{\partial \mathbf{U}_0}{\partial n} &= 0 \end{aligned} \tag{7.56}$$

where $F = E_t + \widetilde{\mathbf{U}} \cdot \nabla E$. The last two equations in (7.51) gives the optimality conditions

$$\alpha^2 g = \phi, \qquad \beta^2 \omega_0 = y(0) \tag{7.57}$$

We again use a similar kind of computational approach as used in Section 7.4.

7.7 Numerical Examples

7.7.1 Advection of vortex 1 and vortex 2 under Euler's flow

The exact flow is given by solving (7.42) with initial vorticity given by (7.44) and (V2) and boundary condition for streamfunction given in Section (7.4.5). Figure (7.6) and (7.7) shows the velocity and vorticity plots at time $t = 0.5$. As in the test cases in Section 7.5.1, the translational velocity is well recovered. Also the vortex structures are well recovered. Table (7.5) and (7.6) shows the relative L^2 error and the advection error for various values of α and β. As in the test cases in Section 7.5.1, the best results are obtained values of α and β in the range of $[0.1, 10]$. For the parameter γ we also use values in the range of $[0.1, 10]$ because higher values of γ lead to over-smoothing of the translational velocity field which is not desirable when we have discontinuous vortices.

α	β	γ	Relative L^2 Error	Advection Error
0.01	0.01	0.01	2.8e-3	1.3 e-4
1	1	1	2.6e-3	1.4 e-4
10	10	10	2.7e-3	1.3 e-4

Table 7.5: Relative L^2 Errors and Advection Errors for different values of α, β and γ

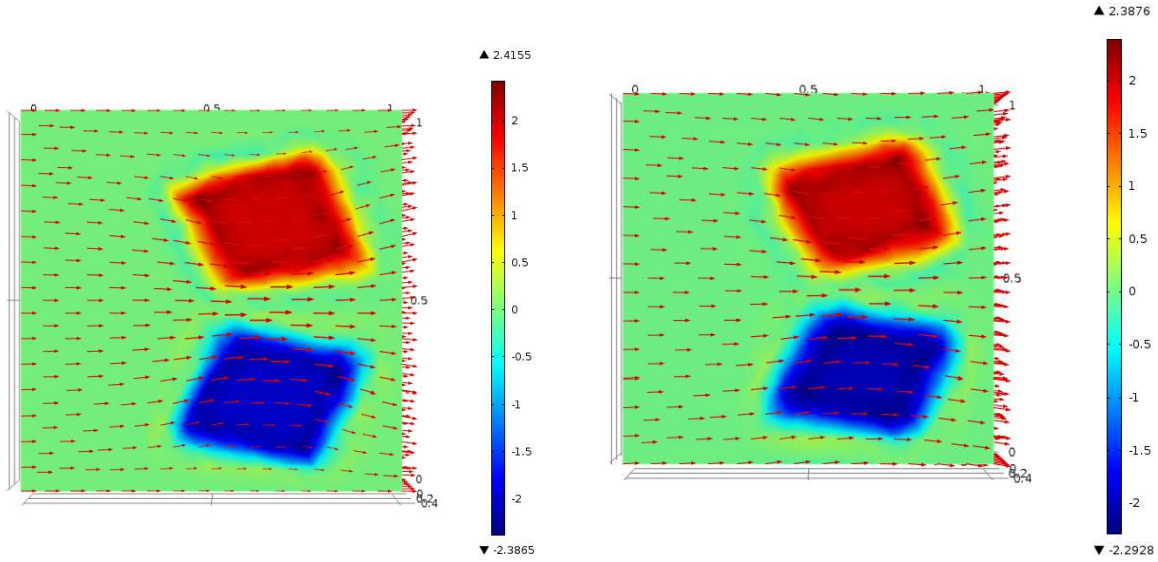

(a) Exact (b) Recovered

Figure 7.7: Velocity and vorticity plots for vortex motion (V2) under Euler's flow at $t = 0.5$ for $\alpha = \beta = \gamma = 1$

α	β	γ	Relative L^2 Error	Advection Error
0.01	0.01	0.01	3.5e-3	1.7 e-4
1	1	1	3.4e-3	1.2 e-4
10	10	10	3.1e-3	1.4 e-4

Table 7.6: Relative L^2 Errors and Advection Errors for different values of α, β and γ

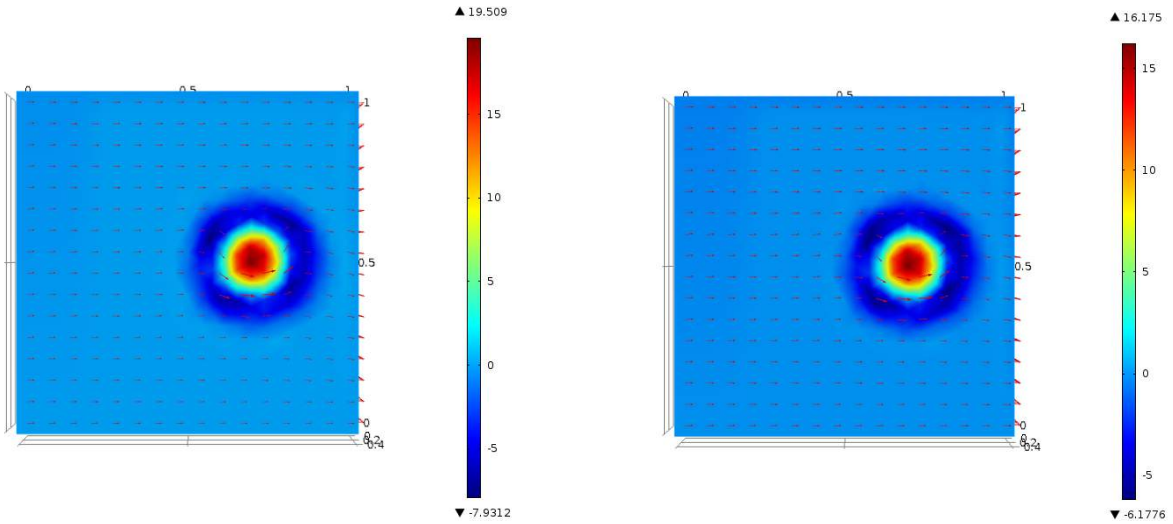

(a) Exact (b) Recovered

Figure 7.8: Velocity and vorticity plots for vortex motion (7.44) under Navier-Stokes flow at $t = 0.5$ for $\alpha = \beta = \gamma = 1$

α	β	γ	Relative L^2 Error	Advection Error
0.01	0.01	0.01	5.4e-3	2.8 e-4
1	1	1	5.3e-3	2.4 e-4
10	10	10	5.6e-3	2.7 e-4

Table 7.7: Relative L^2 Errors and Advection Errors for different values of α, β and γ

7.7.2 Advection of vortex 1 and vortex 2 under Navier-Stokes flow

The exact flow is given by solving (7.43) with initial vorticity given by (7.44) and (V2) and boundary condition for streamfunction given in Section (7.4.5). Figure (7.8) and (7.9) shows the velocity and vorticity plots at time $t = 0.5$. Again the translational velocity is well recovered. Also the diffusive vortex movement is well captured. Table (7.7) and (7.8) shows the relative L^2 error and the advection error for various values of α and β.

7.8 Formulation 3 - Non-Linear Flow

In this case $\widetilde{\mathbf{U}}$ is determined by minimizing

$$J(\psi(\omega_0, g), \omega_0, g) = \frac{1}{2}\int_Q (E_t + \nabla^\perp\psi.\nabla E)^2 + \frac{\alpha^2}{2}\int_0^T\int_{\partial\Omega}|g|^2 + \frac{\beta^2}{2}\int_\Omega|\omega_0|^2 \tag{7.58}$$

α	β	γ	Relative L^2 Error	Advection Error
0.01	0.01	0.01	4.3e-3	2.2 e-4
1	1	1	4.4e-3	2.8 e-4
10	10	10	4.6e-3	2.5 e-4

Table 7.8: Relative L^2 Errors and Advection Errors for different values of α, β and γ

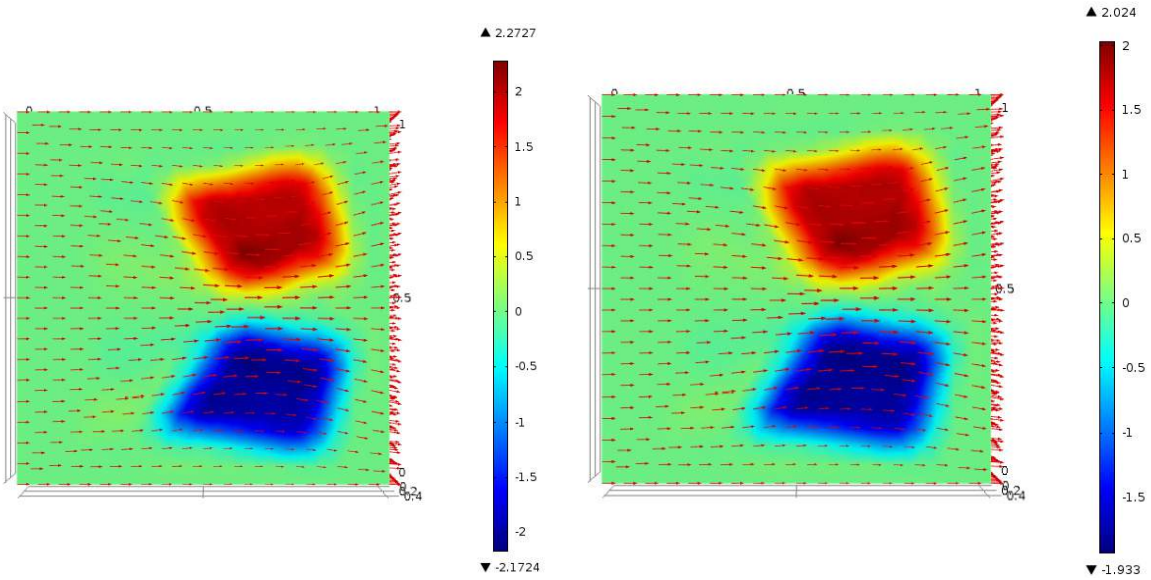

(a) Exact (b) Recovered

Figure 7.9: Velocity and vorticity plots for vortex motion (V2) under Navier-Stokes flow at $t = 0.5$ for $\alpha = \beta = \gamma = 1$

subject to

$$\begin{aligned} &\omega_t + \widetilde{\mathbf{U}} \cdot \nabla\omega = 0 \ (\frac{1}{Re}\Delta\omega), \quad (\mathbf{x}, t) \in \Omega \times (0, T] \\ &\omega(\mathbf{x}, 0) = \omega_0(\mathbf{x}), \quad \mathbf{x} \in \Omega \\ &\omega = 0, \quad \mathbf{x} \in \partial\Omega_- \ (\partial\Omega \text{ for Navier-Stokes}) \end{aligned} \tag{7.59}$$

$$\begin{aligned} \Delta\psi &= \omega, \quad \text{in } \Omega \\ \frac{\partial\psi}{\partial n} &= g, \quad \text{on } \partial\Omega \end{aligned} \tag{7.60}$$

$$\begin{aligned} \widetilde{\mathbf{U}} &= \nabla^{\perp}\psi \\ \omega &= \nabla \times \widetilde{\mathbf{U}} \end{aligned} \tag{7.61}$$

7.8.1 Optimization using Lagrange Multipliers

We first write down the weak forms of (7.59) and (7.60). Multiplying (7.59) with a test function $y \in H^1([0, T]; L^2(\Omega))$, integrating by parts with respect to t and incorporating initial conditions for ω, we get

$$\int_Q (-\omega y_t + (\widetilde{\mathbf{U}} \cdot \nabla\omega)y) + \int_\Omega \omega(T)y(T) - \omega_0 y(0) = 0. \tag{7.62}$$

If we consider the Navier-Stokes equation then performing an integration by parts over Ω and using boundary conditions on ω, we get

$$\int_Q (-\omega y_t + (\widetilde{\mathbf{U}} \cdot \nabla\omega)y) + \int_\Omega \omega(T)y(T) - \omega_0 y(0) + \frac{1}{Re}\int_Q \nabla\omega \cdot \nabla y = 0. \tag{7.63}$$

Multiplying (7.9) with a test function $\phi \in L^2([0, T]; H_a^1(\Omega))$, integrating by parts over Ω, and using boundary conditions on ψ we get

$$\int_Q (\nabla\psi \cdot \nabla\phi - \omega\phi) - \int_0^T \int_{\partial\Omega} g\phi = 0. \tag{7.64}$$

Hence to determine the optimal solution, the auxiliary functional can be written as

$$\begin{aligned}\widetilde{J}(y,\omega,\phi,\psi,g,\omega_0) = J + \int_Q (-\omega y_t + (\widetilde{\mathbf{U}}\cdot\nabla\omega)y) + \int_\Omega \omega(T)y(T) - \omega_0 y(0) \\ + \int_Q (\nabla\psi\cdot\nabla\phi - \omega\phi) - \int_0^T \int_{\partial\Omega} g\phi \ (+\frac{1}{Re}\int_Q \nabla\omega\cdot\nabla y)\end{aligned} \tag{7.65}$$

where y is the Lagrange Multiplier corresponding to the first constraint set (7.8) and ϕ is the Lagrange Multiplier corresponding to the second constraint set (7.14). Here $\omega, y \in L^2([0,T];L^2(\Omega))$ and $\psi,\phi \in L^2([0,T];H_a^1(\Omega))$ where

$$H_a^1(\Omega) = \{\psi \in H^1(\Omega) : \int_\Omega \psi = 0\}$$

7.8.2 PDE's obtained after minimization of $\widetilde{J}$

Taking the Gateaux derivative of $\widetilde{J}$ in (7.65) wrt $y,\omega,\phi,\psi,g,\omega_0$, the standard optimality conditions [100] are

$$\frac{\partial\widetilde{J}}{\partial y}=0,\ \frac{\partial\widetilde{J}}{\partial\omega}=0,\ \frac{\partial\widetilde{J}}{\partial\phi}=0,\ \frac{\partial\widetilde{J}}{\partial\psi}=0,\ \frac{\partial\widetilde{J}}{\partial g}=0,\ \frac{\partial\widetilde{J}}{\partial\omega_0}=0 \tag{7.66}$$

The first and second equations in (7.66) gives the vorticity equation and its adjoint

$$\begin{aligned}&\omega_t + \widetilde{\mathbf{U}}\cdot\nabla\omega = 0 \ (\frac{1}{Re}\Delta\omega)\\ &\omega(\mathbf{x},0) = \omega_0(\mathbf{x})\\ &\omega = 0, \quad \mathbf{x}\in\partial\Omega_- \ (\partial\Omega)\end{aligned} \tag{7.67}$$

$$\begin{aligned}&y_t + \widetilde{\mathbf{U}}\cdot\nabla y = 0 \ (-\frac{1}{Re}\Delta y)\\ &y(\mathbf{x},T) = 0\\ &y = 0 \text{ on } \partial\Omega\end{aligned} \tag{7.68}$$

The third and fourth equations in (7.66) gives the equations for the streamfunction and its adjoint

$$\begin{aligned}&-\Delta\psi = \omega, \quad \widetilde{\mathbf{U}} = \nabla^\perp\psi\\ &\frac{\partial\psi}{\partial n} = g\end{aligned} \tag{7.69}$$

$$\begin{aligned}&\Delta\phi = -\nabla E.\nabla^\perp F\\ &\frac{\partial\phi}{\partial n} = -F\frac{\partial E}{\partial t}\end{aligned} \tag{7.70}$$

where $F = E_t + \widetilde{\mathbf{U}}\cdot\nabla E$. The fifth and sixth equations in (7.66) gives the optimality conditions

$$\alpha^2 g = \phi, \qquad \beta^2\omega_0 = y(0) \tag{7.71}$$

7.9 Numerical Examples

7.9.1 Advection of vortex 1 and vortex 2 under Euler's flow

The exact flow is given by solving (7.42) with initial vorticity given by (7.44) and (V2) and boundary condition for streamfunction given in Section (7.4.5). Figures (7.10) and (7.11) shows

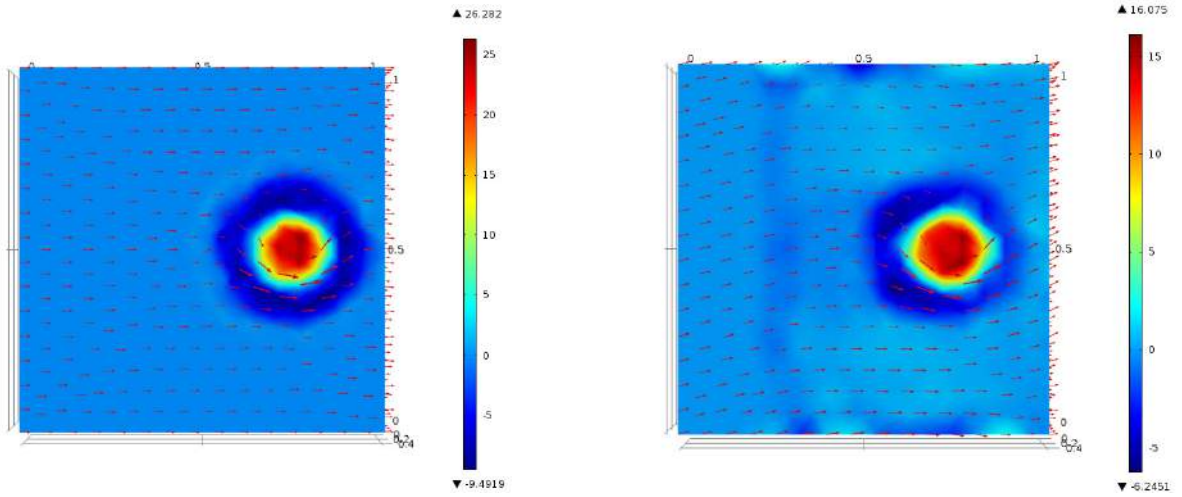

(a) Exact (b) Recovered

Figure 7.10: Velocity and vorticity plots for vortex motion (7.44) under Euler's flow at $t = 0.5$ for $\alpha = \beta = 1$

α	β	Relative L^2 Error	Advection Error
0.01	0.01	0.21	3.21 e-2
0.1	0.01	0.24	3.22 e-2
1	1	0.23	3.26 e-2

Table 7.9: Relative L^2 Errors and Advection Errors for different values of α and β

the velocity and vorticity plots at time $t = 0.5$. Unlike the test cases in Section 7.5.1 and 7.7.1, we see that the translational velocity is not well recovered. Also there is a lot of vortex shredding in Figure (7.10). It diffuses out the vortex even for Euler's flow. In Figure (7.11) we note the vortex patches get diffused to a high extent. Near the red vortex patch there are light blue patches and vice-versa for the blue vortex patch which means vortex shredding takes place. The bad recovery of the vortex patches could be due to lack of non-uniqueness of solution to the vorticity equation (7.67). Table (7.9) and (7.10) shows the relative L^2 error and the advection error for various values of α and β. As in the test cases in Section 7.5.1, the best results are obtained values of α and β in the range of $[0.1, 10]$.

7.9.2 Advection of vortex 1 and vortex 2 under Navier-Stokes flow

The exact flow is given by solving (7.43) with initial vorticity given by (7.44) and (V2) and boundary condition for streamfunction given in Section (7.4.5). Figure (7.12) and (7.13) shows the velocity and vorticity plots at time $t = 0.5$. As in the test cases in Section 7.9.1, we see that the translational velocity and vorticity is not well recovered. There is a lot of vortex shredding and over-diffusivity. Table (7.11) and (7.12) shows the relative L^2 error and the advection error

α	β	Relative L^2 Error	Advection Error
0.01	0.01	0.35	1.64 e-2
1	1	0.37	1.62 e-2
10	10	0.35	1.61 e-2

Table 7.10: Relative L^2 Errors and Advection Errors for different values of α and β

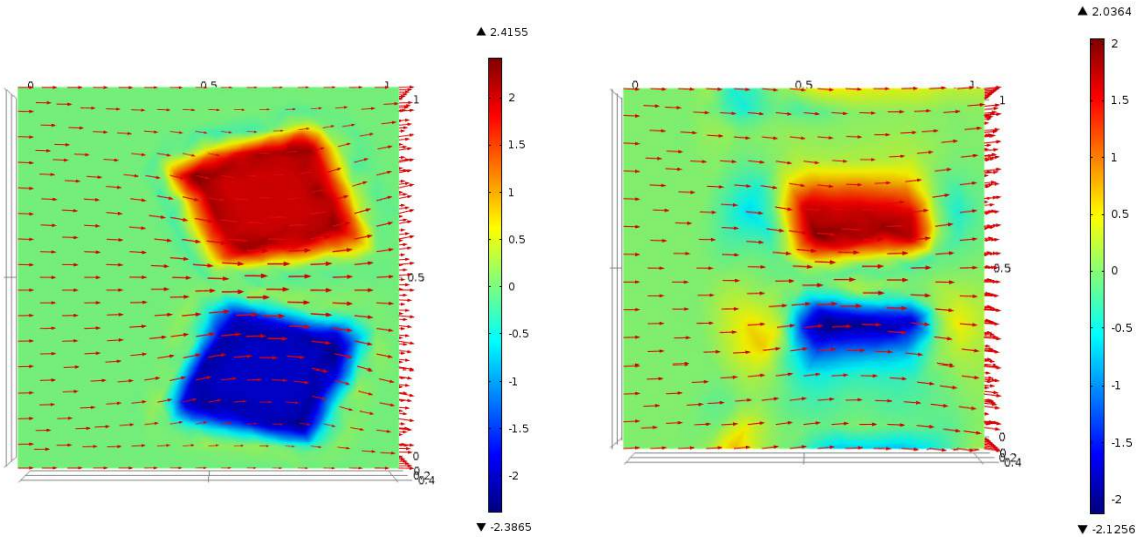

(a) Exact (b) Recovered

Figure 7.11: Velocity and vorticity plots for vortex motion (V2) under Euler's flow at $t = 0.5$ for $\alpha = \beta = 1$

α	β	Relative L^2 Error	Advection Error
0.01	0.01	0.51	6.6 e-2
1	1	0.55	6.1 e-2
10	10	0.52	6.7 e-2

Table 7.11: Relative L^2 Errors and Advection Errors for different values of α and β

for various values of α and β.

7.10 Conclusions

To determine optical velocity for vortex based flows, we have assumed that the underlying fluid satisfies Euler or Navier-Stokes equations. The vorticity-streamfunction formulation for the Euler and Navier-Stokes equations were introduced and the Helmholtz decomposition of the velocity field was used to segregate the translational and rotational part of the velocity field. To determine the velocity and vorticity field a variational approach to minimize a functional, which penalized the tracking or advection error of the scalar image field and the initial vorticity and boundary condition for the streamfunction, was used. For the linearized case we have shown the existence of a unique velocity field. We also exploited the advantages of the discontinuous Galerkin finite elements for the vorticity equation (in case of Euler's flow) to capture discontinuous vortices effectively. Two types of vortex movement under Euler and Navier-Stokes flows were investigated and it was observed that in the case where we assumed

α	β	Relative L^2 Error	Advection Error
0.01	0.01	0.60	7.2 e-2
1	1	0.64	7.4 e-2
10	10	0.65	7.1 e-2

Table 7.12: Relative L^2 Errors and Advection Errors for different values of α and β

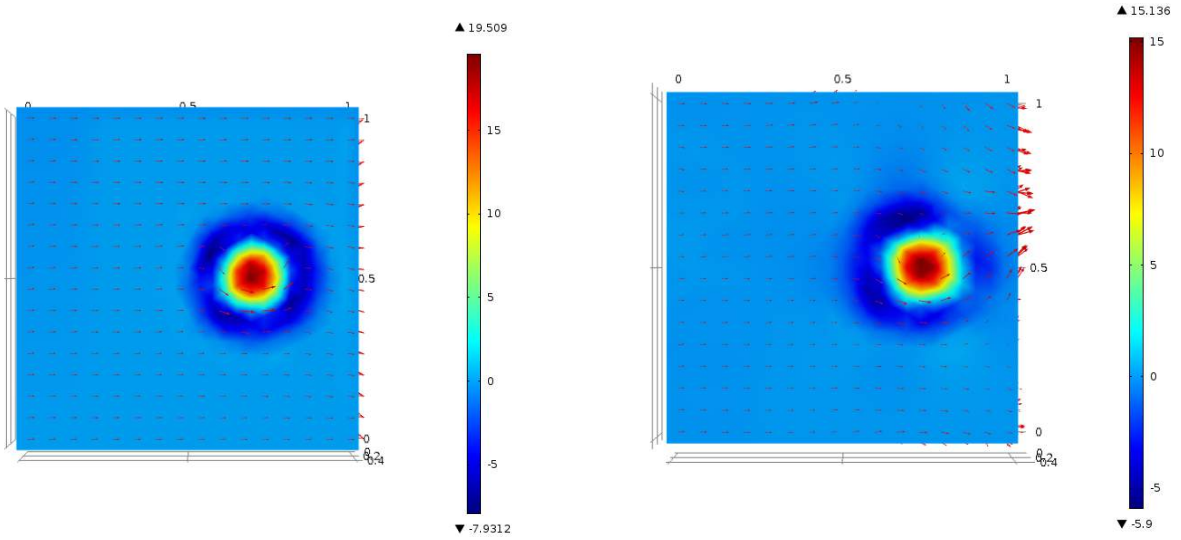

(a) Exact (b) Recovered

Figure 7.12: Velocity and vorticity plots for vortex motion (7.44) under Navier-Stokes flow at $t = 0.5$ for $\alpha = \beta = 1$

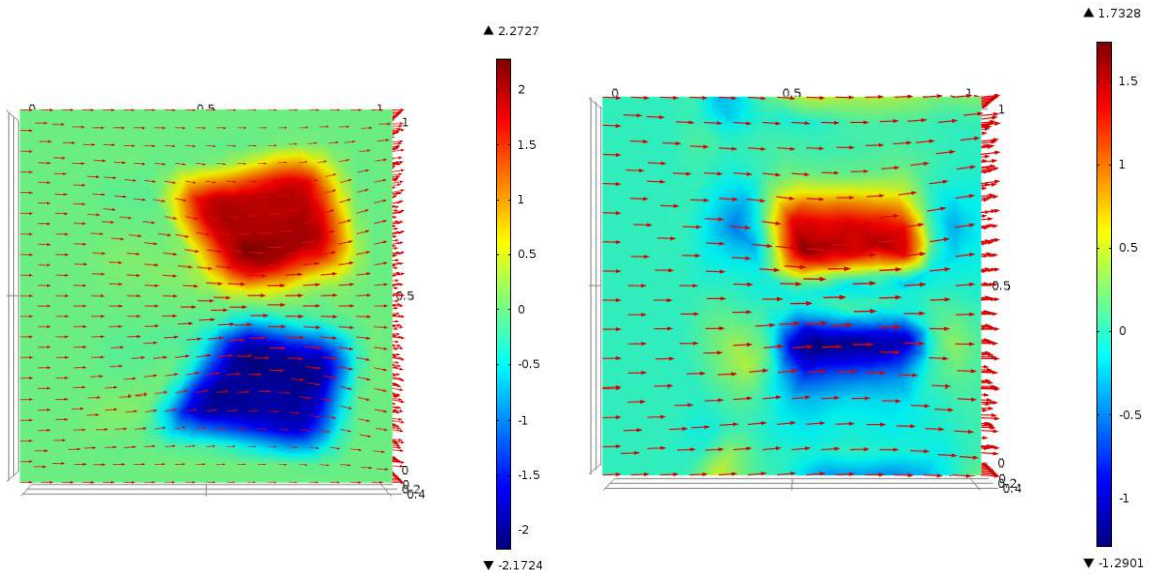

(a) Exact (b) Recovered

Figure 7.13: Velocity and vorticity plots for vortex motion (V2) under Navier-Stokes flow at $t = 0.5$ for $\alpha = \beta = 1$

Helmholtz decomposition of the velocity vector field, significantly good results were obtained even for higher Reynolds number flows. In the case where there was no assumption on the velocity field, occurrence of vortex shredding and high diffusion took place. A reason for this could be the non-uniqueness of solutions to the vorticity equation which is itself an interesting theoretical problem. The authors plan to address this in future. It also suggests that to capture vortex structures, boundary information of the velocity or the initial vorticity is needed or else rotational dynamics should be introduced into the model. Further work will be to use other penalties in our objective functional J and try to capture other types of non-linear flows.

Chapter 8

Numerical Inversion of Circular and Elliptic Radon Transforms

8.1 Introduction

[1] The inversion of circular Radon transforms has been extensively studied by several authors [1, 2, 7, 72, 73, 31, 9, 30, 33, 32, 34, 87, 70, 10, 71], and to a lesser extent, that of elliptical Radon transforms [53, 83, 105, 3, 62, 36]. All these papers deal with full data in the radial direction. In some imaging problems, full data in the radial direction is not available, as is the case of imaging the surrounding region of a bone. To this end, Ambartsoumian, Gouia-Zarrad and Lewis in [5] found explicit inversion formulas for the circular Radon transform with circular acquisition geometry (one of the most widely used ways of collecting data) when half the data in the radial variable is available. These results were recently generalized by Ambartsoumian and Krishnan for a class of elliptical and circular Radon transforms in [6]. The inversion formulas in these papers are given for three cases: support of the function is inside, outside and on both sides of the acquisition circle. The case when the support is inside the circle of acquisition is of importance in ultrasound reflectivity imaging, thermoacoustic and photoacoustic tomography, and non-destructive testing. When the support is outside and on both sides of the acquisition circle, the inversion formulas are applicable in intravascular and radar imaging, respectively. Given the importance of these inversion formulas in several imaging modalities, efficient numerical inversion is of great interest. The main contribution of this paper is a novel implementation of the inversion formulas for a class of circular and elliptical Radon transforms with radially partial data obtained in these papers. The inversion formulas given in [5, 6] were based on an inversion strategy due to Cormack [28] that involved Fourier series techniques. As shown in these papers, the n^{th} Fourier coefficient of the circular (elliptical) Radon transform data is related to the n^{th} Fourier coefficient of the unknown function by a Volterra-type integral equation of the first kind with a weakly singular kernel. This can be transformed to a Volterra-type integral equation of the second kind in which the singularity is removed [104]. It is well known that such an integral equation has a unique solution and this can be obtained by the Picard's process of successive approximations, leading to an exact inversion formula given by a infinite series of iterated kernels; see [104]. In this chapter, we numerically invert Volterra-type integral equation of the first kind adopting a numerical method given in [107] (see also [77]) and combine it with a truncated singular value decomposition to recover the Fourier coefficients of the unknown function from the circular or elliptical Radon transform data. The same method can also be implemented for numerical inversion of Volterra-type integral equation of the second kind proved in the papers [5, 6], but the numerical inversion is less accurate (see Remark 8.3.1). The numerical implementation of the exact inversion formula

[1]The contents of the chapter are in the paper [86] accepted by JMIV, Springer

for the Volterra integral equation of the second kind involving an infinite series of iterated kernels is very unstable and implementing them is still an open problem. To the best of our knowledge, ours is the first successful numerical inversion of circular and elliptical Radon transforms for the circular geometry of acquisition with radially partial data, the theoretical results of which, as already mentioned, were presented in [5] and [6].

8.2 Theoretical background

We consider two generalized Radon transforms in the plane: (a) Circular Radon transform and (b) Elliptical Radon transform.

Circular Radon transform

Let $\partial B(0,R)$ denote the circle of radius R centered at $(0,0)$ and parametrized by

$$\gamma(\phi) = (R\cos\phi, R\sin\phi) : \phi \in [0, 2\pi].$$

Let $\rho > 0$ and define the circle of radius ρ centered at $\gamma(\phi)$:

$$C(\rho,\phi) = \{x \in \mathbb{R}^2 : |x - \gamma(\phi)| = \rho\}$$

Let (r,θ) denote the standard polar coordinates on the plane and let $f(r,\theta)$ be a compactly supported function in $\mathbb{R}^2$. The circular Radon transform of f over the circle $C(\rho,\phi)$ is defined as

$$g^C(\rho,\phi) = R^C f(\rho,\phi) = \int\limits_{C(\rho,\phi)} f(r,\theta)\mathrm{d}s.$$

Here $\mathrm{d}s$ is the arc-length parametrization on the circle $C(\rho,\phi)$. See Figure 8.1a.

Elliptical Radon transform

We consider $\partial B(0,R)$ as before and let $\alpha \in (0,\pi/2)$ be a fixed angle. The ellipses of interest to us are the ones with their foci on $\partial B(0,R)$ separated by the polar angle 2α. Define $a = R\sin\alpha$ and $b = R\cos\alpha$. Given (ρ,ϕ), we consider the foci locations to be $\gamma_{f_1}(\phi) = (R\cos(\phi-\alpha), R\sin(\phi-\alpha))$ and $\gamma_{f_2}(\phi) = (R\cos(\phi+\alpha), R\sin(\phi+\alpha))$. Now consider the ellipse

$$E(\rho,\phi) = \{x \in \mathbb{R}^2 : |x - \gamma_{f_1}(\phi)| + |x - \gamma_{f_2}(\phi)| = 2\sqrt{\rho^2 + a^2}\}.$$

The elliptical Radon transform of f over $E(\rho,\phi)$ is defined as

$$g^E(\rho,\phi) = R^E f(\rho,\phi) = \int\limits_{E(\rho,\phi)} f(r,\theta)\mathrm{d}s,$$

where $\mathrm{d}s$ is the arc-length parametrization on $E(\rho,\phi)$. See Figure 8.1b.

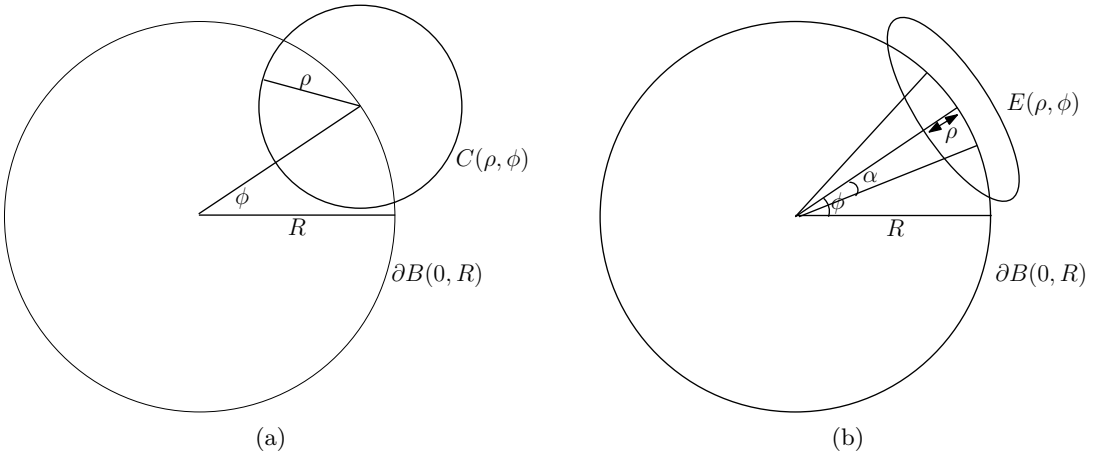

Figure 8.1: Circular and elliptical Radon transform set-up

The transforms R^C and R^E with radially partial data were considered in [5, 6] and explicit inversion formulas were given there, which we now recall. The proof of each of the results below involves a Volterra-type integral equation of the first kind with a weakly singular kernel. As already mentioned in the introduction, the explicit inversion formulas given in [5, 6] involved transforming such an integral equation to one of the second kind with the singularity removed. The inversion formulas are given as an infinite series involving iterated kernels. Since we perform numerical inversion of Volterra-type integral equations of the first kind, we limit ourselves to recalling only them here. However, see Remark 8.3.1.

We expand $f(r,\theta)$, $g^C(\rho,\phi)$ and $g^E(\rho,\phi)$ into a Fourier series:

$$f(r,\theta)=\sum_{n=-\infty}^{\infty} f_n(r)e^{\mathrm{i}n\theta}, g^C(\rho,\phi)=\sum_{n=-\infty}^{\infty} g_n^C(\rho)e^{\mathrm{i}n\phi}, g^E(\rho,\phi)=\sum_{n=-\infty}^{\infty} g_n^E(\rho)e^{\mathrm{i}n\phi}$$

In the following results, f_n is related to g_n^C or g_n^E through a Volterra-type integral equation of the first kind. We will use the superscripts *Int*, *Ext* or *Both* to denote the cases when the support of the function is an annular region in the interior, exterior or on both sides of the circle $\partial B(0,R)$, respectively.

Theorem 8.2.1 (Functions supported in an annulus interior to $\partial B(0,R)$)**.** *[5, 6]*

1. *[5, Thm. 1](Circular transform) Let $0<\varepsilon<R$ and $f(r,\theta)$ in polar coordinates be an unknown continuous function in polar coordinates supported inside the annular region $A(\epsilon,R)=\{(r,\theta): r\in(\epsilon,R),\theta\in[0,2\pi]\}$. If $R^Cf(\rho,\phi)$ is known for $\phi\in[0,2\pi]$ and $\rho\in[0,R-\epsilon]$, then $f(r,\theta)$ can be uniquely recovered in $A(\epsilon,R)$.*

2. *[6, Thm. 3.1](Elliptical transform) Let $f(r,\theta)$ be a continuous function supported inside the annulus $A(\varepsilon,b)$. Suppose $R^Ef(\rho,\phi)$ is known for all $\phi\in[0,2\pi]$ and $\rho\in(0,b-\varepsilon)$, then $f(r,\theta)$ can be uniquely recovered.*

In the above theorems, the relation between the n^{th} Fourier coefficient of the function f and the n^{th} Fourier coefficient of the circular Radon transform $g_n^{\mathrm{C,Int}}$ and the elliptical Radon transform $g_n^{\mathrm{E,Int}}$ involve the Volterra-type integrals which are given below.

1. Circular case, see [5]

$$g_n^{\mathrm{C,Int}}(\rho)=\int_0^{\rho}\frac{K_n(\rho,u)F_n(u)}{\sqrt{\rho-u}}\mathrm{d}u, \tag{8.1}$$

where

$$F_n(u) = f_n(R-u), \qquad T_n(x) = \cos(n \arccos(x))$$
$$K_n(\rho,u) = \frac{4\rho(R-u)T_n\left[\frac{(R-u)^2+R^2-\rho^2}{2R(R-u)}\right]}{\sqrt{(u+\rho)(2R+\rho-u)(2R-\rho-u)}}. \tag{8.2}$$

2. Elliptical case, see [6]

$$g_n^{\mathrm{E,Int}}(\rho) = \int_0^\rho \frac{K_n(\rho,u)F_n(u)}{\sqrt{\rho-u}}\mathrm{d}u, \tag{8.3}$$

where

$$F_n(u) = f_n(b-u)$$
$$K_n(\rho,u) = \frac{\widetilde{K}_n(\rho,b-u)\sqrt{\rho-u}}{\sqrt{a^2+b\rho-\sqrt{R^2\rho^2+a^2(R^2-(b-u)^2)}}} \tag{8.4}$$
$$\widetilde{K}_n(\rho,r) = \frac{2arT_n\left(\frac{b(\rho^2+a^2)-\rho\sqrt{R^2\rho^2+a^2(R^2-r^2)}}{a^2r}\right)}{\sqrt{a^2+(\sqrt{R^2\rho^2+a^2(R^2-r^2)}-b\rho)}}\times$$
$$\frac{\sqrt{2R^2\rho^2+a^2(R^2-r^2)-2b\rho\sqrt{R^2\rho^2+a^2(R^2-r^2)}}}{\sqrt{R^2\rho^2+a^2(R^2-r^2)}}. \tag{8.5}$$

Theorem 8.2.2 (Functions supported in an annulus exterior to $\partial B(0,R)$)**.** *[5, Thm. 6] (Circular transform) Let $f(r,\theta)$ be a continuous function supported inside the annulus centered at 0: $A(R,3R) = \{(r,\theta) : r \in (R,3R), \theta \in [0,2\pi]\}$. If $R^C f(\rho,\phi)$ is known for $\phi \in [0,2\pi]$ and $\rho \in [0,R_1]$, where $0 < R_1 < 2R$ then $f(r,\theta)$ can be uniquely recovered in $A(R,R_1)$.*

In the above theorem, the relation between the n^{th} Fourier coefficient of the circular Radon transform $g_n^{\mathrm{C,Ext}}$ and the n^{th} Fourier coefficient of the function f is given by [5]

$$g_n^{\mathrm{C,Ext}}(\rho) = \int_0^\rho \frac{K_n(\rho,u)F_n(u)}{\sqrt{\rho-u}}\mathrm{d}u, \tag{8.6}$$

where

$$F_n(u) = f_n(R+u)$$
$$K_n(\rho,u) = \frac{4\rho(R+u)T_n\left[\frac{(R+u)^2+R^2-\rho^2}{2R(R+u)}\right]}{\sqrt{(u+\rho)(2R+\rho+u)(2R+u-\rho)}}. \tag{8.7}$$

Theorem 8.2.3 (Functions with support on both sides of $\partial B(0,R)$)**.** *[6]*

1. *[6, Thm. 3.3](Circular transform) Let $f(r,\theta)$ be a continuous function supported inside the disc $D(0,R_2)$ with $R_2 > 2R$. Suppose $R^C(\rho,\phi)$ is known for all $\phi \in [0,2\pi]$ and $\rho \in [R_2-R, R_2+R]$, then $f(r,\theta)$ can be uniquely recovered in the annulus $A(R_1,R_2)$ where $R_1 = R_2 - 2R$.*

2. *[6, Thm. 3.4](Elliptical Radon transform) Let $f(r,\theta)$ be a continuous function supported inside the disc $D(0,R_2)$ with $R_2 > 2b$. Suppose $R^E(\rho,\phi)$ is known for all $\phi \in [0,2\pi]$ and $\rho \in [R_2-b, R_2+b]$, then $f(r,\theta)$ can be uniquely recovered in $A(R_1,R_2)$ where $R_1 = R_2-2b$.*

In the above theorems, the relation between the n^{th} Fourier coefficient of the function f and the n^{th} Fourier coefficient of the circular Radon transform $g_n^{\text{C,Both}}$ and the elliptical Radon transform $g_n^{\text{E,Both}}$ are given below.

1. Circular case, see [6]

$$g_n^{\text{C,Both}}(R_2+R-\rho)=\int_0^{\rho}\frac{K_n(\rho,u)F_n(u)}{\sqrt{\rho-u}}\mathrm{d}u, \tag{8.8}$$

where

$$\begin{aligned}F_n(u)&=f_n(R_2-u)\\ K_n(\rho,u)&=\frac{4(R_2+R-\rho)(R_2-u)\,T_n\left(\frac{(R_2-u)^2+R^2-(R_2+R-\rho)^2}{2(R_2-u)R}\right)}{\sqrt{(\rho-u)(2R_2-\rho-u)(2R+u-\rho)(2R+2R_2-\rho-u)}}.\end{aligned} \tag{8.9}$$

2. Elliptical case, see [6]

$$g_n^{\text{E,Both}}(R_2+b-\rho)=\int_0^{\rho}\frac{K_n(\rho,u)F_n(u)}{\sqrt{\rho-u}}\mathrm{d}u, \tag{8.10}$$

where

$$\begin{aligned}F_n(u)&=f_n(R_2-u)\\ K_n(\rho,u)&=\frac{\widetilde{K}_n(R_2+b-\rho,R_2-u)\sqrt{\rho-u}}{\sqrt{a^2+b(R_2+b-\rho)-\sqrt{R^2(R_2+b-\rho)^2+a^2(R^2-(R_2-u)^2)}}}\end{aligned} \tag{8.11}$$

$$\begin{aligned}\widetilde{K}_n(\rho,r)=&\frac{2arT_n\left(\frac{b(\rho^2+a^2)-\rho\sqrt{R^2\rho^2+a^2(R^2-r^2)}}{a^2r}\right)}{\sqrt{a^2+(\sqrt{R^2\rho^2+a^2(R^2-r^2)}-b\rho)}}\times\\ &\frac{\sqrt{2R^2\rho^2+a^2(R^2-r^2)-2b\rho\sqrt{R^2\rho^2+a^2(R^2-r^2)}}}{\sqrt{R^2\rho^2+a^2(R^2-r^2)}}.\end{aligned} \tag{8.12}$$

8.3 Numerical Algorithm

In this section, we describe the numerical scheme used to invert the integral equations listed in the previous sections.

8.3.1 Fourier coefficients of the circular and elliptical Radon data in the angular variable

Since the functions are real, for reasons of computational efficiency, we compute the modified discrete fast Fourier transform (FFT) of $g^C(\rho,\phi)$ in ϕ for a fixed $\rho\in[\varepsilon,1-\varepsilon]$ as follows [79]. The procedure for g^E is very similar.

1. Let N be even and $\{\phi_1,\phi_2,\cdots,\phi_N\}$ be a discretization of ϕ. We break the array $g^C(\rho,\phi_k)$ for $1\le k\le N$ into two equal length arrays, A for the odd numbered k and B for the even numbered k. In other words, we let $A=\{g^C(\rho,\phi_{2j-1})\}$ and $B=\{g^C(\rho,\phi_{2j})\}$ for $j=1,2,\cdots,N/2$.

2. We then create a complex array $h_\rho^c(j)=A(j)+\mathrm{i}B(j),\quad j=1,2,\cdots,N/2$.

3. Next we perform a discrete FFT on h_ρ^c to get $\widehat{h_\rho^c}(n), \quad n = 1, 2, \cdots, N/2$.

4. The Fourier series of g^C in the ϕ variable is then given by

$$g_n^C(\rho) = \begin{cases} \frac{1}{2}\Big\{ \left(\widehat{h_\rho^c}(n) + \overline{\widehat{h_\rho^c}(\frac{N}{2} - n + 2)}\right) \\ -\mathrm{i}\left(\widehat{h_\rho^c}(n) - \overline{\widehat{h_\rho^c}(\frac{N}{2} - n + 2)}\right) \cdot e^{\frac{2\pi i(n-1)}{N}} \Big\}, \text{for } n = 1, \cdots, \frac{N}{2} + 1 \\ \widehat{h_\rho^c}(N - n + 2), n = \frac{N}{2} + 2, \cdots, N. \end{cases}$$

8.3.2 Trapezoidal product integration method [107]

The next step is to solve the integral equation of the form

$$g_n(\rho) = \int_0^\rho \frac{F_n(u)K_n(\rho, u)}{\sqrt{\rho - u}} \mathrm{d}u, \tag{8.13}$$

Under some assumptions on the kernel K_n and the function g_n, it is known that the integral equation (8.13) has a unique continuous solution F_n.

Theorem 8.3.1 (Existence and uniqueness of solution)**.** *[106] The integral equation (8.13) has a unique continuous solution $F_n(t)$ for $t \in [0, R]$ under the following assumptions:*

1. *The functions*
$$K_n(t, u) \text{ and } \frac{\partial}{\partial t} K_n(t, u)$$
are continuous $0 \le u \le t \le R$,

2. *$K_n(t, t) \neq 0$ for all $t \in [0, R]$,*

3. *The function*
$$G_n(t) = \frac{\partial}{\partial t} \int_0^t \frac{g_n(s)}{(t - s)^{1/2}} \mathrm{d}s$$
is continuous for $t \in [0, R]$.

Under the assumptions of the theorem and using the method of kernel transformation [106, §50], one can transform Volterra equation of the first kind to Volterra equation of the second kind which has a unique solution (see [106, §3]). This derivation was used in the results of [5, 6] to provide analytical inversion formulas for a class of circular and elliptical Radon transforms with radially partial data. Such an exact inversion formula, as it turns out, is numerically unstable. Therefore, we approach the numerical inversion problem by solving (8.13) directly. We use the so-called trapezoidal product integration method proposed in [107]; see also [77]. For the sake of completeness, we briefly sketch this method below.

Rewrite (8.13) as

$$\widetilde{g}_n(\rho) = \int_0^\rho \frac{k_n(\rho, u)}{\sqrt{\rho - u}} F_n(u) \mathrm{d}u \tag{8.14}$$

where

$$k_n(\rho, u) = \frac{K_n(\rho, u)}{K_n(\rho, \rho)}, \qquad \widetilde{g}_n(\rho) = \frac{g_n(\rho)}{K_n(\rho, \rho)}.$$

Let M be a positive even integer and $\rho_l = lh, l = 0, \cdots, M$ and $h = \frac{R - \epsilon}{M}$ be a discretization of $[0, R - \epsilon]$. From (8.14) we have

$$\widetilde{g}_n(\rho_i) = \sum_{k=1}^{i} \int_{\rho_{k-1}}^{\rho_k} \frac{k_n(\rho_i, u)}{\sqrt{\rho_i - u}} F_n(u) \mathrm{d}u$$

In the sub-interval $[\rho_{k-1}, \rho_k]$, we approximate $F_n(u)k_n(\rho_i, u)$ by a linear function taking the values $F_n(\rho_{k-1})k_n(\rho_i, \rho_{k-1})$ and $F_n(\rho_k)k_n(\rho_i, \rho_k)$ at the endpoints ρ_{k-1} and ρ_k, respectively. This is given by

$$F_n(u)\ k_n(\rho_i, u) \approx F_{k-1}^n(\ k_n(\rho_i, \rho_{k-1})\frac{\rho_k - u}{h} + F_k^n\ k_n(\rho_i, \rho_k)\frac{u - \rho_{k-1}}{h}.$$

Hence

$$\widetilde{g}_n(\rho_i) \approx \sum_{k=1}^{i} \int_{\rho_{k-1}}^{\rho_k} \frac{1}{\sqrt{\rho_i - u}} \{F_{k-1}^n k_n(\rho_i, \rho_{k-1})\frac{\rho_k - u}{h} + F_k^n k_n(\rho_i, \rho_k)\frac{u - \rho_{k-1}}{h}\} \mathrm{d}u.$$

A straightforward computation gives

$$\int_{\rho_{k-1}}^{\rho_k} \frac{\rho_k - u}{\sqrt{\rho_i - u}} \mathrm{d}u = -\frac{4}{3}h^{3/2}\Big\{(i-k+1)^{3/2} - (i-k)^{3/2} + 2(i-k+1)^{1/2}\Big\}.$$

In a similar way

$$\int_{\rho_{k-1}}^{\rho_k} \frac{u - \rho_{k-1}}{\sqrt{\rho_i - u}} \mathrm{d}u = \frac{4}{3}h^{3/2}\Big\{(i-k+1)^{3/2} - (i-k)^{3/2} - 2(i-k)^{1/2}\Big\}.$$

Hence

$$\begin{aligned} \widetilde{g}_n(\rho_i) = \sqrt{h}\sum_{k=1}^{i} \Bigg(& -\frac{4}{3}\{(i-k+1)^{3/2} - (i-k)^{3/2}\} + 2(i-k+1)^{1/2}\Bigg) \\ & \times F_n(\rho_{k-1})k_n(\rho_i, \rho_{k-1}) + \\ & \Bigg(\frac{4}{3}\{(i-k+1)^{3/2} - (i-k)^{3/2}\} - 2(i-k)^{1/2}\Bigg) \\ & \times F_n(\rho_k)k_n(\rho_i, \rho_k). \end{aligned} \tag{8.15}$$

Recall that $F_n(R-t) = f_n(t)$ and because of the assumptions on the support of f, we have that $F_n(0) = 0$ for all n. Then (8.15) reduces to

$$\sqrt{h}\Big\{\sum_{k=1}^{i} a_{i-k}\ k_n(\rho_i, \rho_k)\ F_n(\rho_k)\Big\} = \widetilde{g}_n(\rho_i), \qquad i = 1, \cdots, M \tag{8.16}$$

where

$$a_0 = \frac{4}{3}, \qquad a_i = \frac{4}{3}\{(i+1)^{3/2} - 2i^{3/2} + (i-1)^{3/2}\}, \qquad i = 1, \cdots, M.$$

The following theorem states the error estimate for the solution of the integral equation.

Theorem 8.3.2 (Error Estimates)**.** *[107, Thm. 4.1] Let F_n^{exact} be the C^3 solution of (8.14) in $[0, R-\varepsilon]$ and F_n be the solution to* (8.16)*. Then*

$$\max_{0 \le i \le M} \|F_n^{\text{exact}}(\rho_i) - F_n(\rho_i)\| = \mathcal{O}(h^2). \tag{8.17}$$

Equation (8.16) can be written in matrix form as

$$A_n F_n = \widetilde{g}_n, \tag{8.18}$$

where

$$F_n = \begin{pmatrix} F_n(\rho_1) \\ \vdots \\ F_n(\rho_M) \end{pmatrix}, \qquad \widetilde{g}_n = \begin{pmatrix} \widetilde{g}_n(\rho_1) \\ \vdots \\ \widetilde{g}_n(\rho_M) \end{pmatrix} \tag{8.19}$$

and

$$A_n(i,k) = \begin{cases} a_{i-k}\sqrt{h}\ k_n(\rho_i, \rho_k) & 1 \le k \le i \\ 0 & k > i. \end{cases} \tag{8.20}$$

Equation (8.18) has a unique solution because the eigenvalues of the matrix A_n are $\frac{4}{3}\sqrt{h} > 0$. Figure (8.2) shows the condition number of A_n for different values of n. Since A_n is ill-conditioned for several values of n we use the Truncated Singular Value Decompostion (TSVD) [42] to solve the matrix equation.

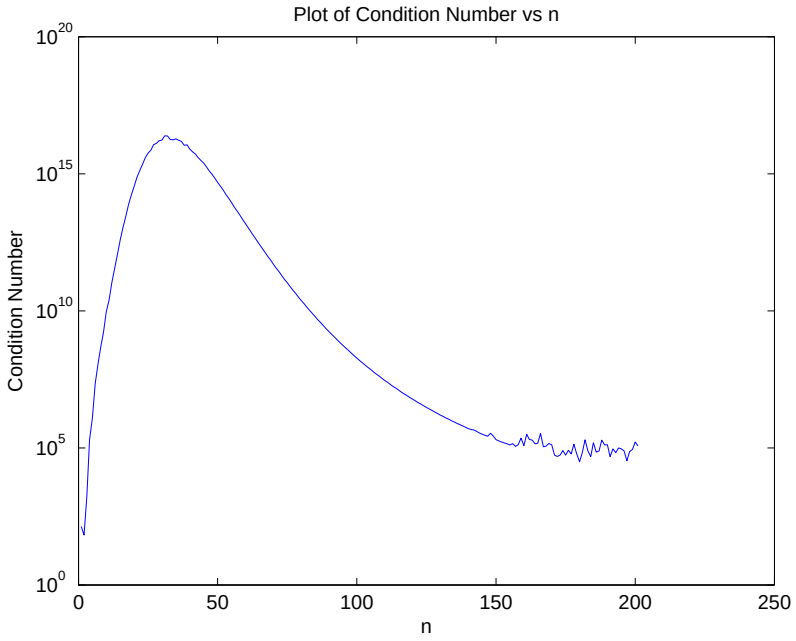

Figure 8.2: Plot of condition number of A_n for $n \in [1, 200]$

8.3.3 Truncated singular value decomposition (TSVD)

In order to solve (8.18), we begin with the SVD of A_n. This is given by $A_n = UDV^T$, where U and V are orthogonal matrices whose columns are the eigenvectors of $A_nA_n^T$ and A_n^TA respectively and D is a diagonal matrix consisting of the singular values of A, that is, the square root of the eigenvalues of $A_n^TA_n$ in descending order represented by $\sigma_i,\ i = 1, \cdots, M$. Now we set

$$A_{n,r} = UD_rV^T \quad \text{and} \quad A_{n,r}^{-1} = VD_r^{-1}U^T$$

where D_r and D_r^{-1} are diagonal matrices with diagonal entries

$$(D_r)_{ii} = \begin{cases} D_{ii} & \text{if} \quad i \le r \\ 0 & \text{otherwise.} \end{cases} \qquad \left(D_r^{-1}\right)_{ii} = \begin{cases} \frac{1}{D_{ii}} & \text{if} \quad i \le r \\ 0 & \text{otherwise.} \end{cases}$$

The matrix $A_{n,r}$ approximates A_n, where $1 \le r \le M$ is the rank of the matrix $A_{n,r}$, as follows.

Let us define the 2-norm of a matrix A by

$$\|A\|_2 = \sup_{x \neq 0} \frac{\|Ax\|_2}{\|x\|_2}. \tag{8.21}$$

It is well known that $\|A\|_2$ is the largest singular value of A [47]. We have that the condition number $\kappa(A_{n,r})$ of $A_{n,r}$ is given by $\kappa(A_{n,r}) = \frac{\sigma_1}{\sigma_r}$ [42].

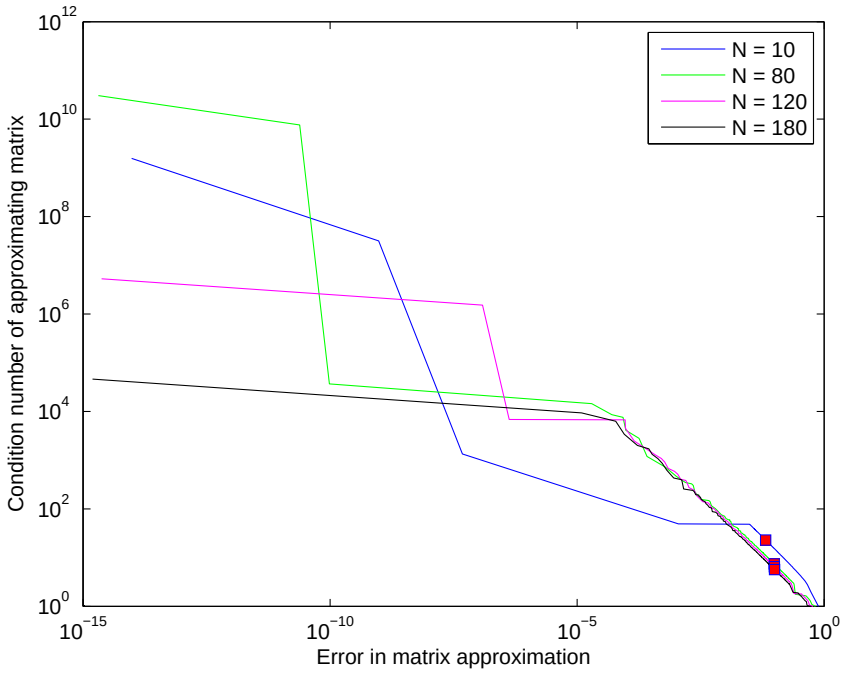

Figure 8.3: Relation between condition number of $A_{n,r}$ and the error in 2-norm from the original matrix A_n, respectively for $n = 10, 80, 120, 180$. The dots on the figures correspond to the half-rank approximation.

Furthermore $\|A_n - A_{n,r}\|_2 = \sigma_{r+1}$. Therefore $A_{n,r}$ for r large, would be a good approximation to A_n, but with high condition number, whereas if r is small, the condition number would be small but the error in the approximation $\|A - A_{n,r}\|_2$ would be large.

Figure 8.3 shows the relation between the condition number of the truncated matrix $A_{n,r}$ and the error $\|A_n - A_{n,r}\|_2$, where the norm is defined by (8.21), for the Fourier coefficients $n = 10, 80, 120$ and 180. For simplicity we considered the matrix arising out of the integral equation (8.1). The other cases are similar.

Due to the competing considerations mentioned above, in all our reconstructions, we chose half-rank approximations ($r = M/2$, where recall that M is the number of discretizations in ρ) to A_n for all n. The condition number of the approximating matrix $A_{n,M/2}$ in all the cases was found to be less than 10. Note that our choice of approximation was independent of the Radon data. Half-rank approximations gave good reconstructions for both the circular and elliptical Radon transforms considered here; see §8.4. We also tested the scheme with rank approximations $r \gg \frac{M}{2}$ and $r \ll \frac{M}{2}$ and found the results to be worse compared to the half-rank approximation case. See Figures 8.6a and 8.6b in §8.4.

8.3.4 Numerical solution of Volterra-type integral equation of second kind

The method of the previous section can also be applied to Volterra-type integral equations of the second kind. It again leads to a non-singular matrix A_n with high condition number.

Given a Volterra integral equation of the first kind,

$$g_n(\rho) = \int_0^\rho \frac{K_n(\rho, u) F_n(u)}{\sqrt{\rho - u}} \mathrm{d}u,$$

one can transform this into a Volterra-type integral equation of the second kind [106] which is

given by

$$G_n(\rho) = F_n(\rho) + \int_0^\rho L_n(\rho, u) F_n(u) du \tag{8.22}$$

where

$$G_n(\rho) = \frac{1}{\pi K_n(t,t)} \frac{\mathrm{d}}{\mathrm{d}\rho} \int_0^\rho \frac{g_n(u)}{\sqrt{\rho - u}} \mathrm{d}u$$

and

$$L_n(\rho, u) = \frac{1}{\pi K_n(\rho,\rho)} \frac{\mathrm{d}}{\mathrm{d}\rho} \int_u^\rho \frac{K_n(t,u)}{\sqrt{t-u}\sqrt{\rho - t}} \mathrm{d}t.$$

We can apply the trapezoidal product integration method to (8.22) with the discretization $\rho_l = lh, \quad l = 0, \cdots, M$ and $h = \frac{R-\epsilon}{M}$ of $[0, R-\epsilon]$ and we arrive at the following matrix equation:

$$(I + A_n) F_n = G_n \tag{8.23}$$

where F_n and G_n are similar to (8.19) and

$$A_n(i,k) = \begin{cases} a_k L_n(\rho_i, \rho_k) & 1 \le k \le i \\ 0 & j > i \end{cases} \tag{8.24}$$

with $a_k = h$, for $k = 1 \cdots i-1$ and $a_i = h/2$.

Remark 8.3.1. *One could apply the numerical algorithm given in this paper to the matrix equation* (8.24)*. However, the evaluation of G_n and L_n involves calculating derivative of an integral which leads to numerical instabilities and hence a high percentage of error. Furthermore, numerical computation of G_n and L_n is time consuming.*

8.4 Numerical Results

We now show the results of the numerical computations performed for the circular and elliptical Radon transforms considered in Theorems 8.2.1, 8.2.2 and 8.2.3. The trapezoidal integration method requires the function to be recovered to be C^3 for $\mathcal{O}(h^2)$ convergence of the approximate solution to the actual one (see Theorem 8.3.2). Nevertheless, we tested our algorithm on functions with jump singularities and it gave good reconstructions. We discretized $\phi \in [0, 2\pi]$ into 400 equally spaced grid points and $\rho \in [0, R-\varepsilon]$ into 400 equally spaced grid points for all the computations. Additionally, we tested the numerical algorithm on 1000 equally spaced grid points in the ρ space for the computations in §8.4.1 and §8.4.1. In all cases we take $R = 1$ unless mentioned otherwise. Besides analysing the physical properties of the reconstructed image, we also evaluate the relative L^2 error percentage between the actual and the reconstructed images, which is defined as

$$\text{Relative } L^2 \text{ error percentage} = \frac{\|f_{\text{rec}} - f_{\text{ex}}\|}{\|f_{\text{ex}}\|} * 100\%$$

where $f_{\text{ex}} = f_{\text{ex}}(x_i, y_j)$ and $f_{\text{rec}} = f_{\text{rec}}(x_i, y_j)$, $i, j = 1 \cdots M$ represents the discretized matrix for the exact function and the reconstructed function respectively, $\|f\| = \frac{1}{M}\sqrt{\sum_{i=1}^M \sum_{j=1}^M f_{ij}^2}$ and $f = f(x_i, y_j)$.

Remark 8.4.1. *The inversion formulae presented here are subtle. We are interested in validating the analytical representation of the formulae. Since we do not have access to real data, we generate our own synthetic Radon data. To do so, we need to integrate the function to be recovered along circles $C(\rho, \phi)$ or ellipses $E(\rho, \phi)$. In this context, we choose a phantom which has an analytic representation and then numerically integrate along given circles using trapezoidal method with 200 points.*

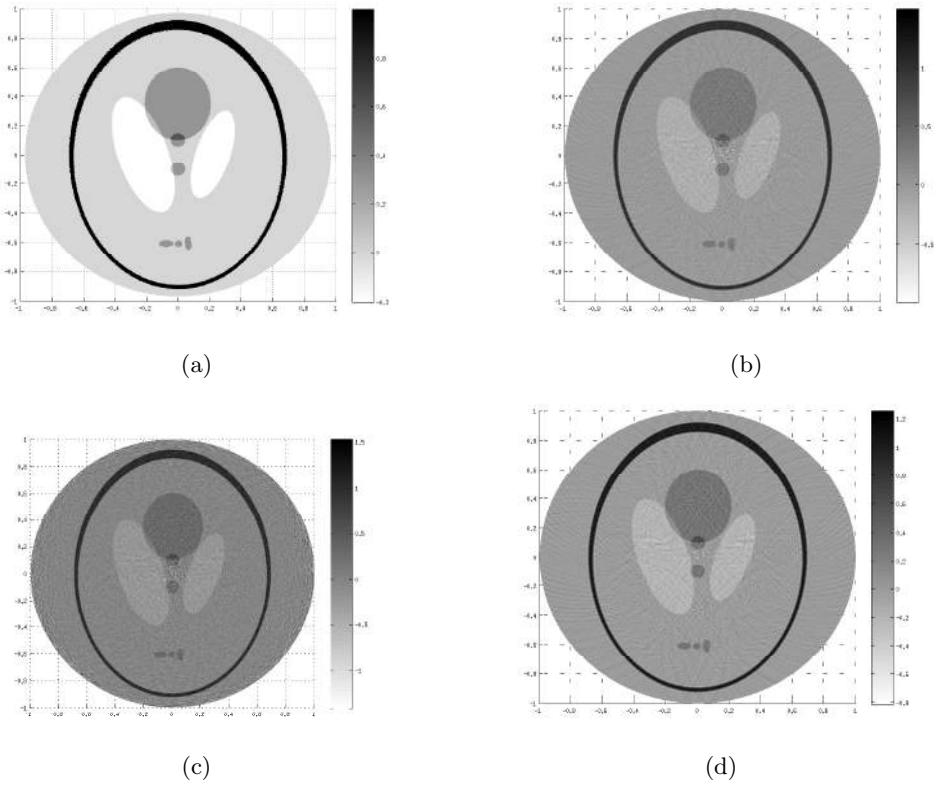

(a) (b)

(c) (d)

Figure 8.4: Results for circular Radon transform data for a function supported in an interior annulus of $\partial B(0, R)$. Figure 8.4a shows the actual Shepp-Logan phantom and Figures 8.4b, 8.4c and 8.4d show the reconstructed images with 400, 400 with 10% added Gaussian noise, and 1000 equally spaced discretizations in ρ, respectively.

8.4.1 Functions supported in an interior annulus

This corresponds to the case when the object we are interested in reconstructing are supported in an annulus centered at 0 of the circle $\partial B(0, R)$ and the circular and elliptical Radon transforms are along circles (ellipses) with center (foci) on $\partial B(0, R)$, see Theorem 8.2.1. For the circular Radon transform case, the matrix A_n consists of entries coming from the kernel equation (8.2), whereas for the elliptical Radon transform case, the matrix entries come from (8.4).

In both the circular and elliptic transform cases discussed below, we notice a good recovery of the image near the origin which is a point of singularity. There is reduction in the number of artifacts as we increase the number of discretization points and hence the relative L^2 error decreases with increasing refinement.

Circular Radon transform data

Figure 8.4a shows the Shepp-Logan phantom which is recovered by numerical inversion in Figures 8.4b, 8.4c and 8.4d using 400 (without and with 10 % Gaussian noise) and 1000 equally spaced discretizations in ρ, respectively. The relative L^2 errors between Figures 8.4a and 8.4b, Figures 8.4a and 8.4c, and Figures 8.4a and 8.4d are 18.6%, 24.2% and 10.1%, respectively. A smooth version of the Shepp-Logan phantom is shown in Figure 8.5 which is also recovered well by the inversion formula. The relative L^2 error between these images is 5.7%, showing that the algorithm performs better with smooth initial data.

To justify the rationale behind half-rank approximations, we tested the algorithm with rank approximations $r = M/8$ and $r = M/1.5$. The results are shown in Figures 8.6a and 8.6b respectively. The relative L^2 error for the first case was 65.8% and for the second case was

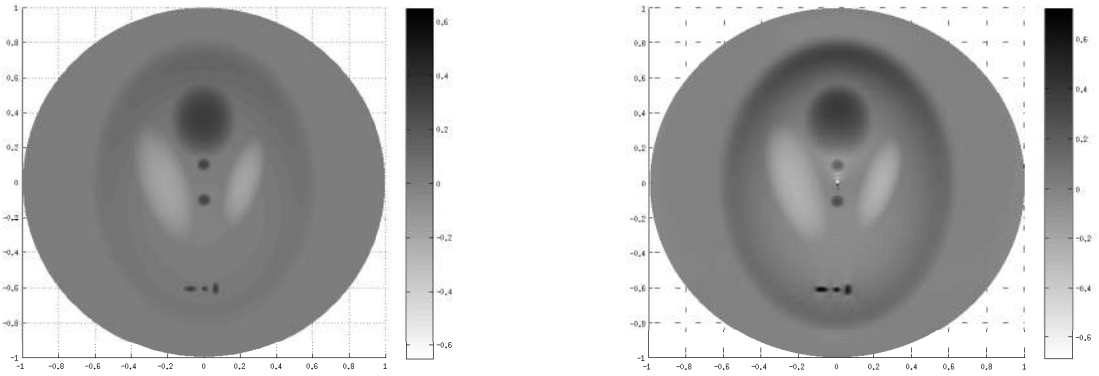

(a) (b)

Figure 8.5: Results for circular Radon transform data for a function supported in an interior annulus of $\partial B(0, R)$. Figure 8.5a shows a smooth version of the Shepp-Logan phantom and Figure 8.5b shows the reconstructed image.

280.1%. This suggests rank approximations too far away from half-rank approximations can either lead to loss of data or lead to blow-offs which results in improper reconstruction.

Elliptical Radon transform data

Figure 8.7 shows the actual and reconstructed images with 400 and 1000 equally spaced discretizations in ρ from elliptical Radon transform data using the numerical algorithm of Section 8.3 based on the result of Part 2 of Theorem 8.2.1.

For the computations we assumed that an object is placed inside the annulus $A(\epsilon, b)$ where $b = R\cos\alpha$ with $\alpha = 30^\circ$ is the length of the semi-minor axis. The resulting integral equation to be solved is given by (8.3) with the kernel $K_n(\rho, u)$ given by (8.4). We see that all the objects in the image have been reconstructed even with the coarser discretization of 400 points. The relative L^2 errors between the Figures 8.7a and 8.7b, and between the Figures 8.7a and 8.7c are 14.2% and 10.6%, respectively.

8.4.2 Functions supported inside $A(R, 3R)$

In this test case, we use circular Radon transform data for functions supported inside $A(R, 3R)$. The integral equation to be considered in this case is (8.6) with the kernel $K_n(\rho, u)$ as defined in (8.7). The actual and reconstructed images are shown in Figure 8.8. Microlocal analysis arguments show that the entire circumference of the two circles cannot be constructed stably with the given circular Radon transform data [40, 41, 39, 81]. We see the presence of an increased number of artifacts in constrast to the interior case (see §8.4.1). The image reconstructed is consistent with this analysis. The relative L^2 error between these images is 35.5%. While the error is large, the number and location of the objects in the image are recovered.

8.4.3 Functions supported on both sides of $\partial B(0, R)$

Circular Radon transform data for functions supported on both sides of $\partial B(0, R)$

We considered a function supported inside the annulus $A(R_1, R_2)$ where $R_2 > 2R$ and $R_1 = R_2 - 2R$ (See Figure 8.9a). In the computations we chose $R = 1.47, R_2 = 3$. Therefore $R_1 = 0.06$. The resulting integral equation is given by (8.8) with the kernel $K_n(\rho, u)$ defined by (8.9). The actual and reconstructed images are shown in Figure 8.9. As in the Figure 8.8, microlocal analysis of the given circular Radon transform data shows that certain parts of boundary of the

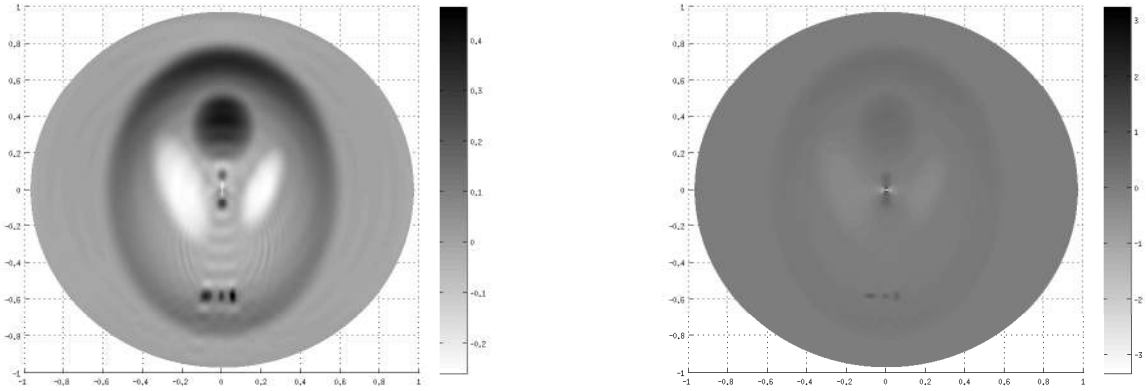

(a) (b)

Figure 8.6: Results for circular Radon transform data for a function supported in an interior annulus of $\partial B(0, R)$. Figure 8.6a shows the reconstruction of smooth version of the Shepp-Logan phantom with $r = M/8$ and Figure 8.6b shows the reconstruction with $r = M/1.5$. Figure 8.6a reveals incomplete reconstruction due to loss of data whereas Figure 8.6b reveals blow-off in the solution.

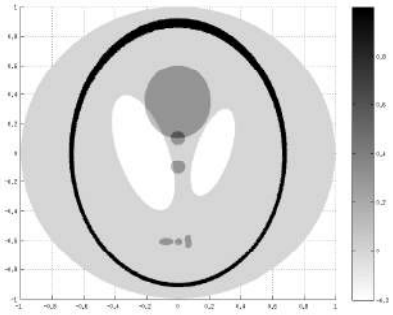

(a)

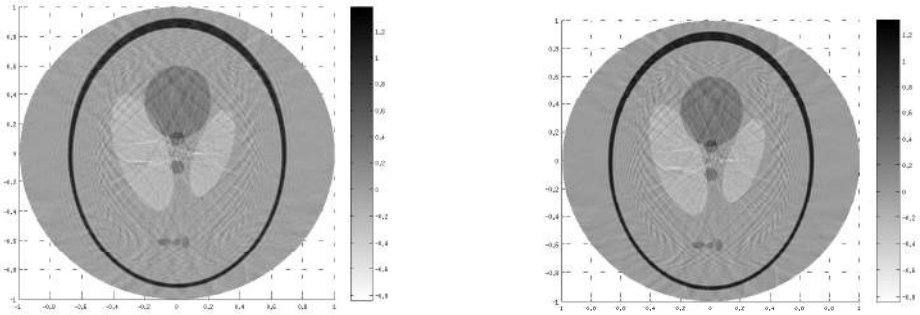

(b) (c)

Figure 8.7: Results of elliptical Radon transform data for a function supported in an interior annulus of $\partial B(0, R)$. Figure 8.7a shows the actual Shepp-Logan phantom and Figures 8.7b and 8.7c show the reconstructed images with 400 and 1000 equally spaced discretizations in ρ, respectively.

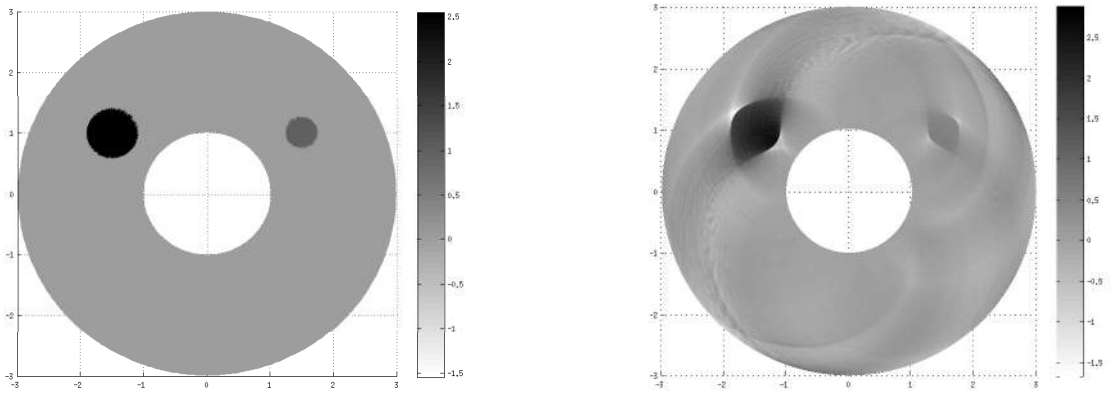

(a) (b)

Figure 8.8: Results for circular Radon transform data for a function supported in an annular region of $C(R, 3R)$. The circular Radon transform data is taken over circles centered on the inner circle. Figure 8.8b shows the reconstructed image.

disc outside the dotted circle cannot be stably reconstructed. Note that the boundary of inner disc is reconstructed well. The relative L^2 error between these images is 32.1%.

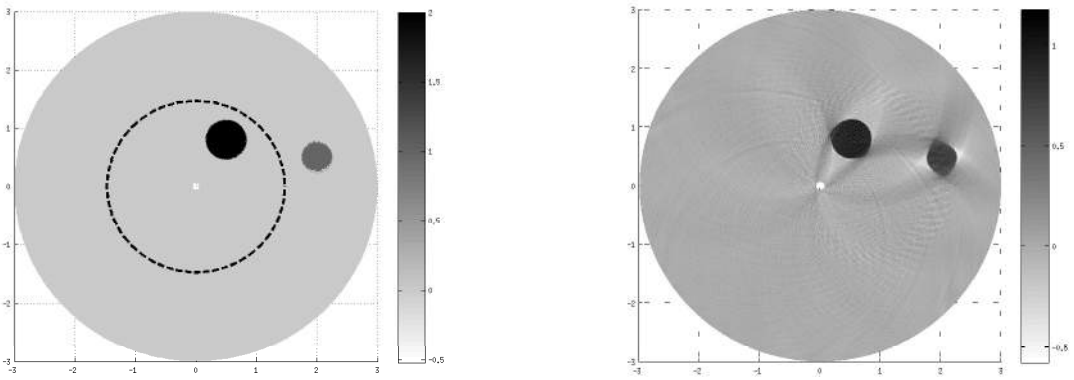

(a) (b)

Figure 8.9: Simulation with circular Radon transform data (Part 1 of Thm 8.2.3) for a function supported on both sides of the circle $\partial B(0, R)$ shown by the dotted circle in Figure 8.9a. Figure 8.9a shows the actual image and Figure 8.9b shows the reconstructed image.

Elliptical Radon transform data for functions supported on both sides of $\partial B(0, R)$

Finally, we tested our algorithm for Part 2 of Theorem 8.2.3. We considered a function placed inside the annulus $A(R_1, R_2)$ where we chose the angle $\alpha = 20°$, $R = 1.47$ and $R_2 = 3$. Then $R_1 = R_2 - 2b = R_2 - 2R\cos 20° \approx 0.237$. We tested the numerical algorithm on the integral equation (8.10) with the kernel $K_n(\rho, u)$ given by (8.11) and the results are shown in Figure 8.10. Same microlocal analysis reasons [3] as in Figure 8.9 applies for this case as well. The relative L^2 error between these images is 31.8% without noise and with 10% Gaussian noise, the relative L^2 error is 52.2%.

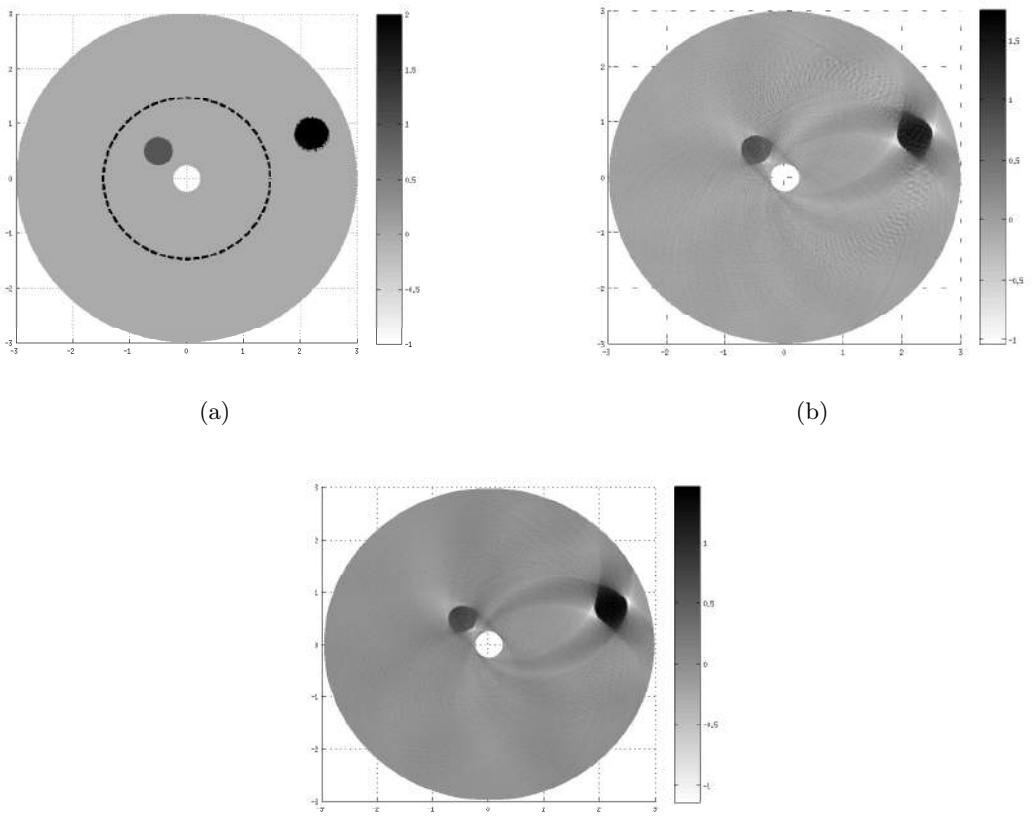

(a) (b)

(c)

Figure 8.10: Simulation with elliptical Radon transform data (Part 2 of Theorem8.2.3) for a function supported on both sides of the circle $\partial B(0, R)$ shown by the dotted circle in Figure 8.10a. Figure 8.10a shows the actual image, Figure 8.10b and Figure 8.10c show the reconstructed image without and with 10% Gaussian noise, respectively.

8.5 Computational Time

We now demonstrate the computational efficiency of our developed algorithm by demonstrating the computational times taken for various reconstructions. We first note that in Section 8.4 we state that the number of angular discretizations in ϕ is fixed to be 400. We only vary the number of radial discretizations ρ to be either 400 or 1000. This is based on the reasoning that since a ray is continuous, given an entry point on the circle $\partial B(0, R)$, it can sweep any set of points in the radial direction. But the number of such entry points determines the number of rays entering the object, eg. a body, which might be restricted depending on the scanner or the condition of the object. Hence we can choose any number of radial discretizations but only a fixed number of angular discretizations.

The reconstruction of the function f can be divided into two phases

1. Pre-processing step.
2. Inversion algorithm step.

In the pre-processing step, we compute the inverse of the matrix A_n given in (8.18) for $n = 1, \ldots, N/2+1$ using the half-rank truncated SVD inversion technique described in Section 8.3.3. The inversion algorithm step consists of the Fourier transform of the Radon data, computing the solution f_n for each n, evaluating f using the inverse Fourier transform and finally displaying the results. The computations are performed in MATLAB with machine configuration of 4 GB RAM, 2.5 GHz I3-processor and 2 clusters.

Phantom	Support	RT Type	Grid	Pre-processing	Inversion algorithm
Shepp-Logan	Interior	Circular	400	610.1 sec	44.4 sec
Shepp-Logan	Interior	Circular	1000	4164.7 sec	55.8 sec
Smooth Shepp-Logan	Interior	Circular	400	612.2 sec	45.4 sec
Shepp-Logan	Interior	Elliptical	400	611.7 sec	45.1 sec
Shepp-Logan	Interior	Elliptical	1000	4163.8 sec	56.4 sec
2 Disks	Combined	Elliptical	400	611.5 sec	45.4 sec

Table 8.1: Time taken for the pre-processing step and inversion algorithm for the two types of discretizations of ρ. RT type stands for the type of Radon transform.

Table 8.1 presents the computational times for the various experiments performed. It can be seen that the computational time depends on the number of radial discretizations of ρ rather than the type of transforms or support of the reconstructed function f. We can see from Table 8.1, that the computational time taken for the pre-processing step is quite large. But since this step is independent of data, given the number of angular discretizations N, this step is computed once, stored in memory and can be used for inversion of any kind of Radon data. This makes the inversion procedure quite fast which can be seen from the time taken for the inversion algorithm step running at less than a minute even for 1000 discretizations on a comparatively slow machine. With the fast computing machines, one can attain high speeds. Such a task is beyond the scope of this work and would be considered in future works.

8.6 Conclusions

We have developed a numerical technique to solve the inversion formulas for circular and elliptical Radon transforms arising in some imaging applications. The inversion formulae and the proposed numerical scheme have been demonstrated to give good reconstructions on some standard test problems involving both discontinuous and smooth images. While the absolute

errors in the reconstructed image are large, especially for discontinuous images, what is more important is that the objects in the image are properly distinguished by the current method. The numerical algorithm requires the solution of ill-conditioned matrix problems which is accomplished using a truncated SVD method. The matrices and the SVD can be constructed in a pre-processing step and re-used repeatedly for the subsequent computations leading to an efficient and fast algorithm.

Chapter 9

Conclusion

The main aim of the thesis was to study some inverse problems related to fluid flows and tomography. In the field of fluid flows, we build methods to determine the two dimensional velocities of a fluid by capturing the movement of the objects in the fluid. Such a method could be applied to determine the motion of clouds using data from the geo-stationary satellites. This information could be useful for farmers,meterologists, etc. In the field of tomography, efficient numerical inversion techniques is presented to reconstruct a function from its circular and elliptic Radon transforms. Such a work is relevant in various imaging modalties like ultrasound imaging, radar imaging and sonar imaging. This chapter will summarize the main contributions of the thesis and will also hint at future work to be done.

9.1 Contributions of the thesis

9.1.1 Methodology

1. In the second chapter, the classical Horn and Schunck method was revisited and used to determine fluid flow velocities by minimizing the Horn-Schunck functional along with the two constraints: the data conservation constraint and the smoothness constraint. We pointed out with illustrations why they were needed. A finite difference iterative scheme was used and the method was used to recover a simple constant flow.

2. In the third chapter, a unique minimizer of the Horn-Schunck functional was shown along with some regularity results. Stability estimates of the minimizer was shown in terms of the given image data which suggested that the velocity field obtained depends continuously on the image derivatives, the domain of definition and the smoothing parameter.

3. In the fourth chapter, fluid flow velocities of a constant flow used in the first chapter was recovered by minimizing the Horn-Schunck functional and using numerical implementation based on the finite element method. The results of the finite difference method from the first chapter and the finite element method in this chapter were compared.

4. In the fifth chapter, our aim was to track steady state incompressible fluid flows. We additionally assumed that the underlying fluid flow is a potential flow and tried to recover it by minimizing a functional. A finite element numerical method was used and tests were done to recover two flows: the first one being a constant flow and the second one being a flow due to point vortex with source of the vortex outside the domain of definition.

5. In the sixth chapter, a new method was devised to track steady state incompressible fluid flows. Based on a constraint based minimization method with incompressibility as the only constraint, the method is used to track flows governed by steady state Stokes and Navier-Stokes equations with known boundary conditions.

6. In the seventh chapter, a new method was devised to track time-dependent incompressible vortex flows. Again a constraint based minimization technique was used with unsteady Euler or Navier-Stokes flow constraints and tested with two vortex flows.

7. In the final chapter, an efficient numerical inversion technique was presented to recover a function from its circular and elliptic Radon transforms. The inversion technique is used to reconstruct several phantoms.

9.1.2 Results

1. After comparing the finite difference and the finite element method implemented in the second and fourth chapters, it was found that the finite element method was comparatively better than the finite difference method. With this idea, we went about tracking incompressible flows using the finite element method. In the third chapter, existence and uniqueness of minimizer of the Horn-Schunck functional was shown which was necessary for efficient numerical implementation.

2. In the fifth chapter, where we attempt to track incompressible flows, the flow was assumed to be potential. It was found from the numerical results that the recovery was not that good. The reason pointed out was lack of sufficient information about the flow in terms of the boundary conditions assumed. In view of this problem, a new method was implemented in the sixth chapter, assuming incompressibility condition and known boundary condition. A nice outcome of the method was that Stokes flow forced by a potential was recovered almost exactly irrespective of the smoothing parameter. But since steady state flows were considered, flow dynamics over various times was missing which resulted in the method not being able to capture non-linear effects like vortices generated by Navier-Stokes equations. In an attempt to modify this shortcoming, another new method was proposed in chapter seven which could efficiently capture vortex flows governed by unsteady incompressible Euler or Navier-Stokes equations.

3. In the final chapter, the numerical inversion algorithm was shown to be fast because of a pre-processing step and also accurate even in the presence of noise. A truncated SVD technique was used and based on the balance between conditioning and error in approximation of the system, half rank approximations were suggested. The results show good reconstructions for several phantoms.

9.1.3 Inference

The methods proposed for tracking incompressible fluid flows using optical flow techniques are simple yet quite efficient. They are not computationally expensive and accurate. The methods have been studied both from the theoretical and numerical point of view. These methods can be extended further to track compressible flows. For image reconstruction, the numerical algorithm suggested was used to reconstruct a function from its circular and elliptic Radon transforms in 2D. Such a method could also be used in reconstructing a function from 3D spherical Radon transforms as well as other types of Radon transforms based on Fourier techniques.

9.2 Future work

Our future work is aimed at a study of more complicated inverse problems in the field of fluid flows and tomography to account for various other assumptions besides the ones already considered here. We would like to create better methods so that we provide the best information to the farmers, meterologists and the doctors who work hard for the sake of the benefit of the world to make it a better and safer place to live in.

Appendix A

Rate of change of image brightness

Consider a patch of brightness pattern that is displaced a distance δx in the x-direction and δy in the y-direction in time δt. The brightness of the patch is assumed to remain constant so that

$$E(x, y, t) = E(x + \delta x, y + \delta y, t + \delta t)$$

Expanding the right hand side about the point (x, y, t) we get,

$$E(x, y, t) = E(x, y, t) + \delta x \frac{\partial E}{\partial x} + \delta y \frac{\partial E}{\partial y} + \delta t \frac{\partial E}{\partial t} + \epsilon$$

where ϵ contains second and higher order terms in $\delta x, \delta y$ and δt. After subtracting $E(x, y, t)$ from both sides and dividing through by δt we have

$$\frac{\delta x}{\delta t}\frac{\partial E}{\partial x} + \frac{\delta y}{\delta t}\frac{\partial E}{\partial y} + \frac{\partial E}{\partial t} + O(\delta t) = 0$$

where $O(\delta t)$ is a term of order δt, and we assume that δx and δy vary as δt. In the limit as $\delta t \to 0$ this becomes

$$\frac{\partial E}{\partial x}\frac{dx}{dt} + \frac{\partial E}{\partial y}\frac{dy}{dt} + \frac{\partial E}{\partial t} = 0$$

which is same as

$$E_t + \nabla E \cdot U = 0$$

where $U = (u, v)$ and $u = \frac{dx}{dt}$, $v = \frac{dy}{dt}$.

Appendix B

Existence Of An Unique Global Minimizer

First we will show that the functional $J(U)$, as given in (6.1), is continuous on Z We use the following results (See [82]). Let X be an open set in a normed linear space L with norm $\|.\|$.

Theorem B.0.1. *Let $J : Z \to \mathbb{R} \cup \{-\infty, \infty\}$ be a convex functional on X. If J is bounded from above in a neighborhood of a point $U_0 \in X$ then it is locally bounded i.e each $U \in X$ has a neighborhood on which J is bounded.*

Proof. We first show that if J is bounded above in an ϵ-neighborhood of some point, it is bounded below in the same neighborhood. We choose a neighborhood of the point 0. Let $|J(U)| \leq B \quad \forall U \in N_\epsilon(0)$ where $N_\epsilon(0)$ is a neighborhood of the origin given by

$$N_\epsilon(0) = \{U \in X : \|U\| < \epsilon\}$$

Since

$$0 = \frac{1}{2}U + \frac{1}{2}(-U)$$

By convexity of J we get,

$$J(0) \leq \frac{1}{2}J(U) + \frac{1}{2}J(-U)$$

This gives,

$$J(U) \geq 2J(0) - J(-U)$$

Now, $\|U\| < \epsilon$ implies $\| - U\| < \epsilon$.

Therefore

$$-J(-U) \geq -B, J(U) \geq 2J(0) - B$$

This means J is bounded from below.
Now for proving the theorem, we take J to be bounded from above by B on an ϵ-neighborhood N of the origin. We will show J to be bounded in a neighborhood of $U \in X, U \neq 0$. We choose $\rho > 1$ so that $V = \rho U \in X$ and let $\lambda = \frac{1}{\rho}$.Then

$$M = \{W \in L : W = (1 - \lambda)Y + \lambda V, Y \in N\}$$

is a neighborhood of $\lambda V = U$ with radius $(1 - \lambda)\epsilon$. Moreover

$$J(W) \leq (1 - \lambda)J(Y) + \lambda J(V) \leq B + J(V).$$

So J is bounded above on M and by he first part of this proof J is bounded below on M. $\square$

Definition B.0.1. *A functional J defined on an open set X is said to be* ***locally Lipschitz*** *if at each $U \in X$ there exists a neighborhood $N_\epsilon(U)$ and a constant $K(U)$ such that if $V, W \in N_\epsilon(U)$, then,*

$$|J(V) - J(W)| \leq K\|V - W\|_Z$$

If this inequality holds throughout a set $Y \subseteq X$ with K independent of U then we say that J is ***Lipschitz*** *on Y.*

Theorem B.0.2. *Let J be convex on an open set $X \subseteq L$. If J is bounded from above in a neighborhood of one point of X, then J is locally Lipschitz in X.*

Proof. By Theorem B.0.1, J is locally bounded. So given U_0 we may find a neighborhood $N_{2\epsilon}(U_0) \subseteq X$ on which J is bounded, say by M. Then J satisfies the stated Lipschitz condition on $N_\epsilon(U_0)$, for if it does not, we may choose $U_1, U_2 \in N_\epsilon(U_0)$ s.t.

$$\frac{J(U_2) - J(U_1)}{\|U_2 - U_1\|} > \frac{2M}{\epsilon}$$

Then we may choose $\alpha > 0$ s.t. $U_3 = U_2 + \alpha(U_2 - U_1)$ is in $N_{2\epsilon}(U_0)$ and $\|U_3 - U_2\| = \epsilon$. Because J is convex on the line through U_1, U_2, U_3 , we may use the following inequality,

$$\frac{J(U_3) - J(U_2)}{\|U_3 - U_2\|} \geq \frac{J(U_2) - J(U_1)}{\|U_2 - U_1\|} > \frac{2M}{\epsilon}$$

This gives us $J(U_3) - J(U_2) > 2M$, contradicting the fact that $|J| \leq M$.

Hence J is locally Lipschitz. □

Theorem B.0.3. *Let J be convex on X. If J is bounded from above in an neighborhood of one point of X, then J is continuous on X.*

Proof. Theorem 6.3.2 implies J is locally Lipschitz, from which continuity follows immediately. □

Theorem B.0.4. *The functional J as given in (6.1) is continuous*

Proof. We will use the Theorem B.0.3 to prove our statement. We assume

$$\|E\|_{W^{1,\infty}(\Omega)} \leq M.$$

As $0 \in Z$, we consider a neighborhood of zero given as $N_1 = \{U : \|U\|_Z < 1\}$. Now

$$\begin{aligned}
|J(U)| &= \left| \frac{1}{2} \int_\Omega (U \cdot \nabla E + E_t)^2 \, dxdy + \frac{K}{2} \int_\Omega \left[\|\nabla u\|^2 + \|\nabla v\|^2 \right] dxdy \right| \\
&\leq \frac{1}{2} \int_\Omega (U \cdot \nabla E + E_t)^2 \, dxdy + \frac{K}{2} \|U\|_Z^2 \\
&\leq \frac{1}{2} \int_\Omega \left(E_t^2 + (U \cdot \nabla E)^2 + 2E_t(U \cdot \nabla E) \right) dxdy + \frac{K}{2} \|U\|_Z^2
\end{aligned}$$

Using Hölder's inequality and L^∞ bound on E and its derivatives we get

$$\begin{aligned}
|J(U)| &\leq \frac{1}{2} \int_\Omega \left[M^2 + M^2(u+v)^2 \right] dxdy + 2M \left(\int_\Omega (\nabla E)^2 \right)^{1/2} \left(\int_\Omega U^2 \right)^{1/2} dxdy + \frac{K}{2} \|U\|_Z^2 \\
&\leq \frac{M^2}{2} \int_\Omega \left[1 + 2(u^2 + v^2) \right] dxdy + M(\int_\Omega M^2)^{1/2} \|U\|_Z + \frac{K}{2} \|U\|_Z^2 \\
&\leq \frac{M^2}{2} (\int_\Omega 1) + M^2 \|U\|_Z^2 + M^2 (\int_\Omega 1) + \frac{K}{2} \|U\|_Z^2 \\
&< \frac{3M}{2} \mu(\Omega) + M^2 + \frac{K}{2} \qquad (\text{ as } \|U\|_Z < 1) \\
&< \infty.
\end{aligned}$$

where $\mu(\Omega)$ is the measure of Ω. This gives us $J(U)$ is bounded above in N_1. As J is convex (by Theorem 6.3.5), we have J is continuous for all $U \in Z$ (by Theorem B.0.3). □

Now we show the existence of the derivative of (6.1).

B.1 Existence Of Gateaux Derivative Of J

Theorem B.1.1. *The Gateaux Derivative of (6.1) exists.*

Proof. The Gateaux Derivative of J at the point U acting on V is defined as

$$\lim_{\epsilon \to 0} \frac{J(U + \epsilon V) - J(U)}{\epsilon}$$

if it exists and is denoted by $J'(U, V)$

By (6.19), the Gateaux Derivative of J is

$$J'(U;V) = \int_\Omega (E_t + (\nabla E \cdot U))(\nabla E \cdot V) + K \int_\Omega (\nabla u_1 \cdot \nabla v_1) + (\nabla u_2 \cdot \nabla v_2)$$

where

$$U = (u_1, u_2), V = (v_1, v_2).$$

We will show it is well defined.

Now,

$$\begin{aligned}
|J'(U;V)| &\leq |\int_\Omega (E_t + (\nabla E \cdot U))(\nabla E \cdot V)| + K|\int_\Omega (\nabla u_1 \cdot \nabla v_1) + (\nabla u_2 \cdot \nabla v_2)| \\
&\leq |\int_\Omega E_t(\nabla E \cdot V)| + |\int_\Omega (\nabla E \cdot U)(\nabla E \cdot V)| + K|\int_\Omega (\nabla u_1 \cdot \nabla v_1) + (\nabla u_2 \cdot \nabla v_2)| \\
&\leq \|E_t\|_H \|\nabla E \cdot U\|_H \|\nabla E \cdot U\|_H \|\nabla E \cdot V\|_H + K(\|\nabla u_1\|_H \|\nabla v_1\|_H + \|\nabla u_1\|_H \|\nabla u_1\|_H)
\end{aligned}$$

By the inequality,$(a+b)^2 \leq (a+b)^2 + (a-b)^2 = 2(a^2+b^2)$, we have,

$$\begin{aligned}
\|\nabla E.U\|_H &\leq \left[2\|E_x\|_{L^\infty}^2 \int_\Omega u_1^2 + 2\|E_y\|_{L^\infty}^2 \int_\Omega u_2^2\right]^{\frac{1}{2}} \\
&\leq \left[2 \max\left\{\|E_x\|_{L^\infty}^2, \|E_y\|_{L^\infty}^2\right\}\right]^{\frac{1}{2}} \|U\|_H
\end{aligned}$$

Hence we obtain

$$\begin{aligned}
|J'(U,V)| &\leq C_1(\|U\|_H + \|U\|_H \|V\|_H + \|\nabla u_1\|_H \|\nabla v_1\|_H + \|\nabla u_2\|_H \|\nabla v_2\|_H) \\
&\leq C_1\|U\|_H + C_1[\|U\|_H^2 + \|\nabla u_1\|_H^2 + \|\nabla u_2\|_H^2]^{\frac{1}{2}} . [\|V\|_H^2 + \|\nabla v_1\|_H^2 + \|\nabla v_2\|_H^2]^{\frac{1}{2}} \\
&= C_1(\|U\|_H + \|U\|_Z \cdot \|V\|_Z) < \infty.
\end{aligned}$$

where,

$$C_1 = 2 \max\left\{\|E_x\|_{L^\infty}^2, \|E_y\|_{L^\infty}^2, \frac{\|E_t^2\|_H \cdot \|E_x\|_{L^\infty}^2}{2}, \frac{\|E_t^2\|_H \cdot \|E_y\|_{L^\infty}^2}{2}, \frac{K}{2}\right\}.$$

So $J'(U, V)$ exists and is well defined. □

B.2 Equivalence of J′(U)=0 and existence of a minimizer for J

Theorem B.2.1. *If the Gateaux derivative vanishes at a point $U = U_0$ then it is a minimizer of (6.1).*

Proof. We have,

$$\begin{aligned} J(U_0 + \epsilon(V - U_0)) &= J((1-\epsilon)U_0 + \epsilon V) \\ &\leq (1-\epsilon)J(U_0) + \epsilon J(V) \qquad \text{(By Convexity of J)} \end{aligned}$$

for any $V \in J(\Omega)$. Let $V - U_0 = H$. Then,

$$J(U_0 + \epsilon H) - J(U_0) = \epsilon(J(V) - J(U_0))$$

This gives,

$$\frac{J(U_0 + \epsilon H) - J(U_0)}{\epsilon} = J(V) - J(U_0)$$

Taking limit on both sides as $\epsilon \to 0$, the left hand side goes to $J'(U_0)$ and the right hand side remains constant as it is independent of ϵ. But $J'(U_0) = 0$. So $J(V) - J(U_0) \geq 0 \quad \forall V \in J(\Omega)$.

Hence $J(V) \geq J(U_0) \quad \forall V \in J(\Omega)$. So U_0 minimizes J globally.

□

Theorem B.2.2. *If there is a global minimizer of (6.1) at $U = U_0$ then Gateaux Derivative of J at U_0 vanishes.*

Proof. Suppose not. Then,

$$\lim_{\epsilon \to 0} \frac{J(U_0 + \epsilon H) - J(U_0)}{\epsilon} = K$$

If $K > 0$ then,

$$\frac{J(U_0 + \epsilon H) - J(U_0)}{\epsilon} > \frac{K}{2} \text{ (for sufficiently small } \epsilon).$$

If $\epsilon < 0$ then,

$$J(U_0 + \epsilon H) - J(U_0) < \epsilon \frac{K}{2}$$

and hence,

$$J(U_0 + \epsilon H) < J(U_0) + \epsilon \frac{K}{2} < J(U_0)$$

which contradicts the fact that U_0 is a global minimizer of J as $U_0 + \epsilon H \in J(\Omega)$ when $H \in J(\Omega)$.

If $K < 0$ then,

$$\frac{J(U_0 + \epsilon H) - J(U_0)}{\epsilon} < 2K \text{ (for sufficiently small } \epsilon).$$

If $\epsilon > 0$ then,

$$J(U_0 + \epsilon H) - J(U_0) < \epsilon 2K.$$

and hence,

$$J(U_0 + \epsilon H) < J(U_0) + \epsilon 2K < J(U_0)$$

which again contradicts the fact that U_0 is a global minimizer of J as $U_0 + \epsilon H \in J(\Omega)$ when $H \in J(\Omega)$.

So the Gateaux derivative of J at the global minimum point U_0 is 0. □

So it follows from above that if there is a unique solution of $J'(U) = 0$ then that unique solution is the global minimizer for J, where J is convex.

Appendix C

Conjugate Gradient method

C.1 Introduction

The solution of the approximate problem: find $u_h \in V_h$:

$$a(u_h, v_h) = F(v_h) \quad \forall v_h \in V_h \tag{C.1}$$

can be found using iterative methods. One such method is the conjugate gradient method. We will discuss about theory of the method in this chapter. Let $\{\phi_i\}_{i=1}^{N_h}$ be a basis of V_h. Let A be the stiffness matrix given by $A = (a(\phi_i, \phi_j))$ and $f = (F(\phi_i))$. If $a(.,.)$ is symmetric, then (C.1) is equivalent to the minimization problem

$$J(u_h) = \min_{v_h \in V_h} J(v_h) \tag{C.2}$$

where

$$J(v) = \frac{1}{2} v^T A V - v^T f, v \in \mathbb{R}^{N_h}. \tag{C.3}$$

So u_h is a solution of (C.2) iff $Au_h = f$.

C.2 Conjugate gradient

Definition C.2.1. *The directions $w_1, w_2 \in \mathbb{R}^N$ are said to be conjugate with respect to the matrix A if*

$$w_1^T A w_2 = 0$$

In the conjugate gradient method, we construct conjugate directions using the gradient of the functional. Then the functional is minimized by proceeding along the conjugate direction. We have the following theorem

Theorem C.2.1. *Let $w_1, w_2, ..., w_N$ be n mutually conjugate directions. Let*

$$x_{k+1} = x_k - \lambda_k w_k$$

where λ_k minimizes

$$\phi(\lambda) = J(x_k - \lambda w_k), \lambda \in \mathbb{R}$$

J is given in (C.3). When $x_1 \in \mathbb{R}^N$ is given, we have

$$x^{N+1} = x^*$$

where

$$Ax^* = f$$

Proof. Let

$$r_n = -J'(x_n) = f - Ax_n$$

Since λ_k minimizes $\phi(\lambda)$, we have

$$\phi'(\lambda_k) = (J'(x_k - \lambda_k w_k), -w_k) = 0$$

This gives

$$\lambda_k = \frac{(r_k)^T w_k}{(w_k)^T A w_k} \tag{C.4}$$

Since $w_1, w_2, ...w_N$ are mutually conjugate directions, they are linearly independent. Therefore there exist $\alpha_i, i \leq i \leq n$, such that

$$x_1 - x^* = \sum_{k=1}^{n} \alpha_k w_k$$

From this, using the fact that w_j are mutually conjugate, we obtain

$$(x_1 - x^*)^T A w_j = \alpha_j (w_j)^T A w_j$$

This gives

$$\alpha_j = \frac{(x_1 - x^*)^T A w_j}{(w_j)^T A w_j} \tag{C.5}$$

Using induction we show that

$$\alpha_k = \lambda_k$$

Since $Ax^* = f$, we have

$$r_1 = f - Ax_1 = A(x_* - x_1)$$

This shows that

$$\alpha_1 = \lambda_1$$

Let $\alpha_i = \lambda_i$ for $1 \leq i \leq k$. From the definition of x_k we obtain,

$$x_k = x_1 - \sum_{i=1}^{k-1} \lambda_i w_i = x_1 \sum_{i=1}^{k-1} \alpha_i w_i,$$

(by induction hypothesis). Since

$$(w_i)^T A w_k = 0, 1 \leq i \leq k-1,$$

we get

$$(x_k - x_1)^T A w_k = 0$$

This together with (C.4) and (C.5) shows that

$$\alpha_k = \lambda_k$$

Thus $\alpha_k = \lambda_k$ for $1 \leq k \leq n$. The definition of x_k implies

$$x_{N+1} = x_1 - \sum_{i=1}^{n} \lambda_i w_i = x_1 - \sum_{i=1}^{n} \alpha_i w_i = x^*$$

□

Now the final theorem in this Appendix is about the iterations to taken for implementing the conjugate gradient method and the convergence of the method to the actual solution of $Au = f$.

Theorem C.2.2. *Let $x_0 \in \mathbb{R}^N$. Define $w_1 = f - Ax_1$ Knowing x_n and w_{n-1} we define x_{n+1} and w_n by*

$$x_{n+1} = x_n + \alpha_n w_n$$

$$w_n = r_n + \beta_n w_{n-1}$$

where

$$r_n = f - Ax_n, \alpha_n = \frac{(r_n, w_n)}{(w_n, Aw_n)}, \beta_n = \frac{(r_n, r_n)}{(r_{n-1}, r_{n-1})}$$

Then w_n are mutually conjugate directions and x_{N+1} is the unique solution of $Ax = f$.

Proof. A proof of this theorem can be found in [57]. □

Remark C.2.1. *It can be shown that*

$$x_n - x_{N+1} \sim \left(\frac{1 - \sqrt{c}}{1 + \sqrt{c}}\right)^n$$

where $c = \frac{m}{M}, m = \inf_{x \neq 0} \frac{(Ax, x)}{\|x\|^2}, M = \sup_{x \neq 0} \frac{(Ax, x)}{\|x\|^2}$. The convergence rate for conjugate gradient method is faster than the steepest descent method, atleast for quadratic functionals. Also as condition number of $A \sim \frac{C}{h^2}$ when $V_h \subset H^1(\Omega)$, so conjugate gradient method is preferred over steepest descent method for finite elements.

Appendix D

Using Optical flow to determine fluid flow

We perform two separate experiments to show the difference in using optical flow method to track rigid bodies and fluid flows.

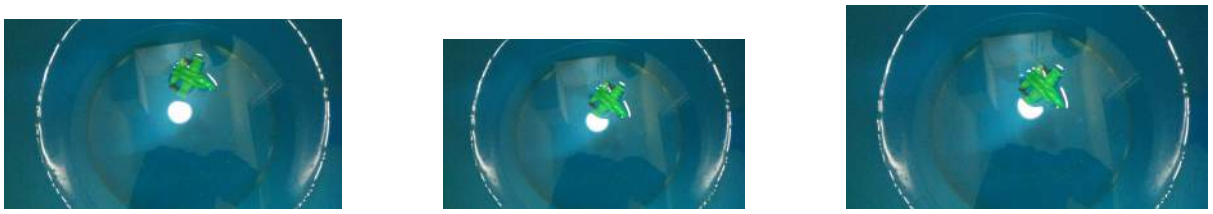

(a) (b) (c)

Figure D.1: Motion of the toy plane due to an imposed force on it representing rigid body motion. There is no movement of the underlying fluid.

Figure D.1 shows the motion of a toy plane in a bucket of water. The plane has been given a force to move by itself. There is no motion of water. This is evident by the reflection of the lamp which remains static in all the three pictures. This set of pictures represents the usual way of determining motion of the rigid body(plane) using optical flow method. There is no motion near the boundary of the domain and hence boundary conditions are trivial in this case.

(a) (b) (c)

Figure D.2: Motion of the toy plane due to movement of water.

Figure D.2 shows the motion of the toy plane due to motion of water. A vortex is imparted to the water in the bucket and the plane moves under its action. This is evident by the disturbance in the reflection of the lamp. This is the case we investigate in our thesis. We use optical flow techniques to capture motion due to fluid flows by tracing scalars(plane) propagated by the flow.

Bibliography

[1] M. Agranovsky, C. Berenstein, and P. Kuchment. Approximation by spherical waves in L^p-spaces. *J. Geom. Anal.*, 6(3):365–383, 1996.

[2] M. Agranovsky and E. T. Quinto. Injectivity sets for Radon transform over circles and complete systems of radial functions. *J. Functional Anal.*, 139:383–414, 1996.

[3] G. Ambartsoumian, J. Boman, V. P. Krishnan, and E. T. Quinto. Microlocal analysis of an ultrasound transform with circular source and receiver trajectories. American Mathematical Society, series =Contemporary Mathematics, volume =598, pages =45 – 58, 2013.

[4] G. Ambartsoumian, R. Felea, V. P. Krishnan, C. Nolan, and Eric Todd Quinto. A class of singular Fourier integral operators in synthetic aperture radar imaging. *J. Funct. Anal.*, 264(1):246–269, 2013.

[5] G. Ambartsoumian, R. Gouia-Zarrad, and M. A. Lewis. Inversion of the circular Radon transform on an annulus. *Inverse Problems*, 26(10):105015, 11, 2010.

[6] G. Ambartsoumian and V. P. Krishnan. Inversion of a class of circular and elliptical radon transforms. 2014. Submitted.

[7] G. Ambartsoumian and P. Kuchment. On the injectivity of the circular Radon transform. *Inverse Problems*, 21(2):473–485, 2005.

[8] G. Ambartsoumian and L. Kunyansky. Exterior/interior problem for the circular means transform with applications to intravascular imaging. *Inverse Probl. Imaging*, 8(2):339–359, 2014.

[9] L–E. Andersson. On the determination of a function from spherical averages. *SIAM J. Math. Anal.*, 19(1):214–232, 1988.

[10] Y. A. Antipov, R. Estrada, and B. Rubin. Method of analytic continuation for the inverse spherical mean transform in constant curvature spaces. *J. Anal. Math.*, 118(2):623–656, 2012.

[11] L. Arlotti, J. Banasiak and B. Lods. A new approach to transport equations associated to a regular field: trace results and well–posedness.*Mediterranean Journal of Mathematics.* 6:367–402, 2009

[12] E. Arnaud, E. Mémin, R. Sosa and G. Artana. A fluid motion estimator for schlieren image velocimetry. *In ECCV06*, I: 198–210, 2006.

[13] G. Aubert, R. Deriche and P. Kornprobst. Computing Optical Flow via Variational Techniques, *SIAM Journal of Math. Anal*, 60(1):156-182 , 1999.

[14] G. Aubert and P. Kornprobst. A mathematical study of the relaxed optical flow problem in the space ,*SIAM Journal of Math. Anal*, 30(6):1282–1308, 1999.

[15] H. H. Bauschke and P. L. Combettes. Convex analysis and monotone operator theory in Hilbert spaces. *CMS Books in Mathematics, Springer* xvi+468 pp. ISBN: 978-1-4419-9466-0, 2011.

[16] A. Borzi, K. Ito and K. Kunisch. An optimal control approach to optical ow computation. *Int. J. Numer. Meth. Fluids* 40:231–240, 2002.

[17] M. J. Black. Combining intensity and motion for incremental segmentation and tracking over long image sequences. In G. Sandini, editor, *Proc. of Second European Conference on Computer Vision, ECCV-92*, volume 588 of LNCS-Series, pages 485–493. Springer-Verlag, May 1992.

[18] M. J. Black. Robust Incremental Optical Flow YALEU/CSD/RR 923

[19] M. J. Black and P. Anandan. Constraints for the early detec- tion of discontinuity from motion. In *Proc. National Conf. on Artificial Intelligence, AAAI-90*, pages 1060–1066, Boston, MA, 1990.

[20] M. J. Black and P. Anandan. A model for the detection of motion over time. In *Proc. Int. Conf. on Computer Vision, ICCV-90*, pages 33–37, Osaka, Japan, December 1990.

[21] V. L. Blanc. L^1-stability of periodic stationary solutions of scalar convection-diffusion equations. *Journal of Differential Equations, Elsevier.* 247:1746–1761, 2009.

[22] P. Bouthemy and J. S. Rivero. A hierarchical likelihood approach for region segmentation according to motion-based criteria. In *Proc. First Int. Conf. on Computer Vision, ICCV-87* , pages 463–467, London, England, June 1987.

[23] J.–F. Cayula and P. Cornillon. Cloud detection from a sequence of SST images. *Remote Sens. Env.*, 55:80–88, 1996.

[24] P. Chandrashkehar, S. Roy and A. S. Vasudeva Murthy.A variational approach to estimate incompressible fluid flows. *Proceedings of Mathematical Sciences, Springer*, (under review), 2015.

[25] B. Cockburn and C.–W. Shu. The Runge–Kutta discontinuous Galerkin method for conservation laws V: multidimensional systems. *Journal of Computational Physics*, 141(2):199-224, 1998.

[26] B. Cockburn and C. –W. Shu. Runge–Kutta discontinuous Galerkin methods for convection-dominated problems. *Journal of scientific computing*, 16(3):173-261, 2001.

[27] B. Cockburn, G. E. Karniadakis and C.-W. Shu. Discontinuous Galerkin methods. Theory, computation and applications. *Lecture Notes in Computational Science and Engineering, Springer-Verlag, Berlin*, 2000.

[28] A. M. Cormack. Representation of a function by its line integrals, with some radiological applications. *J. Appl. Phys*, 34(9):2722 – 2727, 1963.

[29] T. Corpetti, E. Mémin, and P. Pérez. Dense estimation of fluid flows. *IEEE Trans. Pattern Anal. Mach. Intell.*, 24(3):365–380, 2002.

[30] A. Denisjuk. Integral geometry on the family of semi-spheres. *Fract. Calc. Appl. Anal.*, 2(1):31–46, 1999.

[31] J. A. Fawcett. Inversion of n-dimensional spherical averages. *SIAM J. Appl. Math.*, 45(2):336–341, 1985.

[32] D. Finch, M. Haltmeier, and Rakesh. Inversion of spherical means and the wave equation in even dimensions. *SIAM J. Appl. Math.*, 68(2):392–412, 2007.

[33] D. Finch, S. K. Patch, and Rakesh. Determining a function from its mean values over a family of spheres. *SIAM J. Math. Anal.*, 35(5):1213–1240 (electronic), 2004.

[34] D. Finch and Rakesh. The spherical mean value operator with centers on a sphere. *Inverse Problems*, 23(6):S37–S49, 2007.

[35] S. V. Fogel. The estimation of velocity vector-fields from time varying image sequences. *CVGIP: Image Understanding*, 53:253–287, 1991.

[36] J. Frikel and E. T. Quinto. Artifacts in incomplete data tomography with applications to photoacoustic tomography and sonar. 2014. Preprint.

[37] E. Gamble and T. Poggio. Integration of intensity edges with stereo and motion. Technical Report Artificial Intelligence Lab Memo No. 970, MIT, 1987.

[38] V. Girault and P.–A. Raviart. Finite Element Methods for Navier-Stokes Equations. Theory and Algorithms. *Springer Series in Computational Mathematics. Springer-Verlag*, Berlin, Germany, 1986.

[39] A. Greenleaf and G. Uhlmann. Non-local inversion formulas for the X-ray transform. *Duke Math. J.*, 58:205–240, 1989.

[40] V. Guillemin. Some remarks on integral geometry. Technical report, MIT, 1975.

[41] V. Guillemin and S. Sternberg. *Geometric asymptotics*. American Mathematical Society, Providence, R.I., 1977. Mathematical Surveys, No. 14.

[42] P. C. Hansen. The truncated SVD as a method for regularization. *BIT*, 27(4):534–553, 1987.

[43] H. W. Haussecker and D. J. Fleet. Computing Optical Flow with Physical Models of Brightness Variation, *IEEE Transactions on Pattern Analysis and Machine Intelligence* , 23(6):661–673, 2001.

[44] F. Heitz and P. Bouthemy. Multimodal motion estimation and segmentation using Markov random fields. In *Proc. IEEE Int. Conf. on Pattern Recognition* , pages 378–383, June 1990.

[45] D. Heitz, E. Mémin and C. Schnörr. Variational fluid flow measurement from image sequences: synopsis and perspectives. *Exp. Fluids*, 48:369–393, 2010.

[46] M. Hinze, R. Pinnau, M. Ulbrich, S. Ulbrich. Optimization with PDE Constraints. *Springer*, xii+270 pp, ISBN 978-1-4020-8839-1, 2009.

[47] R. A. Horn and C. R. Johnson. *Matrix analysis*. Cambridge University Press, Cambridge, second edition, 2013.

[48] B. K. P. Horn. *Robot Vision*. The MIT Press, Cambridge, Massachusetts, 1986.

[49] B. K. P. Horn and B. G. Schunck. Determining optical flow. *Artificial Intelligence*, 17(1-3):185–203, 1981.

[50] S. Kesavan. Topics in Functional Analysis and Applications. *New Age Intenational Publishers*, 2008.

[51] P. Kuchment and L. Kunyansky. Mathematics of thermoacoustic tomography. *European J. Appl. Math.*, 19(2):191–224, 2008.

[52] H. P. Langtengen. Computational Partial Differential Equations–Numerical methods and Diffpack programming. *Texts in Computational Science and Engineering, Springer* LII, 860 pp. ISBN: 978-3-642-55769-9, 2003.

[53] M. M. Lavrentiev, V. G. Romanov, and V. G. Vasiliev. *Multidimensional inverse problems for differential equations.* Lecture Notes in Mathematics, Vol. 167. Springer-Verlag, Berlin-New York, 1970.

[54] J. A. Leese, C. S. Novak and V. R. Taylor. The determination of cloud pattern motions from geosynchronous satellite image data. *Pattern Recog.*, 2:279–292, 1970.

[55] T. Liu and L. Shen. Fluid Flow and optical flow. *J. Fluid Mech*, 614:253–291, 2008.

[56] A. Logg, K.–A. Mardal, G. N. Wells. Automated Solution of Differential Equations by the Finite Element Method. *Springer*, 2012.

[57] D.G. Luenberger. Optimization by vector space methods. *John Wiley*, 1969.

[58] S. Mensah and E. Franceschini. Near-field ultrasound tomography. *J. Acoust. Soc. Am*, 121.

[59] S. Mensah, E. Franceschini, and J–P. Lefevre. Mammographie ultrasonore en champ proche. *Trait. Signal*, 23(3-4):259–276, 2006.

[60] S. Mensah, E. Franceschini, and M–C. Pauzin. Ultrasound mammography. *Nuclear Instruments and Methods in Physics Research*, 571(3):52–55, 2007.

[61] A. Mitiche and A–R. Mansouri. On the convergence of the Horn and Schunck Optical-Flow Estimation Method. *IEEE Transactions on Image Processing*, Vol. 13 No. 6 June 2004.

[62] S. Moon. On the determination of a function from an elliptical Radon transform. *J. Math. Anal. Appl.*, 416(2):724–734, 2014.

[63] N. Mukawa. Estimation of shape, reflection coefficients and illuminant direction from image sequences. *In ICCV90*, 507–512, 1990.

[64] D. W. Murray and B. F. Buxton. Scene segmentation from visual motion using global optimization. *IEEE Trans. on Pattern Analysis and Machine Intelligence*, PAMI-9(2):220–228, March 1987.

[65] H.–H. Nagel. Displacement vectors derived from second-order intensity variations in image sequences. *CGIP*, 21:85-117, 1983.

[66] H.–H. Nagel. On the estimation of optical flow: Relations between different approaches and some new results. *AI*, 33:299-324, 1987.

[67] H.–H. Nagel. On a constraint equation for the estimation of displacement rates in image sequences. *IEEE Trans. PAMI*, 11:13-30, 1989.

[68] H.–H. Nagel and W. Enkelmann An investigation of smoothness constraints for the estimation of displacement vector fields from image sequences. *IEEE Trans. PAMI*, 8:565-593, 1986.

[69] Y. Nakajima, H. Inomata, H. Nogawa, Y. Sato, S. Tamura, K. Okazaki and S. Torii. Physics-based flow estimation of fluids. *Pattern Recognition*, 36(5):1203 – 1212, 2003.

[70] L. V. Nguyen. A family of inversion formulas in thermoacoustic tomography. *Inverse Probl. Imaging*, 3(4):649–675, 2009.

[71] L. V. Nguyen. Spherical mean transform: a PDE approach. *Inverse Probl. Imaging*, 7(1):243–252, 2013.

[72] S. J. Norton. Reconstruction of a two-dimensional reflecting medium over a circular domain: exact solution. *J. Acoust. Soc. Amer.*, 67(4):1266–1273, 1980.

[73] S. J. Norton and M. Linzer. Reconstructing spatially incoherent random sources in the nearfield: exact inversion formulas for circular and spherical arrays. *J. Acoust. Soc. Amer.*, 76(6):1731–1736, 1984.

[74] N. Papadakis and E. Mémin. Variational assimilation of fluid motion from image sequence. *SIAM Journal on Imaging Sciences*, 1(4):343-363, 2008.

[75] J. A. Parikh, J. S. DaPonte, J. N. Vitale and G. Tselioudis. An evolutionary system for recognition and tracking of synoptic scale storm systems. *Pattern Recognition Letters*, 20:1389–1396, 1999.

[76] S. Peleg and H. Rom. Motion based segmentation. In *Proc. IEEE Int. Conf. on Pattern Recognition*, pages 109–113, June 1990.

[77] R. Plato. The regularizing properties of the composite trapezoidal method for weakly singular Volterra integral equations of the first kind. *Adv. Comput. Math.*, 36(2):331–351, 2012.

[78] J. L. Potter. Scene segmentation using motion information. *IEEE Trans. on Systems, Man and Cybernetics*, 5:390–394, 1980.

[79] W. H. Press, S. A. Teukolsky, W. T. Vetterling, and B. P. Flannery. *Numerical recipes in C*. Cambridge University Press, Cambridge, second edition, 1992. The art of scientific computing.

[80] A. Quarteroni and A. Valli. Numerical Approximation of Partial Differential Equations. *Springer Series in Computational Mathematics*, 1994.

[81] E. T. Quinto. Singularities of the X-ray transform and limited data tomography in $\mathbb{R}^2$ and $\mathbb{R}^3$. *SIAM J. Math. Anal.*, 24:1215–1225, 1993.

[82] A. W. Roberts and D. E. Varberg. Convex Functions, *Academic Press, New York and London*, 1973.

[83] V. G. Romanov. An inversion formula in a problem of integral geometry on ellipsoids. *Mat. Zametki*, 46(4):124–126, 1989.

[84] S. Roy. Optical Flows - Determination of 2D velocities of a moving fluid. *M.Phil Thesis, Tata Institute of Fundamental Research, CAM, Bangalore*,`https://www.dropbox.com/s/zpqi5btol7mehbq/mphil.pdf?dl=0`, 2011.

[85] S. Roy, P. Chandrashkehar and A. S. Vasudeva Murthy. A variational approach to Optical Flow estimation of unsteady incompressible flows. *Journal of Computational Mathematics, Global Science*, (under review), 2014.

[86] S. Roy, V. P. Krishnan, P. Chandrashkehar and A. S. Vasudeva Murthy. An efficient numerical algorithm for Radon transform inversion with applications in ultrasound imaging and related fields. *Springer Journal of Mathematical Imaging and Vision*, (to appear), 2014.

[87] B. Rubin. Inversion formulae for the spherical mean in odd dimensions and the Euler-Poisson-Darboux equation. *Inverse Problems*, 24(2):025021, 10, 2008.

[88] P. Ruhnau and C. Schnörr. Optical Stokes flow: An imaging based control approach. *Exp. Fluids*, 42:61–78, 2007.

[89] J. Schmetz, P. Pili, S. Tjemkes, D. Just, J. Kerkmann, S. Rota and A. Ratier. An Introduction to Meteostat Second Generation (MSG).*American Meteorological Society*, 2002.

[90] C. Schnörr. Determining Optical Flow for Irregular Domains by Minimizing Quadratic Functionals of a Certain Class. *International Journal of Computer Vision*, 6:1, 25-38 (1991).

[91] B. G. Schunck. Image flow segmentation and estimation by constraint line clustering. *IEEE Transactions on Pattern Analysis and Machine Intelligence*, 11(10):1010–1027, October 1989.

[92] E. Simoncelli, E. Adelson, and D. Heeger. Probability distributions of optical flow. In *Proc. CVPR*, 310–315, 1991.

[93] S. Soatto and A. J. Yezzi. Deformotion - Deforming Motion, Shape Average and the Joint Registration and Segmentation of Images. *International Journal of Computer Vision.* , 53:153–167, 2003.

[94] A. Spoerri and S. Ullman. The early detection of motion boundaries. In *Proc. 1st ICCV*, pages 209–218, London, UK, June 1987.

[95] J. E. Stout, D. W. Martin, and D. N. Sikdar. Estimating GATE rainfall with geosynchronous satellite images. *Mon. Wea. Rev.*, 107:585–598, 1979.

[96] M. J. Tarr and M. J. Black. A computational and evolution- ary perspective on the role of representation in computer vision. Technical Report YALEU/DCS/RR-899, Yale University, October 1991.

[97] W. B. Thompson. Combining motion and contrast for segmentation. *IEEE Transactions on Pattern Analysis and Machine Intelligence*, AMI-2:543–549, 1980.

[98] W. B. Thompson, K. M. Mutch, and V. Berzins. Edge detection in optical flow fields. In *Proc. of the Second National Conference on Artificial Intelligence*, pages 26–29, August 1982.

[99] W. B. Thompson, K. M. Mutch, and V. A. Berzins. Dynamic occlusion analysis in optical flow fields. *IEEE Transactions on Pattern Analysis and Ma- chine Intelligence*, PAMI-7(4):374–383, July 1985.

[100] F. Tröltzsch. Optimal Control of Partial Differential Equations: Theory, Methods and Applications. *Graduate Studies in Mathematics, American Mathematical Society*, Vol-112, 2010.

[101] Q. X. Wu. A correlation-relaxation labeling framework for computing optical flow- Template matching from a new perspective. *IEEE Trans. Pattern Analysis and Machine Intelligence*, 17:843–853, 1995.

[102] J. Yuan, P. Ruhnau, E. Mémin, and C. Schnörr. Discrete orthogonal decomposition and variational fluid flow estimation. In *Scale-Space* 2005, volume 3459 of *Lect. Not. Comp. Sci.*, pages 267–278. Springer, 2005.

[103] L. Zhou, C. Kambhamettu, D. Goldgof, K. Palaniappan, and A. Hasler. Tracking non-rigid motion and structure from 2D satellite cloud images without correspondences. *IEEE Trans.PAMI*, 23(11):1330–1336.

[104] F. G. Tricomi. *Integral equations*. Dover Publications, Inc., New York, 1985. Reprint of the 1957 original.

[105] V. V. Volchkov. *Integral geometry and convolution equations*. Kluwer Academic Publishers, Dordrecht, 2003.

[106] V. Volterra. *Theory of functionals and of integral and integro-differential equations*. With a preface by G. C. Evans, a biography of Vito Volterra and a bibliography of his published works by E. Whittaker. Dover Publications, Inc., New York, 1959.

[107] R. Weiss. Product integration for the generalized Abel equation. *Math. Comp.*, 26:177–190, 1972.